THE UNIVERSITY *of* EDINBURGH

Development of High-Pressure Single-Crystal Neutron Diffraction on KOALA

Jack Binns

Supervisor: Prof. S Parsons

January 2016

Declaration

This thesis has been written entirely by me and has not been submitted in any previous application for a degree. Except where stated, all the work detailed in this thesis has been carried out by me.

Jack Binns

Acknowledgments

I must begin by thanking Prof. Simon Parsons, firstly for the opportunity to undertake this project and secondly for all the expertise, support, teaching, and quite interesting etymological discussions. The time I have spent in your group as been an absolute pleasure.

Thanks also to Prof. Garry McIntyre for all your assistance and guidance during my time in Sydney. Your enthusiasm and curiosity were a great motivator and I am very thankful to have been one of your students. Thank you for the introduction to superior Melbournian pies and an excellent selection of jokes, I wish I could remember more than one at a time.

Many thanks also to Dr. Stephen Moggach for all your kind words and for imparting so much crystallographic know-how, I wish you and your girls all the best. Thanks also to Prof. Konstantin Kamenev for all your help and experimental expertise and advice.

A big thank you to all the members of the Parsons and Moggach groups over my time in Edinburgh and a special thanks to Andy, Jorge, and Scott, you have been great colleagues and better friends. To Jon, Sara, and Matt thanks for being great friends and flatmates during my time Down Under.

I would certainly not be have gotten this far without my family and I cannot thank you enough for everything you have done for me. To my Grandpa, despite the lack of chemical reactions, I hope you enjoy reading this thesis.

Finally, to Rosie I am very lucky to have met you! Your affection, friendship, support and encouragement very far from home has meant the world.

I dedicate this work to the memory of my grandmother Grace.

Abstract

This thesis project has focused on the development of high-pressure single-crystal diffraction experiments on the neutron Laue diffractometer KOALA at the OPAL reactor at ANSTO, Australia. Over the course of this project several candidate systems have been studied under conditions of high-pressure using X-ray diffraction with a view to their use in developmental experiments on KOALA. The results of two high-pressure KOALA experiments are presented as well as the notable results from X-ray diffraction on the candidate systems.

The first experiment on hexamethylenetetramine provided valuable insights into how reduced crystallite size and reciprocal-space access affects data collected on KOALA. In addition, data treatment techniques were developed to deal with the unique and challenging high-pressure Laue data, including corrections for attenuation due to the cell body. The ability to collect data through the body of cell prompted a further experiment on the complex, low-symmetry structure of the amino acid L-arginine dihydrate. Despite the smaller crystal size and dominant parasitic scattering from the diamond-anvil cell, the data collected allow a full anisotropic refinement of hexamethylenetetramine with bond lengths and angles that agree with literature data within experimental error. This technique is highly suited to low-symmetry crystals, as shown by the successful refinement of data from a L-arginine dihydrate crystal. In such cases the transmission of diffracted beams results in higher completeness values than are possible with X-rays.

The hydrogen-bonded ferroelectric rubidium hydrogensulfate was the subject of ambient-pressure experiments on KOALA investigating the nature of the ferroelectric transition. Further high-pressure X-ray diffraction studies were carried out to resolve the structures of phases at high-pressure and to investigate the ferroelectric transition under pressure.

The potassium cobalt citrate metal-organic framework UTSA-16 has shown a wide variety of pressure-mediated framework-solvent interactions including negative linear compressibility, the ordering of potassium ions, and coordination changes which were investigated by high-pressure single-crystal and powder X-ray diffraction. These behaviors are rationalised by examination of the structural changes occurring in the framework

under pressure.

Two members of the widely studied alkylammonium tetrachlorometallate family, tetramethylammonium tetrachloroferrate(III) and tetramethylammonium tetrachlorogallate(III), display numerous phase transitions with temperature. The structures of these phases have been determined for the first time, and the contrast between the two materials explored with first-principles calculations.

Contents

Chapter 1

Introduction

1.1 Introduction

The correlation between structure and property is the central tenet of material science and informs both the understanding of a material's properties and also efforts to design improved functional materials. Historically, temperature and chemical composition have been the primary variables used in the investigation of structure-property relationships, however since the beginning of the last century pressure has been increasingly utilised as a probe capable of inducing unique changes to a material of interest.

1.1.1 High-pressure science

Since the earliest studies of Bridgman at the beginning of 20^{th} century, high-pressure methods have found application in almost all areas of condensed-matter research for which Bridgman received the 1946 Nobel prize in physics (Bridgman, 1946).

Conditions of pressure vary enormously in nature, from the vacuum of space to the core of a neutron star, pressure varies almost forty orders of magnitude; even for more mundane stars such as the Sun, the pressure at the core reaches an estimated 10^{16} Pa. While these extreme conditions are still beyond experimental feasibility, conditions approaching those in the centre of the Earth (3.6×10^{11} Pa) and other celestial bodies are possible, and form an integral part of geophysics and astrogeophysics (Anderson and Hart, 1976). Geophysical and mineralogical research has driven much of the development of high-pressure (and high-temperature) experimental techniques in an attempt to replicate the conditions inside the Earth (Hemley *et al.*, 1987; Miletich *et al.*, 2000; Navrotsky, 2015).

High-pressure techniques have been widely used in condensed-matter-physics studies of the elements and simple compounds up to very high (10^{11} Pa) pressures, with the holy grail being the metallic, possibly superconducting, phase of hydrogen (Ashcroft, 1968; Holzapfel, 1996; Kenichi *et al.*, 2003; Lundegaard *et al.*, 2006; Drummond *et al.*, 2015). This continues to be an active field, recent measurements by Drozdov *et al.* of hydrogen sulfide under high-pressure (200 GPa) suggests that this material is capable of superconductivity at an unprecedented temperature of 203 K (Drozdov *et al.*, 2014, 2015), sparking interest in a wide range of hydride materials as high-temperature su-

perconductors (Errea *et al.*, 2015). Outside the field of superconductivity, pressure is widely used as a tool for understanding structure-property relationships within materials *e.g.* (Guennou *et al.*, 2011) as well as for the synthesis of novel functional materials (Arevalo-Lopez *et al.*, 2014).

The effect of pressure on biological systems is by contrast a relatively under-developed field, despite the observation that the average pressure at the bottom of the oceans is approximately 4×10^7 Pa (Mozhaev *et al.*, 1996), although piezophilic bacteria have been detected in the Mariana Trench at pressures as high as 1.3×10^8 Pa (Allen and Bartlett, 2004). Crystallographic studies of proteins from peizophiles are shedding light on the adaptations required for life under such extreme conditions (Nagae *et al.*, 2012).

Beyond marine biology, high-pressure techniques are finding increased application structural biology, giving insights into the protein-folding process by causing conformational changes that are inaccessible by heating and cooling (Fourme *et al.*, 2001, 2012; Girard *et al.*, 2005). While the conformational potential energy surface of proteins is in general well-characterised for changes of temperature (Leopold *et al.*, 1992), the structure of the pressure-dependent surface is largely unknown and difficult to generalise (Silva *et al.*, 2001; Cioni and Gabellieri, 2011).

Structural studies of molecular materials at high pressures are used to investigate the abundant low-molecular-weight compounds thought to compose the structures of icy satellites such as Saturn's Titan and the Galilean moons (Loveday *et al.*, 2001; Maynard-Casely *et al.*, 2012). The mechanical and thermodynamic information from such studies is vital to understanding phenomena such as cryovulcanism, as well as raising the possibility of liquid oceans on a number of icy moons in the solar system (Sotin *et al.*, 1998; Loveday and Nelmes, 2003).

The prevalence of weak, and therefore highly compressible, intermolecular forces in molecular crystals allows the direct probing of structure-property relationships in crystalline materials, without the need to adjust the crystallisation conditions or other chemical variables (Hemley and Dera, 2000). To date, a wide range of crystalline materials have been investigated, ranging from simple organic compounds (Allan and Clark, 1999) to much larger molecules of amino acids (Moggach *et al.*, 2008), vitamins (Fabbiani *et al.*, 2010), molecular magnets (Prescimone *et al.*, 2008; Craig *et al.*, 2015), and

metal-organic frameworks (Graham *et al.*, 2012).

Hydrogen bonds are perhaps the most widely studied intermolecular interaction and are often invoked as 'structure-directing' in the discussion and rationalisation of polymorphism in molecular solids (Gavezzotti, 2013; Moggach *et al.*, 2015). It is no surprise then to find that much of the high-pressure work on molecular solids has examined hydrogen bonding (Boldyreva, 2004; Moggach *et al.*, 2008; Funnell *et al.*, 2013).

Under ideal conditions hydrogen atoms can typically be located by X-ray diffraction, however the systematic errors and low completeness introduced by high-pressure cells means that hydrogen atoms are often absent in electron-density maps. Hydrogen-atom positions may be inferred from the location of other atoms or calculated from first principles; however there are cases where this is not possible. The most troublesome are complex hydrate structures where several hydrogen-bonding schemes may be in accordance with a satisfied hydrogen-bond network (Capelli *et al.*, 2013), however the incorrect hydrogen atom location can result in wildly inaccurate estimations of the thermodynamic stability of a particular polymorph, especially troubling for *ab initio* prediction of organic hydrate structures (Hulme *et al.*, 2007; Bardwell *et al.*, 2011).

While the scattering amplitudes of X-rays f increase linearly with atomic number Z, most neutron scattering amplitudes b are within a factor of three of each other and vary in a pseudorandom manner with atomic number Z (Sears, 1992). The contrast between scattering factors for X-rays and neutrons is illustrated in Figure 1.1.1. Significant differences exist between neighbouring elements and even isotopes of the same element.

This makes neutron diffraction an ideal technique for the location of light atoms, especially hydrogen and deuterium, which are both strong neutron scatterers. Neutron diffraction has been the primary technique for hydrogen-atom location in a range of materials; from an early powder diffraction study of uranium hydride (Rundle, 1951) to the examination of hydrogen/deuterium exchange in proteins *via* high-resolution single-crystal neutron diffraction (Chen *et al.*, 2012).

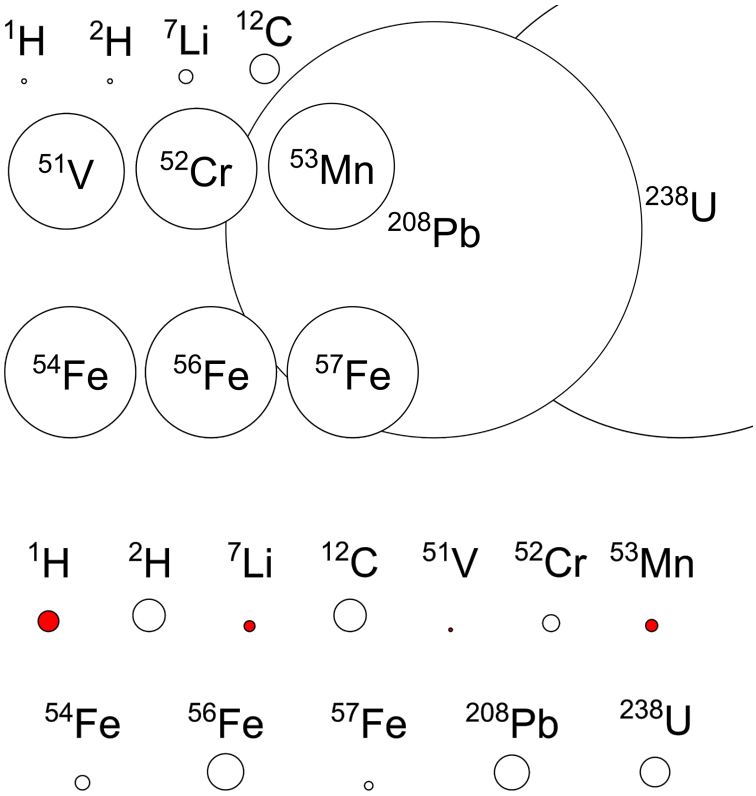

Figure 1.1.1: Contrasting scattering lengths for X-rays and neutrons. Each set of scattering lengths is scaled to the ^{1}H value for that radiation.

1.2 Neutron diffraction

1.2.1 Properties of the neutron

Neutrons have found wide application in a great variety of condensed-matter studies since the invention of nuclear reactors and the subsequent development of dedicated spallation sources. The utility of neutrons results both from their fundamental properties as well as by contrast with X-ray scattering.

The neutron was discovered by James Chadwick in 1932 while investigating the bombardment of beryllium foil by alpha radiation, his results were explained by the production of a particle with zero charge and a mass equivalent to a proton (Chadwick, 1932).

The mass of the neutron is in fact slightly larger than that of the proton (1.001 m_p) and for 'thermal' neutrons, with a conventional standard velocity of $v = 2.20{\times}10^3$ m s^{-1}($E = 25.3$ meV, $\lambda = 1.8$ Å, corresponding to a thermal energy k_BT for 294 K), the de Broglie wavelength is on the scale of interatomic distances within condensed matter leading to interference effects giving information on the geometry of the material.

The electrical neutrality of the neutron ($q_n = (-0.4{\pm}1.1){\times}10^{-21}$ e (Baumann *et al.*, 1988)) results in no Coulombic interaction with the electrons within a material. As a result, neutrons are a highly penetrating form of radiation and scattering is mediated directly by nucleus and becomes dependent upon the specific nuclide (Squires, 1978). While being electrically neutral, the neutron has a spin of $1/2$ with a magnetic moment of $\mu_n = -1.913\,\mu_N$ where $\mu_N = e\hbar/2m_p$ is the nuclear magneton, neutrons are therefore scattered by the unpaired electrons in magnetic atoms. This allows the structure and distributions of magnetic moments in a solid to be probed by elastic (Bragg) scattering (Lynn, 1994).

In addition to studying the distributions of nuclei and unpaired electrons, neutrons can also be used to study excitations within solids. The energies of thermal neutrons are on the same order of magnitude as many excitations within condensed matter. Consequentially the creation or annihilation of these excitations (*e.g.* phonons, magnons, *etc.*) by incident neutrons results in significant changes in the energies of scattered neutrons. Inelastic neutron scattering has become an invaluable tool in the study of dy-

namics, in particular the measurement of magnetic excitations and phonon dispersion relations which almost exclusively rely upon neutron scattering (Dolling and Brockhouse, 1962).

1.2.2 Scattering of neutrons by atoms

Neutron scattering by a nucleus is governed by the strong nuclear force which operates on length scales of 10^{-14} to 10^{-15} m. Thermal neutrons possess a wavelength in the region of 10^{-10} m and in the incident beam may be represented by a plane wave along the z-axis with wavevector $\mathbf{k}$, magnitude $|\mathbf{k}| = k = {}^{2\pi}/_{\lambda}$, with wavefunction $\psi_{in} = e^{ikz}$. The scattered wave ψ_{sc} will be spherically symmetrical as a result of the small size of the scattering body relative to the scattering radiation. The magnitude of the scattered wave will decrease with distance from the nucleus r in proportion to the constant b known as the *scattering length*. The negative sign in Equation 1.2.2 is conventional and corresponds to a positive repulsive (psuedo-)potential between neutron and the nucleus, which is the case for the majority of nuclides.

$$\psi_{in} = e^{ikz} \tag{1.2.1}$$

$$\psi_{sc} = -\frac{b}{r}e^{ikr} \tag{1.2.2}$$

The density of scattered neutrons at some distance r is therefore $|\psi_{sc}|^2 = {}^{b^2}/_{r^2}$. The total cross-section of a nucleus σ is defined as the number of particles scattered in all directions per second divided by the incident flux ($I_0 = |\psi_{in}|^2 v$, where v is the neutron velocity) (Bacon, 1975).

$$\sigma = 4\pi r^2 v \frac{|\psi_{sc}|^2}{|\psi_{in}|^2 v} \tag{1.2.3}$$

$$\sigma = 4\pi r^2 v \frac{(b/r)^2}{v} \tag{1.2.4}$$

$$\sigma = 4\pi b^2 \tag{1.2.5}$$

The cross-section is the effective area of the target nucleus with b corresponding to the effective range of the nuclear potential, called the *Fermi pseudopotential*, $V(\mathbf{r})$, which describes the potential experienced by a neutron at position $\mathbf{r}$.

$$V(\mathbf{r}) = \frac{2\pi\hbar}{m_n} b\delta^3(\mathbf{r}) \tag{1.2.6}$$

Where $\delta^3(\mathbf{r})$ is the three-dimensional Dirac δ-function which ensures the scattering potential is zero except very close to the nucleus to reflect the very short effective range of the strong nuclear force.

Under normal conditions, neutrons are considered to scatter from the surface of the nucleus as if the two objects are impenetrable spheres. There is however a finite probability of the neutron penetrating the nucleus to form a *compound nucleus*. This compound nucleus is short-lived and is analogous to an excited electronic state, although less well understood (Bacon, 1975). The probability of compound-nucleus formation is a function of the total energy of the neutron-nucleus system; if its value is close to that of a hypothetical compound nucleus, resonant scattering or absorption can occur and the properties and energies of states within the compound nuclei determine which relaxation pathways are possible and their relative probabilities.

The Breit-Wigner formula (Breit and Wigner, 1936) gives an expression for a compound cross-section, which sums the scattering and absorption cross-sections, for some given nuclear properties as a function of neutron energy in the region of such a transition (Figure 1.2.1) (Bacon, 1975).

For the most part, nuclear energy levels are spaced hundreds of electron volts apart and so the milli-electron volt energies of thermal neutrons make little difference to the total energy of the neutron-nucleus system and thus b values are typically invariant with neutron wavelength. The magnitude and sign of the scattering length is determined by the difference to the closest energy level and whether it is to the high- or low-energy side of that level. The apparently random distributions of b values across the periodic table can be interpreted by considering the values of cross-section in the region of a nuclear transition; large positive values are due to neutron-nucleus system energies just above a transition, likewise large negative values will be observed in the case of neutron-

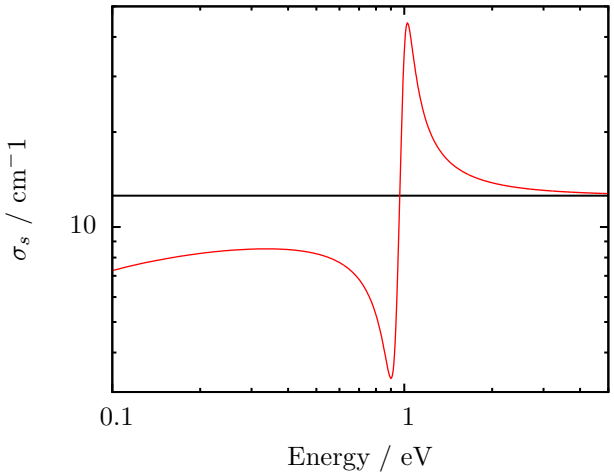

Figure 1.2.1: Calculated cross-sections versus neutron energy for a hypothetical nucleus with radius 10 fm and a single resonance at 1 eV. Solid line shows the high energy limit $4\pi R^2$. Plotted following (Bacon, 1975).

nucleus system energies just below (Bacon, 1975). The exact sign and magnitude of b is dependent upon the shape, depth, and range of the actual nuclear potential, which is often complex and poorly understood. Negative scattering lengths correspond to a phase change of π, rather than a change in the nature of the nuclear potential. For strongly absorbing nuclei, the scattering length is highly dependent upon neutron energy and a phase change other than π occurs during the scattering process making b a complex number. At high neutron energies the cross-section is directly proportional to the atomic radius and σ approaches $4\pi R^2$.

The scattering length is also dependent upon the total spin of the neutron-nucleus system, if the nucleus has non-zero spin I, the total spin of the system is $I + 1/2$ or $I - 1/2$ with each spin state having a corresponding b.

For a collection of atoms in a material there will be a mixture of isotopes and their distribution (and if applicable, spin states) will be random. As a result the scattering from a particular atomic site is split into coherent and incoherent scattering. For elastic scattering it is the coherent scattering which gives rise to the diffraction signal, incoherent scattering is uniform in direction and contributes an isotropic background (Furrer *et al.*, 2009).

$$\sigma = \sigma_{coh} + \sigma_{inc} \tag{1.2.7}$$

$$\sigma_{coh} = 4\pi \langle b \rangle^2 \tag{1.2.8}$$

$$\sigma_{inc} = 4\pi \left(\langle b^2 \rangle - \langle b \rangle^2 \right) \tag{1.2.9}$$

The corresponding coherent and incoherent scattering lengths are therefore $b_{coh} = \langle b \rangle$ and $b_{inc} = \sqrt{\langle b^2 \rangle - \langle b \rangle^2}$. Hydrogen is an example of a typical strong incoherent scatterer due to the very different scattering lengths of each spin state. With nuclear spin $I = 1/2$, the spin of the neutron-plus-nucleus system can be in a triplet ($S_+ = I + 1/2$) or singlet state ($S_- = I - 1/2$) with respective scattering lengths $b_+ = 10.85$ fm and $b_- = -47.50$ fm, resulting in $\sigma_{coh} = 1.76$ barn and $\sigma_{inc} = 80.3$ barn (1 barn $= 1 \times 10^{-28}$ m^2) (Furrer *et al.*, 2009).

1.2.3 Scattering by crystals

The regular arrangement of atoms in a crystal acts as a three-dimensional diffraction grating for both X-rays and thermal neutrons. The scattering density of the crystal in real space $\rho_{cr}(\mathbf{r})$ and the resulting diffraction pattern in reciprocal space $F_{cr}(\mathbf{k})$ are related by Fourier transformation where $\mathbf{r}$ and $\mathbf{k}$ are position vectors in real and reciprocal space respectively. The scattering density of the crystal in real space can be considered the convolution of the Bravais lattice $L(\mathbf{r})$, represented as a three-dimensional Dirac comb, and the scattering density of the unit cell $\rho_{uc}(\mathbf{r})$. The Dirac comb is an array of delta functions spaced at lattice points $\mathbf{R} = u\mathbf{a} + v\mathbf{b} + w\mathbf{c}$.

$$L(\mathbf{r}) = \sum_{u,v,w=-\infty}^{\infty} \delta^3(\mathbf{r} - \mathbf{R}) \tag{1.2.10}$$

The scattering density of the unit cell is typically approximated as the sum of the individual scattering densities of each atom $\rho_j(\mathbf{r}_j)$ in the unit cell at fractional coordinates $\mathbf{r}_j = (x_j\mathbf{a} + y_j\mathbf{b} + z_j\mathbf{c})$.

$$\rho_{uc}(\mathbf{r}) = \sum_{j=1}^{N} \rho_j(\mathbf{r} - \mathbf{r}_j) \tag{1.2.11}$$

The convolution theorem states that the Fourier transform of a convolution is the

product of Fourier transforms.

$$\rho_{cr}(\mathbf{r}) = \rho_{uc}(\mathbf{r}) * L(\mathbf{r}) \tag{1.2.12}$$

$$T[\rho_{cr}(\mathbf{r})] = T[\rho_{uc}(\mathbf{r})] \times T[L(\mathbf{r})] \tag{1.2.13}$$

The Fourier transform of a Dirac comb in real space is a Dirac comb in reciprocal space with delta functions now spaced at reciprocal lattice points $\mathbf{G} = h\mathbf{a}^* + k\mathbf{b}^* + l\mathbf{c}^*$.

$$T[L(\mathbf{r})] = \sum_{h,k,l=-\infty}^{\infty} \delta^3(\mathbf{k} - \mathbf{G}) \tag{1.2.14}$$

The Fourier transform of the unit-cell scattering density is called the *structure factor* $\mathbf{F}(\mathbf{k})$. The structure factor determines how the arrangement of atoms in the unit cell affects the measured intensity of a reflection and is usually described in terms of a distribution of N atoms at fractional coordinates $\mathbf{r}_j$ (Eq. 1.2.16).

$$T[\rho_{uc}(\mathbf{r})] = \mathbf{F}(\mathbf{k}) = \int \sum_{j=1}^{N} \rho_j(\mathbf{r} - \mathbf{r}_j) e^{2\pi i \mathbf{k}.\mathbf{r}_j} d\mathbf{r} \tag{1.2.15}$$

$$\mathbf{F}(\mathbf{k}) = \sum_{j=1}^{N} b_j e^{2\pi i \mathbf{k}.\mathbf{r}_j} \tag{1.2.16}$$

$$T[\rho_{cr}(\mathbf{r})] = F_{cr}(\mathbf{k}) = \sum_{j=1}^{N} b_j e^{2\pi i \mathbf{k}.\mathbf{r}_j} \times \sum_{h,k,l=-\infty}^{\infty} \delta^3(\mathbf{k} - \mathbf{G}) \tag{1.2.17}$$

The above relation shows that the diffraction pattern of a periodic material will have non-zero intensity only at discrete points in reciprocal space where $\mathbf{k} = \mathbf{G}$. The diffraction pattern of the crystal can therefore be considered as the structure factor of the unit cell sampled at reciprocal lattice points $\mathbf{G}$ labelled by indices $\mathbf{h} = (h, k, l)$. The structure factor is therefore usually written in terms of reflection $\mathbf{h}$ and is a complex quantity with magnitude $|\mathbf{F}(\mathbf{h})|$ and phase $\phi_{\mathbf{h}} = 2\pi(\mathbf{h}.\mathbf{r}_j) = 2\pi(hx_j + ky_i + lz_j)$:

$$\mathbf{F}(\mathbf{h}) = \sum_{j=1}^{N} b_j e^{2\pi i \mathbf{h}.\mathbf{r}_j} \tag{1.2.18}$$

$$\mathbf{F}(\mathbf{h}) = |\mathbf{F}(\mathbf{h})|e^{i\phi_{\mathbf{h}}} \tag{1.2.19}$$

From the measured diffracted beam intensities $I(\mathbf{h}) \propto |\mathbf{F}(\mathbf{h})|^2$, the scattering density at each point in the unit cell $\mathbf{r}$ is reconstructed by reverse Fourier transformation over the sum of measured reflections $\mathbf{h}$ in the diffraction pattern.

$$\rho(\mathbf{r}) = \frac{1}{V}\sum_{\mathbf{h}} \mathbf{F}(\mathbf{h})e^{-2\pi i\mathbf{h}.\mathbf{r}} \tag{1.2.20}$$

In neutron scattering, $\rho(\mathbf{r})$ corresponds to the nuclear scattering density and b_j is the scattering length of atom j measured in fm. For X-rays, $\rho(r)$ becomes the electron density and b_j is substituted by f_j, the atomic form factor measured in electrons.

Both atomic form factors and scattering lengths are the Fourier transforms of the corresponding atomic scattering densities. Consequentially the neutron scattering length, being represented by a δ-function, transforms to a constant and there is no decay in scattering power with angle as there is for atomic form factors. However this is not the case for interactions between neutrons and the magnetic moments of unpaired electrons and radicals (Zheludev *et al.*, 1994). Since the neutron scatters from the outer unpaired electrons only, the neutron magnetic form factor falls off with $\sin\theta/\lambda$ more rapidly than the X-ray form factor (Bacon, 1975).

1.2.4 Neutron Laue diffraction

Friedrich, Knipping, and von Laue's 1912 experiment using a polychromatic X-ray beam incident on a single crystal of copper sulfate pentahydrate was the first demonstration of atomic diffraction and earned the Nobel Prize for von Laue in 1914 (Friedrich *et al.*, 1912; Eckert, 2012). The technique which now bears von Laue's name uses the same polychromatic incident beam although the source is more likely to be a synchrotron or nuclear reactor than an X-ray tube. While the Laue method was the forerunner of all other methods of crystal-structure determination, the intrinsic complexity of analysis *versus* monochromatic techniques, as well as the mistakenly held belief that the technique suffered prohibitively from harmonic overlap, resulted in the technique lagging behind techniques utilising monochromatic sources (Amorós, 2012). The method was

soon relegated to determining Friedel symmetry, crystal quality, and orientation for use in other experiments.

The availability of synchrotron X-ray sources renewed interest in the method as a means of fully exploiting the full bandwidth of radiation produced at these sources, in particular when applied to macromolecular crystals (Moffat *et al.*, 1984). A rigorous investigation of the harmonic-overlap problem by Cruickshank, Helliwell and Moffat showed that the proportion of single-order reflections is greater than 83 %, making Laue diffraction suitable for crystal-structure determination (Cruickshank *et al.*, 1987, 1991).

In the context of X-ray diffraction, the Laue method reduces collection times allowing studies of weakly scattering crystals, biological samples vulnerable to radiation damage (Rabinovich and Lourie, 1987), and even time-dependent studies of subunit motion within protein crystals (Bourgeois *et al.*, 2003).

Neutron beams on the other hand are universally weak and expensive, a powerful driving force to utilise as much of the flux as possible. The neutron Laue instruments VIVALDI and LADI at the Institut Laue-Langevin (ILL) in France as well as KOALA at the OPAL reactor in Australia have proven the utility of the technique to problems in contemporary single-crystal neutron diffraction (McIntyre *et al.*, 2006; Blakeley, 2009).

The increase in flux to the sample by using a white beam allows crystals as small as 0.1 mm^3 to be used for structure determination (Edwards, 2011). The most common application of the neutron Laue technique has been the location of hydrogen atom positions in both organic species and metal clusters (Lin *et al.*, 2013; Edwards *et al.*, 2014; Jones *et al.*, 2013).

For large sample crystals full data collections can be relatively short allowing structural changes during phase transitions to be investigated in a feasible experimental time (Dobe *et al.*, 2004). In addition, magnetic scattering can also be observed in Laue patterns, the overlapping of nuclear and magnetic peaks requires careful treatment however quantitative analysis is possible (Schobinger-Papamantellos *et al.*, 2004). Other forms of magnetic ordering can also be detected thanks to the large solid-angle detectors used on these instruments. The mineral tapiolite ($FeTa_2O_6$) shows rods of scattered intensity along the $\mathbf{c}^*$ direction below the Néel temperature due to two-dimensional

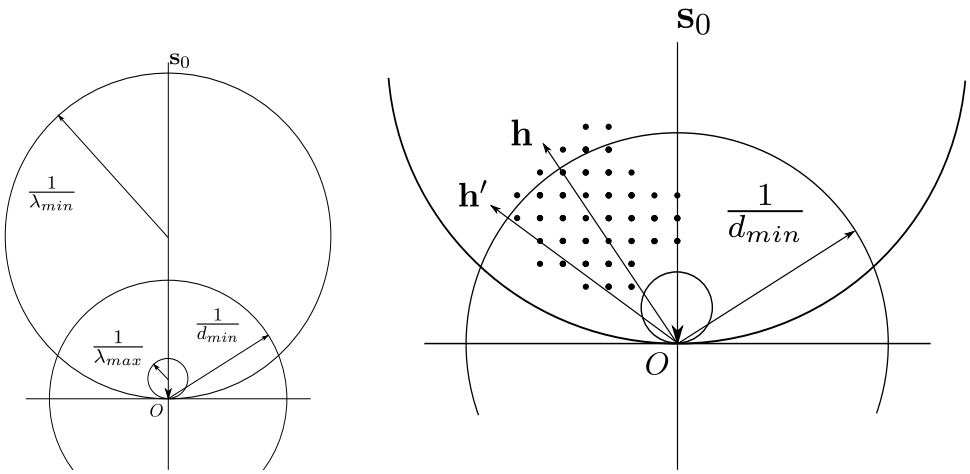

Figure 1.2.2: (a) Scaled Ewald construction for a Laue diffractometer having $\lambda_{max}/\lambda_{min} = 8$ as on KOALA. The accessible volume of reciprocal space is defined by the limits of $1/\lambda_{min}$, $1/\lambda_{max}$ and $1/d_{min}$ as rotated around the incident beam $\mathbf{s}_0$; (b) Illustration of the multiplicity problem. Ray $\mathbf{h}$ has a multiplicity of two due to the intrinsic resolution of the crystal which gives the maximum $1/d_{min} = d^*_{max}$ beyond which the reflection cannot be measured and so the outer points are beyond the resolution of the experiment. Ray $\mathbf{h}'$ on the other hand is single. Figures follow Cruickshank *et al.* (1987) and Wilkinson *et al.* (2002)

antiferromagnetic ordering between Fe sites (Chung *et al.*, 2004).

In the Laue technique, the sample single-crystal is illuminated by a polychromatic beam of X-rays or neutrons. This beam has a wavelength-dependent intensity distribution $\Lambda(\lambda)$, between the limiting wavelengths λ_{min} and λ_{max}. This results in a significant volume of reciprocal space being simultaneously explored, with each reciprocal lattice point self-selecting a wavelength distribution thus integrating intensity over wavelength rather than angle as in the monochromatic case (Giacovazzo *et al.*, 1993).

In the Ewald formalism the scattering geometry consists of a volume V_R as defined by spheres with limiting radii $1/\lambda_{min}$ and $1/\lambda_{max}$ sharing tangents at the reciprocal origin intersected by the sample resolution limit sphere with radius $1/d_{min} = d^*_{max}$ centered on the reciprocal origin (Figure 1.2.2). This volume is radially symmetrical around the incident beam and a typical Laue pattern will contain many more reflections than a monochromatic pattern (Cruickshank *et al.*, 1987).

1.2.4.1 The harmonic-overlap problem

The fundamental analytic difficulty inherent in the Laue method is the so-called *multiple-order* or *harmonic-overlap* problem (Cruickshank *et al.*, 1987, 1991; Amorós, 2012). The harmonic-overlap problem is a result of the fact that for any spacing d there exist further spacings of general form d/j where j is a positive integer. Bragg's law is then satisfied for a corresponding set of wavelengths λ/j. Therefore all Bragg reflections up to order j are exactly superimposed (an energy, rather than spatial overlap) provided λ and λ/j lie in the range $\Delta\lambda = 1/\lambda_{min} - 1/\lambda_{max}$ (Cruickshank *et al.*, 1987). These reciprocal lattice points lie along a line originating at the origin of reciprocal space, termed a ray by Cruickshank *et al.,* thus each Laue reflection arises from one ray and each reciprocal lattice point along that ray contributes to one, and only one, ray. A ray may be the summation of Bragg reflections, and the number contributing to a Laue reflection is termed the multiplicity m (Figure 1.2.2(b)).

A Laue diffraction pattern is therefore the distribution of rays in reciprocal space rather than the distribution of reciprocal lattice points as in the monochromatic case. Without energy discriminating detectors, it is impossible to quantify the contributions of each individual structure factor to a multiple-order ray and so the structure factor information is, in effect, lost. Without a detailed analysis it was assumed that a prohibitive number of Laue reflections were overlapped and the technique was unsuitable for structure determination.

As mentioned above, a Laue pattern is the distribution of rays, that is lines from the origin of reciprocal space to some reciprocal lattice point $\mathbf{h} = (h, k, l)$, and $2\mathbf{h}$, $3\mathbf{h}$...$n\mathbf{h}$. If greatest common denominator of h, k, and l is 1 then $\mathbf{h}$ is the inner point of the ray, *i.e.* the reciprocal lattice point closest to the origin along that ray. Reciprocal lattice point $n\mathbf{h} = (nh, nk, nl)$ is the n^{th}-order harmonic of $\mathbf{h}$.

Thus we can deduce the proportion of inner rays (*i.e.* single reflections) in any limiting range of h, k, and l by reducing the problem to one of number theory. The probability that an integer, h is divisible by an integer n is $1/n$, consequentially the probability that n is a common divisor of three integers h, k, and l is $1/n^3$ and conversely the probability that n is *not* a common divisor of h, k, l is $1 - (1/n^3)$. As a result, the

probability P that $\mathbf{h}$ is an inner point is given by the expression:

$$P = \prod_{j}^{n} 1 - \frac{1}{j^3} = \frac{1}{\zeta(3)} = 0.83191\ldots \tag{1.2.21}$$

Where the product is over the sequence of primes from $j = 2, 3, 5 \ldots n$. This product converges quickly to an approximate limit of 0.843 with only the first two terms. If n is taken to be on the order of typical h, k, l limits for a small molecules diffraction experiment, *e.g.* 11, this value converges to 0.833.

This probability can also be expressed as the inverse of the third-order Riemann zeta function $\zeta(3)$, and in general for n integers the probability P is given by the inverse n^{th}-order Riemann zeta function (Cruickshank *et al.*, 1987). This makes the Laue technique especially applicable for incommensurate structure determination as $P \to 1$ as $n \to \infty$ (McIntyre *et al.*, 2006). P is independent of crystal symmetry, orientation or unit-cell dimensions and depends only upon the ratio of λ_{max} to λ_{min}, as given implicitly in the choice of limiting prime in the product expression of P.

Further conclusions from the work of Cruickshank *et al.* are:

- P shows a marked dependency on d^* and $\Delta\lambda$, and typically increases proportionally with both.
- Restricting the angular acceptance of the detectors has a severe detrimental effect on P.
- The high-angle reflections are typically at high resolution and are predominantly single.
- A further form of overlap is possible for densely-packed low-index zones, although this entirely due to spatial overlap and can be mitigated with changes in orientation or crystal-to-detector distance for plate detectors (Cruickshank *et al.*, 1991).

1.2.4.2 Laue diffraction experiments

During a typical Laue diffraction experiment the crystal is held stationary during the exposure, and once completed the sample is rotated around the vertical axis, conventionally $\mathbf{z}$, by some angle ϕ and another exposure collected. The crystal class and unit-cell

dimensions determine the number of steps and the magnitude of ϕ. For low-symmetry crystals the sample may be rotated on the mount (around $\mathbf{x}$ or $\mathbf{y}$) and further data collected to get as large a reciprocal-space coverage as possible. The set of, typically, four to ten frames thus constitutes the data set (McIntyre *et al.*, 2006).

Detection of the diffracted neutrons is carried out using a neutron-sensitive image plate lining the interior of the cylindrical detector drum. The detector material, Eu^{2+}-doped BaFBr, is the same as used for X-ray image plates with the addition of Gd_2O_3. The gadolinium acts a neutron convertor, producing electrons and γ-rays with high efficiency when bombarded with neutrons. When irradiated with X-rays or γ-rays, Eu^{2+} is ionised to Eu^{3+} and the liberated electrons are trapped in Br vacancy states close to the conduction band forming F-centres (Niimura *et al.*, 1994). The irradiated material is then illuminated by a red reading laser and the resulting fluorescence is detected by a blue-light sensitive photomultiplier (Wilkinson *et al.*, 2000).

A Laue pattern for a crystal of L-arginine dihydrate is shown in Figure 1.2.3(a) and the corresponding simulated Laue patterns (Figures 1.2.3(b) and (c)) illustrate the general features of a Laue diffraction pattern. Spots are coloured by maximum wavelength and multiplicity in (b) and (c) respectively. Laue spots are arranged in groups of conic sections which arise from reflections in the same zone *i.e.* having planes containing a common rational direction or zone axis (Amorós, 2012). Each spot lies at the intersection of several zones, however the most obvious, high-density sections stand out clearest and are due to zones of low index such as the [001] zone marking out a sinusoidal section across the detector from left to right.

Where these low-index zones intersect the spots are referred to as nodals. The shape of the conic sections is dependent upon the angle between the zone axis and the incident beam, ψ. When $\psi < \pi/4$, the zone is an ellipse; for $\psi = \pi/4$ a parabola and for $\psi > \pi/4$, a hyperbola. The rotational symmetry of a zone is shown by the symmetry of conic sections surrounding the node and their corresponding zone axes.

Friedel symmetry can be precisely determined using this technique by directing the incident beam along a symmetry axis, the Laue pattern will display the symmetry present along that axis (Amorós, 2012). This effect is exploited in the Laue alignment cameras OrientExpress at ILL and JOEY at ANSTO (Ouladdiaf *et al.*, 2006; Klose

et al., 2014).

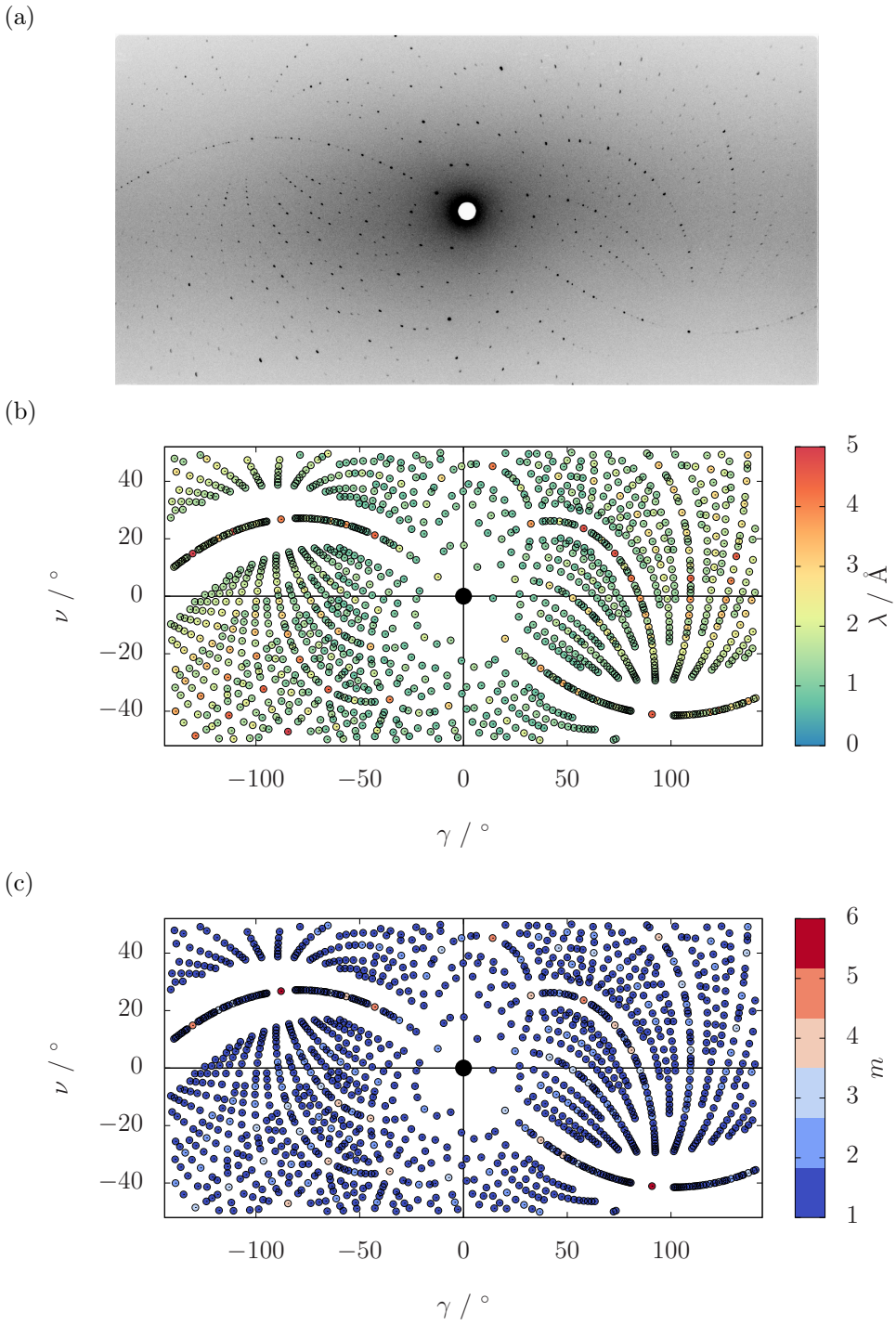

Figure 1.2.3: (a) Laue diffraction pattern for L-arginine dihydrate (Chapter 2). The sinusoidal shape of the high-density [001] zone is clear across the image from high to low γ; (b) Simulated Laue pattern for the same image, spots are coloured by the maximum wavelength for which the Bragg condition is satisfied; (c) Illustrates the multiplicity of each reflection based upon d and $\Delta\lambda$.

In the general Ewald construction, the end of scattering vector **h** forms a sphere of

radius $d^* = 2\sin\theta/\lambda$, the intersection of this sphere with the Ewald sphere of radius $1/\lambda$ creates the circle of observation, the reciprocal lattice point $\mathbf{h}$ is said to be in the diffracting condition if the tip of $\mathbf{h}$ lies at any point on this circle (Figure 1.2.4(a)). The only complication for Laue diffraction is that the circle of observation must be extended into a volume of observation by virtue of using a shell of thickness $\Delta\lambda$ rather than a single value. The Bragg condition is:

$$\mathbf{S}_1 - \mathbf{S}_0 = \frac{s_1 - s_0}{\lambda} = \mathbf{h} \tag{1.2.22}$$

Where $\mathbf{S}_0$ and $\mathbf{S}_1$ are vectors along the incident and diffracted beam respectively, of length $1/\lambda$. The KOALA diffractometer has a cylindrical detector and so the Bragg condition can be expressed in terms of cylindrical polar coordinates γ and ν as defined in Figure 1.2.4(b), the subscript makes clear this is in the laboratory frame:

$$\mathbf{h}_L = \left(\frac{1}{\lambda}\right)\begin{pmatrix} \sin\gamma\cos\gamma \\ \cos\gamma\cos\nu - 1 \\ \sin\nu \end{pmatrix} \tag{1.2.23}$$

Positions within the image, *i.e.* in the detector frame of a detector with radius R_D, in the horizontal (x_D) and vertical (y_D) are given by the relations below:

$$\tan\nu = \frac{y_D}{R_D} \tag{1.2.24}$$

$$\gamma = \frac{x_D}{R_D} \tag{1.2.25}$$

1.2.4.3 Indexing Laue diffraction patterns

The wavelength giving rise to a particular Laue spot is not known *a priori*, and so only the directions of the ray giving rise to a Laue spot can be determined. In almost all cases indexing a Laue pattern requires the unit-cell dimensions to be known beforehand. In general, indexing algorithms compare the relative angles between spots with a set of calculated rays generated from the known cell parameters to determine the orientation

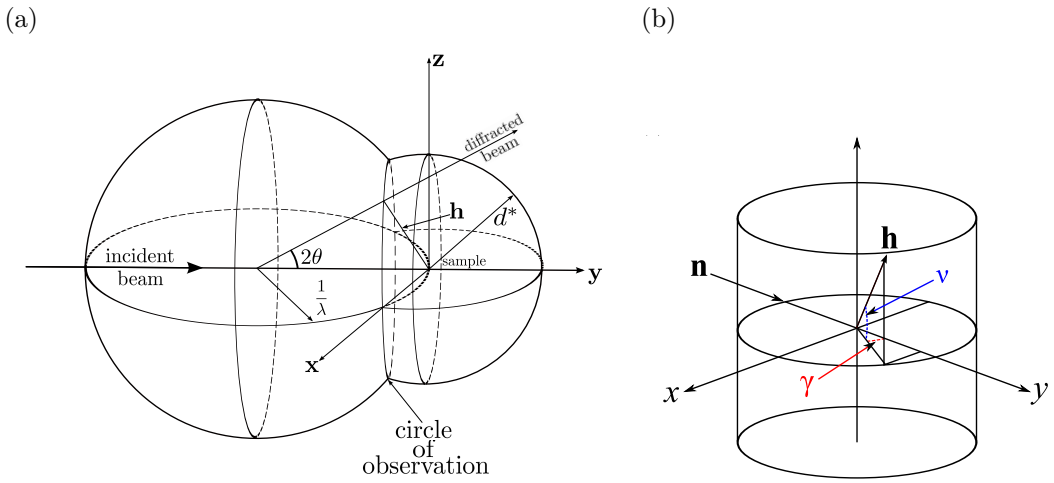

Figure 1.2.4: (a) Scattering vector **h** forms a sphere of radius $d^* = 2\sin\theta/\lambda$, the intersection of this sphere with an Ewald sphere of radius $1/\lambda$ creates the circle of observation. The reciprocal lattice point **h** is in the diffracting condition if the tip of **h** lies at any point on this circle. Adapted from (McIntyre and Stansfield, 1988); (b) Schematic of the Laue instruments. The incident beam, **n** travels along the instrument y axis. During an experiment the crystal is rotated about the vertical z axis by an angle ϕ between successive patterns. Each Laue spot **h** is characterised by a vertical angle ν and horizontal angle γ.

matrix **UB**. The orientation matrix is the product of two matrices, **B** which acts on the reciprocal axes to create an orthogonal set and **U** which brings this set into coincidence with the laboratory axis system. For a cylindrical Laue diffractometer such as KOALA, there is only one additional matrix, **Φ** which accounts for the rotation of the crystal about z by ϕ.

$$\mathbf{\Phi} = \begin{pmatrix} \cos\phi & \sin\phi & 0 \\ -\sin\phi & \cos\phi & 0 \\ 0 & 0 & 1 \end{pmatrix} \tag{1.2.26}$$

Therefore the Cartesian coordinates of a reflection, $\mathbf{h} = (h, k, l)$ in the laboratory frame $\mathbf{h}_L = (x, y, z)$ are given by:

$$\mathbf{h}_L = \mathbf{\Phi U B h} \tag{1.2.27}$$

The set of reciprocal vectors, as measured by spot coordinates, $\mathbf{z}_L$, are defined by analogy to $\mathbf{h}_L$ taking into account that λ is unknown:

$$\mathbf{z}_L = \mathbf{\Phi z} \tag{1.2.28}$$

$$\mathbf{z}_L = \lambda \mathbf{h}_L = \lambda \mathbf{UBh} = \begin{pmatrix} \cos\phi & \sin\phi & 0 \\ -\sin\phi & \cos\phi & 0 \\ 0 & 0 & 1 \end{pmatrix} \begin{pmatrix} \sin\gamma\cos\gamma \\ \cos\gamma\cos\nu - 1 \\ \sin\nu \end{pmatrix} \tag{1.2.29}$$

$$\cos 2\theta = \cos\nu \sin\gamma \tag{1.2.30}$$

A number of different algorithms exist for indexing using the above relations; one based on the comparison of angles is presented here. A list of n Laue spots is collected either by manual picking or an automatic peak-detection algorithm giving three quantities; the detector coordinates $(x_{D,i}, y_{D,i})$ and ϕ.

For each spot i, the Bragg angle θ_i and vectors $\mathbf{z}_{L,i}$ are calculated using the above relations. The angles between pairs of vectors are calculated: $\alpha_1 = \{\mathbf{z}_{L,1}, \mathbf{z}_{L,2}\}$, $\alpha_2 = \{\mathbf{z}_{L,1}, \mathbf{z}_{L,3}\}$, $\alpha_3 = \{\mathbf{z}_{L,2}, \mathbf{z}_{L,3}\}$. A series of $\mathbf{h}$'s are generated from the supplied unit-cell dimensions up to some maximum values of h, k, and l and the angles between them calculated. If a matching angle is found amongst the three experimental angles then the pattern is now indexed, the wavelength and hence the vectors $\mathbf{z}_i$ determined. $\mathbf{U}$ is determined following the method for finding an orthogonal matrix from Busing & Levy (Busing and Levy, 1967; Rodriguez-Carvajal *et al.*, 2014).

In practice, further comparisons are made and an array of possible solutions (typically containing symmetry equivalents) is presented. The index is then refined based on least-squares fitting of calculated and actual spot locations taking into account variation in crystal off-sets, tilts, and unit-cell dimensions.

1.2.4.4 Normalisation

Since the Bragg condition is met for many reflections over the diffraction volume at various wavelengths during the experiment, it is necessary to scale the intensities to one common wavelength to allow the data to be refined. A reflection (and its symmetry equivalents) can be measured at various wavelengths and the diffracted intensity as a function of wavelength is not uniform but is highly dependent upon the wavelength at

which the diffraction condition is met and therefore on the wavelength spectrum of the instrument, $\Lambda(\lambda)$. The spectrum is a Maxwellian distribution of thermal neutrons with wavelengths in the range 0.5-4.5 Å for KOALA, Figure 1.2.5 shows the spectra for the KOALA and VIVALDI instruments.

These spectra are determined by the use of a standard crystal, typically a ruby, for which unit cell dimensions are known to a high precision. The stability of this spectrum is integral to the success of the normalisation process carried out in the program *LAUE 4* (Piltz, 2011). In the first step, the collection of integrated spot intensities are distributed into groups of equivalents and a number of reflections are culled from the data set based on a number of criteria such as; lying outside the wavelength range chosen for the normalisation, have multiplicities $m > 2$, or having no equivalent or repeat. An initial refinement stage uses the nominal wavelength spectrum to determine scale factors for each Laue pattern. While principally designed to account for variation in exposure times between patterns, this refinement accounts for the significant variation in diffracted intensity as the high-pressure cell is rotated and is capable of scaling data collected with the incident beam directed through the gasket of the cell.

Once the initial image scale factors are determined, further cycles of least-squares refinement are carried out. These cycles refine wavelength-dependent corrections to account for differences in detector efficiency with vertical angle ν. For two diffracted neutron beams of identical intensity, the beam having the larger ν will have a longer path length through the image plate, effectively increasing the detector efficiency and producing an inflated spot intensity. In addition corrections for sample absorption and secondary extinction can also be applied for large high-quality crystals.

At this point it is also possible to refine the instrument wavelength spectrum which is represented as an n-point spline curve, typically $n = 10$, this accounts for the usually minor variations in the incident spectrum and is a helpful diagnostic for the success of the process. This refined spectrum can then be used as the basis for further cycles of normalisation, further refining the data set parameters and reducing merging R-factors. An additional use of the the refined spectrum is in the detection of changes in unit-cell dimensions. The nominal wavelength of each reflection is determined based on the indexing and supplied unit-cell dimensions, if these dimensions are significantly different

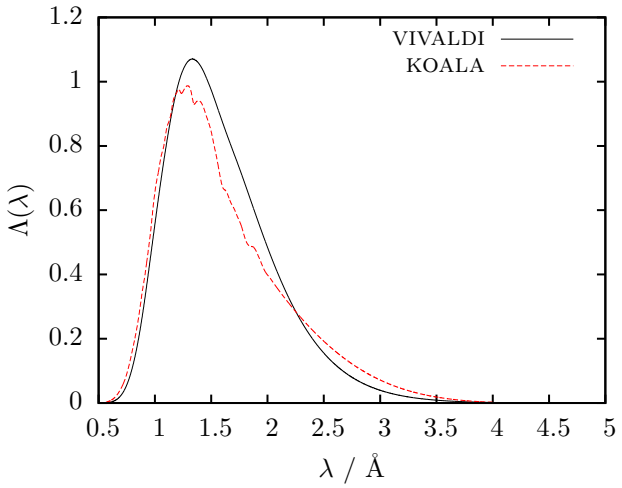

Figure 1.2.5: Normalised instrument wavelength spectra for KOALA and VIVALDI.

for the sample in question there will be a shift in the refined wavelength spectrum *versus* the nominal spectrum.

The final step in the normalisation process involves the removal of outlier reflections from the data set, a reflection is rejected if the difference between reflection intensity I and average reflection intensity $\bar{I}$ was greater than $10\sigma(\bar{I})$. A visual inspection of the outlier reflections is then made and the outliers are added to the list of rejected reflections. The normalisation is then repeated using the updated rejected reflection list and instrument spectrum until the process converges.

1.2.5 High-pressure neutron diffraction

The earliest reported high-pressure neutron diffraction experiment was conducted by Wolfe and Reiffel (1962) at Chalk River Laboratories, Canada on samples of rubidium iodide and rubidium chloride at pressures of up to 0.54 GPa. Later developments were made by Brugger *et al.* (1967) culminating in the development of a dedicated high-pressure instrument at the Idaho Falls Research Reactor, USA. This instrument utilised mechanical choppers to carry out time-of-flight measurements, reaching an eventual maximum pressure of 7.3 GPa, although data were limited to a total of three reflections at this pressure (McCann and Cartz, 1972).

The development of cylindrical clamp cells such as the 'McWhan' type (and variants) increased the maximum available pressures to *ca.* 3 GPa and found use in elastic and

inelastic neutron scattering from both powders and single crystals with typical sample volumes of 500 mm^3 (Nelmes *et al.*, 1987, 1991; Klotz, 2012). In the following decade opposed-anvil cells, often using sapphire rather than diamonds, were pioneered at the Kurchatov Institute, Russia (Goncharenko, 2004). The much smaller sample sizes, up to 1 mm^3, often limited the collected data to a small number of intense low-resolution reflections. These cells were capable of reaching a remarkable maximum pressure of 31 GPa (Glazkov *et al.*, 1988) and could be used for both single-crystal (limited to *ca.* 2 GPa) and powder samples (Ahsbahs, H., 1984; Kuhs *et al.*, 1989).

The 1990's saw the coupling of the intense ISIS spallation source (UK) with the specifically developed Paris-Edinburgh (PE) cell, which has gone on to become the workhorse of high-pressure neutron powder diffraction (Klotz, 2012). Numerous variants have been developed in subsequent years, but in general the cell is capable of experiments up to 10 GPa using sample volumes of approximately 100 mm^3 (Besson *et al.*, 1995). The standard tungsten carbide anvils can be replaced with sintered diamond, and this allows the maximum pressure to be increased to 25 GPa, although the sample volume is reduced to *ca.* 35 mm^3 (Klotz *et al.*, 1995).

Given the success achieved with the PE cell using powder samples, it is unsurprising that a modified version, the so-called VX variant, was specifically developed for use with single-crystals (Klotz *et al.*, 2004). The VX cell provides two windows *ca.* 140° wide around the press axis, and using redesigned toroidal anvils the perpendicular angular access is ±20° up to 8 GPa (Bull *et al.*, 2005). Bull, Guthrie, Nelmes, Loveday, Komatsu, Hamidov and Gutmann (2009) used the VX cell to collect high-pressure single-crystal diffraction data on the time-of-flight Laue diffractometer SXD at ISIS. Samples of KD_2PO_4 and squaric acid ($D_2C_4O_4$) measuring several mm^3 were studied at 5 and 7.5 GPa respectively. The opaque tungsten carbide anvils can be replaced by artificial diamonds for *in situ* sample growth, as demonstrated in a study of a 0.5 mm^3 sample of ice-VI at 1.3 GPa (Bull *et al.*, 2009).

The VX cell is not limited to time-of-flight diffractometers, Bull *et al.* (2011) collected single-crystal neutron diffraction data from a sample of squaric acid measuring 3 mm^3 at pressures up to 10 GPa using the monochromatic D9 instrument at the ILL, France. Measurement of reflection intensities was carried out by sequentially step-

ping through reflections allowing greater collection times for high-resolution and high-leverage peaks. The wavelength of D9 can be tuned and this was exploited to achieve greater data coverage.

Irrespective of type of incident beam, data from the VX cell are limited to quasi-two-dimensional cuts through reciprocal space, with angular restrictions increasing at higher pressures. It is clearly possible to collect high-quality single-crystal data using this cell, however the sample must be carefully chosen such that the scientific query can be answered with such a limited data set. Furthermore, the sample volumes used in these experiments present a significant challenge for single crystal growth, again severely restricting the range of materials which can be studied.

Preliminary work using large-angular-access cells has been carried out on VIVALDI. The panoramic moissanite-anvil cell developed by Geophysical Laboratory (Xu *et al.*, 2002) was trialled using a 0.5 mm^3 sample of natrolite ($Na_2Al_2Si_3O_{10} \cdot 2H_2O$) placed in the cell at 1 bar. The outer steel support of the cell consisted of three support pillars giving a total shaded area of 60° in the horizontal plane, vertical access is limited to ±34°. A series of five patterns were collected for a total of just three hours, integrated data could be used to refine fractional coordinates in agreement with published neutron data to within three estimated standard deviations (McIntyre *et al.*, 2005).

By using the full, polychromatic beam the Laue technique can mitigate some of the difficulties in collecting data from small samples at reasonable rates. The cylindrical image-plate detectors offer distinct advantages over electronic detectors particularly for high-pressure collections. The small point-spread function leads to Bragg spots which are approximately equal to the projected form of the crystal, regardless of intensity. Given the disparity in crystal volume between the anvils and the sample this, in principle, allows easy separation of the three sets of Bragg reflections. A further advantage of the image-plate detectors is the ability to overexpose strong reflections without detrimental effects on the detector. Therefore very strong and very weak scattering can be recorded at the same time and in very close proximity (McIntyre *et al.*, 2005). Given these advantages, high-pressure neutron diffraction using the Laue method could provide an additional tool in the study of crystalline matter at high pressures. The development and application of this technique is the main subject of this thesis.

The structure of this thesis is broadly split into two parts. In Chapter 2, the experimental and data-processing developments and results from the two successful experiments on KOALA are described. Over the course of this development, studies were carried out in parallel on a number of materials with the intention of using the samples as subjects for future high-pressure single-crystal experiments on KOALA. The results of these parallel studies, carried out primarily by high-pressure X-ray diffraction, are presented in the subsequent chapters. Chapter 3 links these two halves and presents a study on the proton-conductor material rubidium hydrogensulfate which was studied at high-pressure and high-temperature with KOALA. While this experiment was ultimately unsuccessful, valuable experience was acquired and the experimental difficulties and further refinements are dealt with in this chapter.

1.3 References

Ahsbahs, H. 1984 *Rev. Phys. Appl. (Paris)* **19**(9), 819–821.

Allan D R and Clark S J 1999 *Phys. Rev. B* **60**, 6328–6334.

Allen E and Bartlett D 2004 *Piezophiles: microbial adaptation to the deep-sea environment* Vol. 3 Eolss Publishers Co Ltd Oxford.

Altomare A, Cascarano G, Giacovazzo C and Guagliardi A 1993 *Journal of Applied Crystallography* **26**(3), 343–350.

Amorós J L 2012 *The Laue Method* Elsevier.

Anderson D L and Hart R S 1976 *Journal of Geophysical Research* **81**(8), 1461–1475.

Arevalo-Lopez A M, Senn M S, Skedd L and Attfield J P 2014 *Zeitschrift für anorganische und allgemeine Chemie* **640**(6), 1164–1167.

Ashcroft N W 1968 *Phys. Rev. Lett.* **21**, 1748–1749.

Bacon G E 1975 *Neutron Diffraction* Oxford : Clarendon Press, 1975.

Bardwell D A, Adjiman C S, Arnautova Y A, Bartashevich E, Boerrigter S X M, Braun D E, Cruz-Cabeza A J, Day G M, Della Valle R G, Desiraju G R, van Eijck B P, Facelli J C, Ferraro M B, Grillo D, Habgood M, Hofmann D W M, Hofmann F, Jose K V J, Karamertzanis P G, Kazantsev A V, Kendrick J, Kuleshova L N, Leusen F J J, Maleev A V, Misquitta A J, Mohamed S, Needs R J, Neumann M A, Nikylov D, Orendt A M, Pal R, Pantelides C C, Pickard C J, Price L S, Price S L, Scheraga H A, van de Streek J, Thakur T S, Tiwari S, Venuti E and Zhitkov I K 2011 *Acta Crystallographica Section B* **67**(6), 535–551.

Baumann J, Gähler R, Kalus J and Mampe W 1988 *Phys. Rev. D* **37**, 3107–3112.

Besson J M, Klotz S, Hamel G, Makarenko I, Nelmes R J, Loveday J S, Wilson R M and Marshall W G 1995 *High Pressure Research* **14**(1-3), 1–6.

Blakeley M 2009 *Crystallography Reviews* **15**(3), 157–218.

Boehler R, Guthrie M, Molaison J, dos Santos A, Sinogeikin S, Machida S, Pradhan N and Tulk C 2013 *High Pressure Research* **33**(3), 546–554.

Boldyreva E V 2004 *Journal of Molecular Structure* **700**(1-3), 151 – 155.

Bourgeois D, Vallone B, Schotte F, Arcovito A, Miele A E, Sciara G, Wulff M, Anfinrud P and Brunori M 2003 *Proceedings of the National Academy of Sciences*

100(15), 8704–8709.

Breit G and Wigner E 1936 *Phys. Rev.* **49**, 519–531.

Bridgman P W 1946 *Rev. Mod. Phys.* **18**, 1–93.

Brugger R, Bennion R and Worlton T 1967 *Physics Letters A* **24**(13), 714 – 717.

Bull C L, Guthrie M, Archer J, Fernandez-Diaz M T, Loveday J S, Komatsu K, Hamidov H and Nelmes R J 2011 *Journal of Applied Crystallography* **44**(4), 831–838.

Bull C L, Guthrie M, Klotz S, Philippe J, Strässle T, Nelmes R J, Loveday J S and Hamel G 2005 *High Pressure Research* **25**(4), 229–231.

Bull C L, Guthrie M, Nelmes R J, Loveday J S, Hamidov H and Gutmann M J 2009 *High Pressure Research* **29**(4), 644–648.

Bull C L, Guthrie M, Nelmes R J, Loveday J S, Komatsu K, Hamidov H and Gutmann M J 2009 *High Pressure Research* **29**(4), 780–791.

Busing W R and Levy H A 1967 *Acta Crystallographica* **22**(4), 457–464.

Capelli S C, Falvello L R, Forcén-Vázquez E, McIntyre G J, Palacio F, Sanz S and Tomás M 2013 *Angewandte Chemie* **125**(50), 13705–13709.

Chadwick J 1932 *Nature* **129**(3252), 312.

Chen J C H, Hanson B L, Fisher S Z, Langan P and Kovalevsky A Y 2012 *Proceedings of the National Academy of Sciences* **109**(38), 15301–15306.

Chung E, Lees M, McIntyre G, Wilkinson C, Balakrishnan G, Hague J, Visser D and Paul D M 2004 *Journal of Physics: Condensed Matter* **16**(43), 7837.

Cioni P and Gabellieri E 2011 *Biochimica et Biophysica Acta (BBA) - Proteins and Proteomics* **1814**(8), 934 – 941.

Cipriani F, Castagna J C, Wilkinson C, Oleinek P and Lehmann M S 1996 *Journal of Neutron Research* **4**(1-4), 79–85.

Craig G A, Woodall C H, McKellar S C, Probert M R, Kamenev K V, Moggach S A, Brechin E K, Parsons S and Murrie M 2015 *Dalton Trans.* **44**, 18324–18328.

Cruickshank D W J, Helliwell J R and Moffat K 1987 *Acta Crystallographica Section A* **43**(5), 656–674.

Cruickshank D W J, Helliwell J R and Moffat K 1991 *Acta Crystallographica Section A* **47**(4), 352–373.

Dobe C, Noble C, Carver G, Tregenna-Piggott P L W, McIntyre G J, Barra A L,

Neels A, Janssen S and Juranyi F 2004 *Journal of the American Chemical Society* **126**(50), 16639–16652.

Dolling G and Brockhouse B N 1962 *Phys. Rev.* **128**, 1120–1123.

Drozdov A, Eremets M and Troyan I 2014 *arXiv preprint arXiv:1412.0460* .

Drozdov A, Eremets M, Troyan I, Ksenofontov V and Shylin S 2015 *Nature* .

Drummond N D, Monserrat B, Lloyd-Williams J H, Rios P L, Pickard C J and Needs R J 2015 *Nat Commun* **6**.

Eckert M 2012 *Acta Crystallographica Section A* **68**(1), 30–39.

Edwards A J 2011 *Australian Journal of Chemistry* **64**(7), 869–872.

Edwards A J, Dhayal R S, Liao P K, Liao J H, Chiang M H, Piltz R O, Kahlal S, Saillard J Y and Liu C W 2014 *Angewandte Chemie* **126**(28), 7342–7346.

Errea I, Calandra M, Pickard C J, Nelson J, Needs R J, Li Y, Liu H, Zhang Y, Ma Y and Mauri F 2015 *Phys. Rev. Lett.* **114**, 157004.

Fabbiani F P A, Buth G, Dittrich B and Sowa H 2010 *CrystEngComm* **12**, 2541–2550.

Fourme R, Girard E and Akasaka K 2012 *Current Opinion in Structural Biology* **22**(5), 636 – 642.

Fourme R, Kahn R, Mezouar M, Girard E, Hoerentrup C, Prangé T and Ascone I 2001 *Journal of Synchrotron Radiation* **8**(5), 1149–1156.

Friedrich W, Knipping P and von Laue M 1912 *Bayer. Akad. Wiss. München* pp. 303–322.

Funnell N P, Dawson A, Marshall W G and Parsons S 2013 *CrystEngComm* **15**, 1047–1060.

Furrer A, Strässle T and Mesot J 2009 *Neutron scattering in condensed matter physics* Vol. 4 World Scientific Publishing Company Incorporated.

Gavezzotti A 2013 *CrystEngComm* **15**, 4027–4035.

Giacovazzo C, Monaco H L, Viterbo D, Scordari F, Gilli G, Zanotti G and Catti M 1993 *Acta Cryst* **49**, 373–374.

Girard E, Kahn R, Mezouar M, Dhaussy A C, Lin T, Johnson J E and Fourme R 2005 *Biophysical Journal* **88**(5), 3562 – 3571.

Glazkov V, Besedin S, Goncharenko I, Irodova A, Makarenko I, Somenkov V, Stishov S and Shil'shtein S S 1988 *JETP Lett* **47**(12).

Goncharenko I N 2004 *High Pressure Research* **24**(1), 193–204.

Graham A J, Tan J C, Allan D R and Moggach S A 2012 *Chem. Commun.* **48**, 1535–1537.

Guennou M, Bouvier P, Chen G S, Dkhil B, Haumont R, Garbarino G and Kreisel J 2011 *Phys. Rev. B* **84**, 174107.

Guthrie M, Boehler R, Molaison J J, dos Santos A M and Tulk C A 2013 *Transactions of the symposium held at the 2013 American Crystallographic Association Annual Meeting* **44**, 149–149.

Hemley R J, Bell P M and Mao H K 1987 *Science* **237**(4815), 605–612.

Hemley R J and Dera P 2000 *Reviews in Mineralogy and Geochemistry* **41**(1), 335–419.

Holzapfel W B 1996 *Reports on Progress in Physics* **59**(1), 29.

Hulme A T, and Price S L 2007 *Journal of Chemical Theory and Computation* **3**(4), 1597–1608.

Jones A O, Blagden N, McIntyre G J, Parkin A, Seaton C C, Thomas L H and Wilson C C 2013 *Crystal Growth & Design* **13**(2), 497–509.

Kenichi T, Kyoko S, Hiroshi F and Mitsuko O 2003 *Nature* **423**(6943), 971–974.

Klose F, Constantine P, Kennedy S J and Robinson R A 2014 *Journal of Physics: Conference Series* **528**(1), 012026.

Klotz S 2012 *Techniques in high pressure neutron scattering* CRC press.

Klotz S, Besson J M, Hamel G, Nelmes R J, Loveday J S, Marshall W G and Wilson R M 1995 *Applied Physics Letters* **66**(14), 1735–1737.

Klotz S, Hamel G and Frelat J 2004 *High Pressure Research* **24**(1), 219–223.

Kuhs W, Ahsbahs H, Londono D and Finney J 1989 *Physica B: Condensed Matter* **156**, 684 – 687.

Leopold P E, Montal M and Onuchic J N 1992 *Proceedings of the National Academy of Sciences* **89**(18), 8721–8725.

Lin T C, Cole J M, Higginbotham A P, Edwards A J, Piltz R O, Pérez-Moreno J, Seo J Y, Lee S C, Clays K and Kwon O P 2013 *The Journal of Physical Chemistry C* **117**(18), 9416–9430.

Loveday J S and Nelmes R J 2003 *High Pressure Research* **23**(1-2), 41–47.

Loveday J S, Nelmes R J, Guthrie M, Belmonte S A, Allan D R, Klug D D, Tse J S

and Handa Y P 2001 *Nature* **410**(6829), 661–663.

Lundegaard L F, Weck G, McMahon M I, Desgreniers S and Loubeyre P 2006 *Nature* **443**(7108), 201–204.

Lynn J W 1994 *Journal of Applied Physics* **75**(10), 6806–6810.

Maynard-Casely H E, Brand H E A and Wallwork K S 2012 *Journal of Applied Crystallography* **45**(6), 1198–1207.

McCann D R and Cartz L 1972 *The Journal of Chemical Physics* **56**(6), 2552–2554.

McIntyre G J, Lemée-Cailleau M H and Wilkinson C 2006 *Physica B: Condensed Matter* **385-386, Part 2**, 1055–1058.

McIntyre G J and Stansfield R F D 1988 *Acta Crystallographica Section A* **44**(3), 257–262.

McIntyre G, Mélési L, Guthrie M, Tulk C, Xu J and Parise J 2005 *Journal of Physics: Condensed Matter* **17**(40), S3017.

Miletich R, Allan D R and Kuhs W F 2000 *Reviews in Mineralogy and Geochemistry* **41**(1), 445–519.

Moffat K, Szebenyi D and Bilderback D 1984 *Science* **223**(4643), 1423–1425.

Moggach S A, Marshall W G, Rogers D M and Parsons S 2015 *CrystEngComm* **17**, 5315–5328.

Moggach S A, Parsons S and Wood P A 2008 *Crystallography Reviews* **14**(2), 143–184.

Mozhaev V V, Heremans K, Frank J, Masson P and Balny C 1996 *Proteins: Structure, Function, and Bioinformatics* **24**(1), 81–91.

Nagae T, Kato C and Watanabe N 2012 *Acta Crystallographica Section F* **68**(3), 265–268.

Navrotsky A 2015 *American Mineralogist* **100**(4), 674–680.

Nelmes R J, McMahon M I, Piltz R O and Wright N G 1991 *Ferroelectrics* **124**(1), 355–360.

Nelmes R J, Tun Z and Kuhs W F 1987 *Ferroelectrics* **71**(1), 125–141.

Niimura N, Karasawa Y, Tanaka I, Miyahara J, Takahashi K, Saito H, Koizumi S and Hidaka M 1994 *Nuclear Instruments and Methods in Physics Research Section A: Accelerators, Spectrometers, Detectors and Associated Equipment* **349**(2), 521 – 525.

Ouladdiaf B, Archer J, McIntyre G, Hewat A, Brau D and York S 2006 *Physica B:*

Condensed Matter **385-386, Part 2**, 1052–1054.

Piltz R O 2011 *Acta Crystallographica Section A* **A67**, C155.

Prescimone A, Milios C, Moggach S, Warren J, Lennie A, Sanchez-Benitez J, Kamenev K, Bircher R, Murrie M, Parsons S and Brechin E 2008 *Angewandte Chemie International Edition* **47**(15), 2828–2831.

Rabinovich D and Lourie B 1987 *Acta Crystallographica Section A* **43**(6), 774–780.

Rodriguez-Carvajal J, Fuentes-Montero L and Čermák P 2014 '*Esmeralda Laue Suite*'.

Rundle R E 1951 *Journal of the American Chemical Society* **73**(9), 4172–4174.

Schobinger-Papamantellos P, Wilkinson C, Ritter C, Tung L D, Buschow K H J and Moze O 2004 *Journal of Physics: Condensed Matter* **16**(36), 6569.

Sears V F 1992 *Neutron News* **3**(3), 26–37.

Silva J L, Foguel D and Royer C A 2001 *Trends in Biochemical Sciences* **26**(10), 612 – 618.

Sotin C, Grasset O and Beauchesne S 1998 *in* B Schmitt, C De Bergh and M Festou, eds, 'Solar System Ices' Vol. 227 of *Astrophysics and Space Science Library* Springer Netherlands pp. 79–96.

Squires G L 1978 *Introduction to the theory of thermal neutron scattering* Cambridge university press.

Wilkinson C, Cowan J A, Myles D A A, Cipriani F and McIntyre G J 2002 *Neutron News* **13**(1), 37–41.

Wilkinson C, Schobinger-Papamantellos P, Myles D, Tung L and Buschow K 2000 *Journal of Magnetism and Magnetic Materials* **217**(1-3), 55–64.

Wolfe G and Reiffel L 1962 Feasibility of neutron diffraction studies in high pressure Technical report DTIC Document.

Xu J, kwang Mao H, Hemley R J and Hines E 2002 *Journal of Physics: Condensed Matter* **14**(44), 11543.

Zheludev A, Barone V, Bonnet M, Delley B, Grand A, Ressouche E, Rey P, Subra R and Schweizer J 1994 *Journal of the American Chemical Society* **116**(5), 2019–2027.

Chapter 2

High-Pressure Single-Crystal Laue Diffraction on KOALA

2.1 Synopsis

The first high-pressure neutron diffraction study in a miniature diamond-anvil cell of a single crystal of size typical for X-ray diffraction is reported. This is made possible by modern Laue diffraction using a large-solid-angle image-plate detector. An unexpected finding is that even reflections whose diffracted beams pass through the cell body are reliably observed, albeit with some attenuation. The cell body does limit the range of usable incident angles, but the crystallographic completeness for a high-symmetry unit cell is only slightly less than for a data collection without the cell. Data collections for two sizes of hexamine single crystals, with and without the pressure cell, and at 300 K and 150 K, show that sample size and temperature are the most important factors that influence data quality. Despite the smaller crystal size and dominant parasitic scattering from the diamond-anvil cell, the data collected allow a full anisotropic refinement of hexamine with bond lengths and angles that agree with literature data within experimental error. This technique is shown to be suitable for low-symmetry crystals, and in these cases the transmission of diffracted beams through the cell body results in much higher completeness values than are possible with X-rays. The way is now open for joint X-ray and neutron studies on the same sample under identical conditions.

2.2 Introduction

Diffraction methods can provide the highest-quality structural information about a crystal on the atomic scale and much work has been carried out to adapt X-ray and neutron diffraction techniques to a variety of challenging sample environments, including high-pressure (McMahon *et al.*, 2013; Guthrie, 2015). X-ray diffraction benefits from the strong photon-electron interaction as well as excellent and relatively inexpensive laboratory sources which can be complemented by very-high-intensity synchrotron sources. In particular, improvements in synchrotron technology have led to the development of dedicated high-pressure beam lines (McMahon, 2015). In many ways neutron diffraction is the reverse; all sources are located at central facilities and are weak compared even to laboratory X-ray tubes. However neutrons can have several advantages over X-rays, the most relevant to high-pressure crystallography being their greater sensitivity to low-Z

atoms, particularly hydrogen, and their greater penetrability through extreme sample environments.

High-pressure neutron powder diffraction has been successfully applied to the discovery of new phases of simple hydrates (Fortes *et al.*, 2007; Loveday *et al.*, 2001) and ices (Fortes *et al.*, 2012; Nelmes *et al.*, 2006). Amongst larger molecular systems it has been applied to the study of polymorphism in amino acids (Funnell *et al.*, 2010; Moggach *et al.*, 2006) and explosives (Davidson *et al.*, 2008).

The Paris-Edinburgh (PE) cell developed in the 1990's has become the standard workhorse of high-pressure neutron powder diffraction and is capable experiments up to 10 GPa with sample volumes of approximately 100 mm^3 (Besson *et al.*, 1995). Replacing the standard tungsten carbide anvils with sintered diamond allows the maximum pressure to be increased to 25 GPa, although using a smaller sample volume of approximately 35 mm^3 (Klotz *et al.*, 1995). These studies have also exploited the construction of new beam lines and instruments dedicated to high-pressure neutron diffraction (Boehler *et al.*, 2013; Guthrie *et al.*, 2013; ISIS, 1996, 1997). However, high-pressure neutron powder diffraction methods have two significant and well-known disadvantages with respect to single-crystal techniques: the loss of information due to peak overlap, which is exacerbated by strain broadening, and the requirement to deuterate the sample.

Deuteration can present a significant synthetic challenge for molecules of even modest complexity and can occasionally induce structural changes in molecular crystals by altering the vibrational properties of individual molecules and of the crystal as a whole. As a result the thermodynamic and mechanical properties of deuterated and undeuterated crystals can be significantly different (Crawford *et al.*, 2009). For high-pressure neutron-diffraction studies of hydrogenated samples, single-crystals are essential.

High-pressure single-crystal neutron diffraction experiments have been conducted with both time-of-flight (Bull *et al.*, 2009) and monochromatic sources (Bull *et al.*, 2011) up to 10 GPa using the VX Paris-Edinburgh press (Klotz *et al.*, 2004). Time-of-flight data were collected on the Laue diffractometer SXD at the ISIS pulsed neutron source on KD_2PO_4 and squaric acid ($D_2C_4O_4$) at 5 and 7.5 GPa (Bull *et al.*, 2009). Further high-pressure data using a monochromatic neutron beam were collected on squaric acid on the D9 single-crystal diffractometer at the Institut Laue-Langevin (ILL)

at 3.5 and 10 GPa. Measurements were carried out by sequentially stepping through the reflections with collection times typically 15-20 minutes per reflection, increasing to up to an hour for high-resolution reflections (Bull *et al.*, 2011). The geometry of the PE-cell constrains application of this technique to situations where the quasi-2D access is sufficient for structural refinements. Diamond/moissanite-anvil cells with much greater angular access have also been utilised in studies using both time-of-flight (Bull *et al.*, 2009) and steady-state Laue methods (McIntyre *et al.*, 2005). Successful as these neutron experiments have been, complementing high-pressure X-ray data with high-pressure neutron data is still fraught with the technical challenge to obtain identical conditions.

The adaption of neutron-sensitive image plates with high spatial resolution has sparked a renaissance in the application of neutron Laue methods at reactor sources with LADI and VIVALDI, both at the ILL (Cipriani *et al.*, 1996; McIntyre *et al.*, 2006), and now with KOALA at ANSTO (Edwards, 2011), which exploit the excellent match between attainable resolution and the low divergence of the guides on which the Laue diffractometers are located. These characteristics allow study of single crystals with volumes several orders of magnitude smaller than conventionally required for neutron diffraction, and the principal aim of this work is to demonstrate that this sensitivity enables single-crystal neutron diffraction data to be collected using samples contained in conventional diamond-anvil cells of the type also used for X-ray measurements, opening the way for joint spectroscopic and diffraction studies using neutrons and X-rays on the exactly same sample.

By using the full polychromatic beam the Laue technique mitigates some of the difficulties in collecting data from small samples at reasonable rates. The cylindrical image-plate detectors offer distinct advantages over electronic detectors particularly for high-pressure collections. The small point-spread function leads to Bragg spots which are approximately equal to the projected form of the crystal, regardless of intensity. Given the disparity in crystal volume between the anvils and the sample, this usually facilitates separation of the corresponding three sets of Bragg reflections. A further advantage of the image-plate detectors is the ability to overexpose strong reflections without detrimental effects on the detector. Therefore very strong and very weak scat-

tering can be recorded at the same time and in very close proximity (McIntyre *et al.*, 2005).

Hexamethylenetetramine (or hexamine, HMT, $C_6H_{12}N_4$) was chosen as the sample material for the initial experiments. The crystal structure was first determined by Dickenson and Raymond in 1923 and has since been the model crystalline system for a variety of fundamental diffraction studies including charge density and neutron diffraction (Dickinson and Raymond, 1923; Duckworth *et al.*, 1970; Terpstra *et al.*, 1993). HMT crystallises in space group $I\bar{4}3m$, with a = 7.028(2) Å (300 K), occupying a site with $\bar{4}3m$ symmetry. The asymmetric unit thus consists of only three atoms, all of which lie on symmetry-constrained positions giving a total of 14 parameters for a fully anisotropic refinement.

Further experiments were carried out using the naturally-occurring amino acid L-arginine (abbreviated as **R**, $C_6H_{14}N_4O_2$, $2(H_2O)$). L-arginine crystallises from aqueous solution as a dihydrate in an orthorhombic unit cell, space-group symmetry $P2_12_12_1$, a = 5.6243(1), b = 11.8081(3), and c = 15.5406(3) Å, V = 1032.09(4) Å^3, whose structure was first reported by Karle & Karle (1964), with a subsequent neutron diffraction study carried out by Lehmann *et al.* as part of the Brookhaven series of amino-acid structure determinations (Lehmann *et al.*, 1973). The L-arginine molecule consists of an amino-acid group with a side-chain of three aliphatic carbon atoms capped by a guanidinium group. In the dihydrate the two water molecules link the repeat units in an infinite ordered chain. This complex, low-symmetry structure requires a total of 289 parameters for a fully anisotropic refinement and represents a significant increase in complexity over HMT.

2.3 Methods

The miniature diamond-anvil cell (mini-DAC, Figure 2.3.1) was a Merrill-Bassett type (Merrill and Bassett, 1974) using beryllium copper alloy for the cell body and backing plate. The alloy used was BERYLCO-25, chosen for its low thermal contraction, with composition 1.8-2.0 weight% Be, a maximum 0.6 weight% Ni, Co and Fe, and the remainder Cu. The diamond anvils were Boehler-Almax cut, 3 mm high with 1 mm

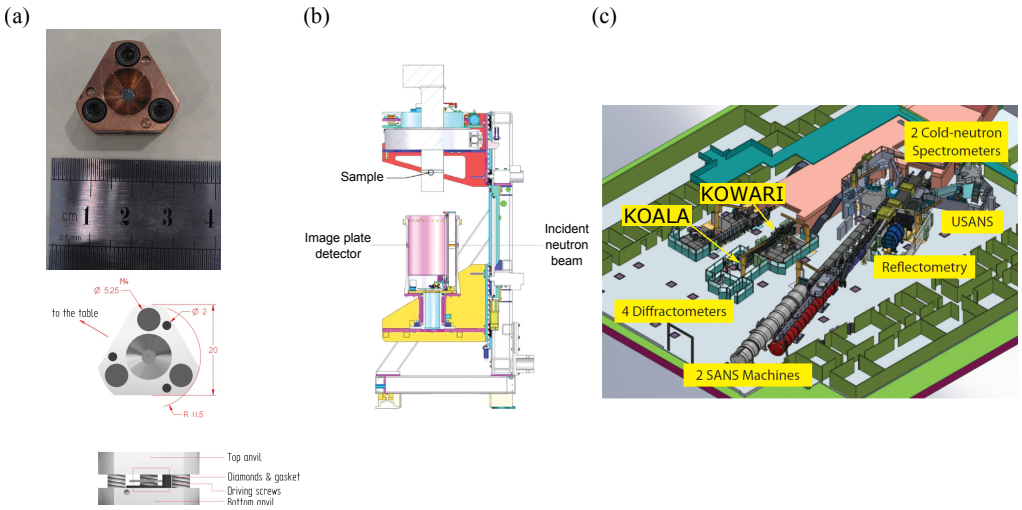

Figure 2.3.1: (a) Photograph of the miniature DAC and diagram of the miniature DAC including cell dimensions in mm; (b) Diagram of KOALA Laue diffractometer opened to allow sample mounting. During operation the sample holder and detector drum assembly are moved together to align the sample and drum center with the incident neutron beam; (c) Layout of neutron scattering instruments at ANSTO. KOALA lies downstream of strain scanner instrument KOWARI.

[001] culet faces set into the body by 1.5 mm (Moggach *et al.*, 2008). The thickness of each half of the cell body was 5 mm, with a height of 20 mm. Alignment was established with three 2 mm diameter Cu-Be guide pins. The backing plate gave optical access through the rear of the anvils with an opening half-angle, ω of 39°.

The small size of the cell allows it to be mounted within the cryostat shields on the KOALA Laue single-crystal diffractometer on the OPAL reactor at ANSTO.

Beyond its reduced size, this cell does not differ in construction from a conventional Merrill-Bassett type DAC used for high-pressure X-ray diffraction, and so the cell can also be mounted on a standard goniometer head for X-ray diffraction measurements. The optical access afforded by the large opening-angle and transparent diamonds allows measurement of pressure by ruby fluorescence as well as other *in situ* spectroscopic measurements (Piermarini *et al.*, 1975).

2.3.1 Crystallisation and data collection geometry

Crystals of undeuterated HMT-h_{12} were selected from commercial samples supplied by Sigma Aldrich. Crystals of undeuterated L-arginine dihydrate were grown by slow-evaporation of a saturated aqueous solution of L-arginine following literature growth studies (Mallik and Kar, 2005).

The KOALA diffractometer consists of a cylindrical detector faced by neutron-sensitive image plates located at the end of a thermal neutron guide; it is essentially a copy of VIVALDI (McIntyre *et al.*, 2006). The incident unmonochromated thermal-neutron beam has a Maxwellian distribution of wavelengths between 0.5 Å, and 4 Å (3.27 - 5.11 meV). The detector area subtends ±144° in the horizontal plane and ±52° out of the plane at the sample, and in a typical experiment four to ten diffraction patterns are collected at different angles of rotation (ϕ) about the instrument's vertical z-axis. In the instrument coordinate system, shown in Figure 2.3.2(a), the origin lies at the sample, the z-axis is vertical pointing upwards along the cylindrical axis of the detector, the incident beam travels along the positive y-axis with the x-axis making a right-handed set. With the mini-DAC mounted it is convenient to define the rotation angle $\phi = 0°$ where the cell axis lies along the incident beam **n**.

The geometry of the cell defines an opening half-angle ω and data are collected with $|\phi| < \omega$ to maximise incident flux at the sample and avoid high background due to scattering if the incident beam passes through the cell body. The angle which the scattered ray, **h** makes with the cell axis is denoted ψ. If $\psi \leq \omega$ the diffracted beam passes only through a diamond, but if $\psi > \omega$, the diffracted beam passes through a diamond and the cell body. The direction of a diffracted beam is defined with respect to the instrument coordinate system by two cylindrical polar angles: γ in the horizontal and ν in the vertical planes, with both equal to zero along the incident beam. A general schematic of the KOALA instrument is given in Figure 2.3.2(a), the reference angles about the mini-DAC are shown in Figure 2.3.2(b).

2.3.2 Sample centring

To centre a sample mounted in the mini-DAC, the cell was rotated around the vertical cylindrical axis to view between the two diamonds and the approximate sample height and off-set determined optically. A series of eighteen 1-hour exposures with x, y, and z off-sets displaced by ± 0.5 and ± 1.0 mm from their initial values were then collected. The intensities of several intense sample spots were monitored at each position and the off-sets where these were maximised taken as the centre. The sample position along z was re-optimised before the collections at 150 K to account for thermal contraction

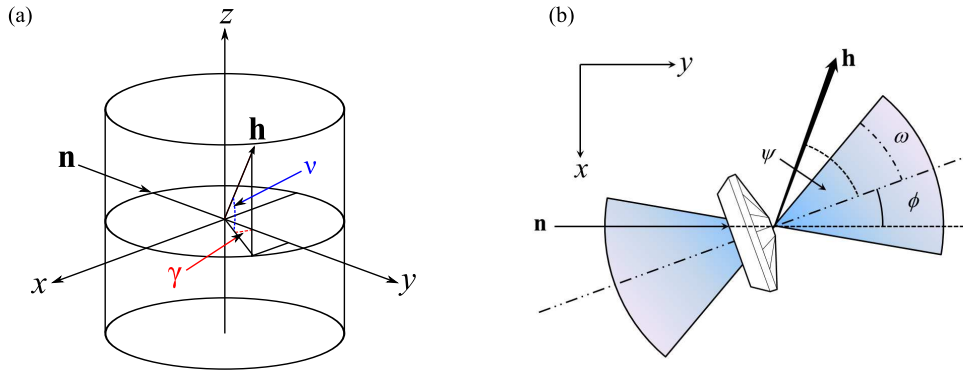

Figure 2.3.2: (a) Schematic of the KOALA instrument. The incident beam, **n** travels along the instrument y-axis. During an experiment the crystal is rotated about the vertical z-axis by an angle $\Delta\phi$ between successive patterns. Each reflection **h** is characterised by the horizontal and vertical polar angles γ, ν; (b) The angle ϕ orients the mini-DAC with respect to the incident beam, ψ is the angle a reflection **h** makes with the mini-DAC axis. The geometry of the mini-DAC creates an opening half-angle ω which limits the direction of the incident beam.

of the sample holder. Figure 2.3.3(a) shows the mini-DAC mounted on the KOALA instrument.

2.3.3 Data collection

Ambient-pressure experiments without the mini-DAC were carried out to gauge the effects of sample size. Data were collected at 300 K using a crystal of HMT-h_{12} of dimensions 0.4 x 0.4 x 0.3 mm^3 (crystal **A**), and a smaller sample measuring 0.3 x 0.2 x 0.15 mm^3 (crystal **B**), which was small enough that it could be accommodated within the gasket of a mini-DAC (Figure 2.3.3(b)). These data sets will be designated $\mathbf{A}_{300}$ and $\mathbf{B}_{300}$, respectively. Both $\mathbf{A}_{300}$ and $\mathbf{B}_{300}$ consisted of four patterns collected for approximately four hours each. Crystal **B** was also cooled to 150 K and four patterns were recorded each for 12 hours (data-set $\mathbf{B}_{150}$). Rotation steps of 20° were used for all three collections. Crystal **B** was then loaded into the mini-DAC using a circular steel gasket of thickness 250 μm, radius 5 mm, and an internal diameter 800 μm, with Fluorinert FC75 as a hydrostatic medium. Pseudo-Kossel lines were observed in the images as a result of increased mosaic spread in the near-perfect anvils while under stress (McIntyre *et al.*, 2015). By reducing primary extinction, the scattering power of the diamonds increases and the strongest diamond reflections in effect become secondary sources. The presence of pseudo-Kossel lines indicated that the sample pressure was

0.25 GPa (Loveday *et al.*, 1990). The applied pressure was low in order to validate the structural parameters against ambient-pressure data and to separate the effects of placing the sample within the cell from the degrading effects of high pressures.

The high-pressure room-temperature data set on crystal **B**, $\mathbf{B}_{\mathrm{DAC},300}$, consisted of six patterns collected at $\phi = -30°$, $-20°$, $-10°$, $0°$, $10°$, and $20°$. Exposure times were 12 hours for the first five and 8 hours for the final pattern. Low-temperature high-pressure data, $\mathbf{B}_{\mathrm{DAC},150}$, were collected at $\phi = -35°$, $-30°$, $-20°$, $-10°$, $0°$, and $35°$ also for 12 hours each.

Two data collections were carried out using crystals of L-arginine dihydrate; ambient pressure data were collected at 300 K using a crystal of 0.6 x 0.5 x 0.5 mm^3 (referred to as $\mathbf{R}_{300}$). A total of ten patterns were collected for two hours each using rotation steps of 20°.

A second crystal of 0.6 x 0.5 x 0.4 mm^3 (referred to as $\mathbf{R}_{\mathrm{DAC}}$) was loaded into the mini-DAC. Again, the applied pressure was low, *ca.* 0.25 GPa. In this experiment the gasket was Ti-Al-V (Al 6 %, V 4 %) alloy 1 mm thick, manufactured by laser cutting and contained a pre-drilled conical hole of no more than 0.5 mm in diameter. This gasket was indented around the pre-drilled hole before being widened with a vertically-mounted drill to 0.7 mm in diameter. The Ti-Al-V alloy was chosen for the very low background exhibited during testing. The data set consisted of twelve patterns collected for 12 hours each at ϕ values of $-30°$ to $-10°$ in $5°$ steps, $-85°$ to $-95°$ in $5°$ steps, and $30°$ to $20°$ in $5°$ steps.

The incident beam was collimated to a diameter of 1 mm at distance of 22 cm before the sample. Currently this is the narrowest collimator available for KOALA and its use is critical to reducing the background intensity; experiments using wider collimators resulted in significantly poorer peak-to-background ratios and patterns often could not be successfully integrated. Further reductions to background scattering could be gained by decreasing the diameter further to reduce scattering from the polycrystalline gasket. Improvements in collimation have been critical to the success of many neutron instruments, particularly when using complex sample environments such as high-pressure cells, and it seems likely further gains can be made on KOALA (Klotz *et al.*, 1995; Boehler *et al.*, 2013).

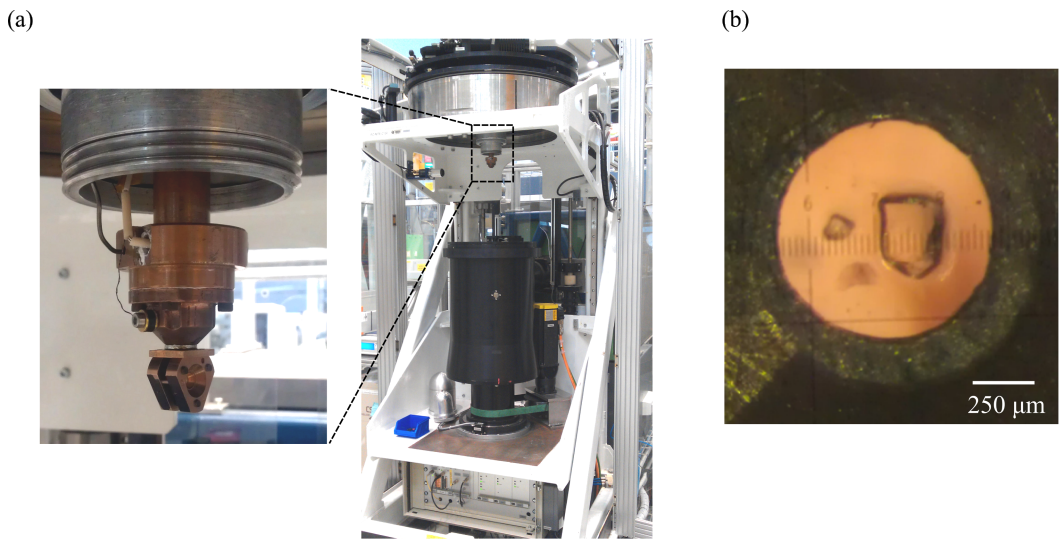

Figure 2.3.3: (a) KOALA quasi-Laue diffractometer on the OPAL reactor ANSTO, inset shows the mini-DAC mounted on the instrument; (b) Microscope photograph of the crystal **B** of HMT along with a chip of ruby in the DAC gasket.

2.3.4 Indexing and processing of data collected at ambient pressure

Ambient-pressure diffraction patterns ($\mathbf{A}_{300}$, $\mathbf{B}_{300}$, $\mathbf{B}_{150}$, and $\mathbf{R}_{300}$) were indexed and processed using the program *LaueG* (Piltz, 2015). Reflection intensities were integrated with a modified two-dimensional version of the minimum $\sigma(I)/I$ algorithm formulated by Wilkinson *et al.* (1988) and Prince *et al.* (1997). The crystallographic resolution limit for integration was determined iteratively by finding the d-spacing at which *ca.* 5 % of integrated reflections had $I/\sigma(I) \geq 5$.

Data were normalised to a single common incident wavelength by comparison of repeat observations and equivalent reflections with wavelengths within the range 0.85-3.5 Å using the program *LAUE4* (Piltz, 2011). Due to the small size of the crystals no absorption or extinction corrections were applied. The crystal structures were refined against $|F|^2$ using all data in *CRYSTALS* (Betteridge *et al.*, 2003). Since the neutron Laue method does not allow accurate empirical determination of the unit-cell volume, unit-cell dimensions were taken from literature values where available, otherwise values calculated from a Berman thermal equation-of-state derived from X-ray powder measurements using *EOSFIT 7.0* (Stevens and Hope, 1975; Berman, 1988; Angel *et al.*, 2014).

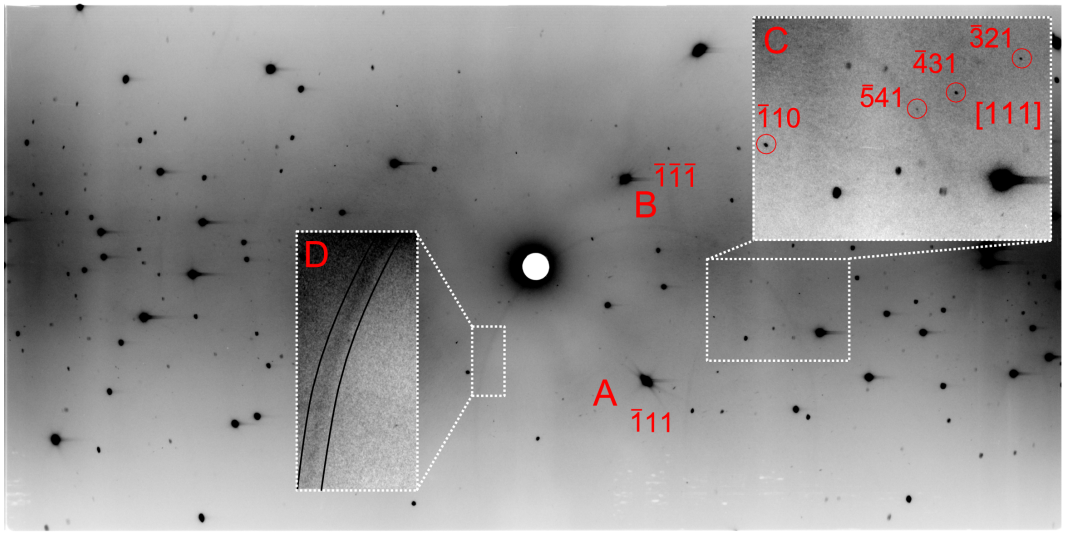

Figure 2.3.4: Laue diffraction pattern recorded at 150 K, $\phi = -30°$ using the mini-DAC. The pattern is dominated by scattering from the two diamond anvils: A marks the $\bar{1}11$ reflection of one anvil; B marks the $\bar{1}\bar{1}\bar{1}$ reflection of the other anvil. Inset C shows four reflections from the sample along the [111] zone, reflection $\bar{5}41$ lies on top of a pseudo-Kossel line. Inset D highlights the same pseudo-Kossel line which is centered on the reflection marked by A. The contrast in each inset is adjusted to highlight certain features.

2.3.5 High-pressure data processing

Processing the high-pressure data presented additional difficulties. The most troublesome features were the very intense, often over-exposed, reflections distributed throughout the pattern arising from the two diamond anvils (Figure 2.3.4). These reflections were intense enough to produce a streaking effect on the read pattern due to long-lived fluorescence from the detector material as the detector cylinder was rotated during the reading process. Pseudo-Kossel lines (§2.3.3) were also observed around some diamond reflections. The fluorescence streaks and pseudo-Kossel lines produced localised areas of marginally increased background, complicating background modelling for sample reflections which straddled the edges of these features. The gasket material itself can produce spots, streaking or other background features depending upon composition and texture. Such features might be easily mistaken for sample reflections during the centring procedure described above (Chapter 3).

2.3.5.1 Indexing and orientation refinement from the high-pressure patterns

The sample crystal was more than 500 times smaller than the total illuminated volume of the diamonds; consequently sample reflections were far weaker and had a smaller

area than all but the weakest diamond reflections, and could therefore be distinguished in data-collection images.

The two sets of intense diamond peaks, typically 50-100 in number, were picked manually and indexed in *LaueG*. Orientation off-sets were refined for each pattern to account for the orbital rotation of the diamonds about the centred sample over the course of the experiment. The diamond reflections were then masked out and the remaining reflections used to index the sample, initially using strong reflections, but then iteratively including progressively weaker data until all sample reflections had been located and indexed. The orientation matrix obtained from analysis of one pattern was then applied to the other patterns by rotation about **z** and then re-refined for each pattern. Comparison of the refined sample xy-offset values for the full set of patterns confirmed the sample had been centered to within 0.07 mm.

2.3.5.2 Development of model spot profiles and integration

Model spot profiles determined using intense sample spots were used to define the areas of integration of nearby weaker spots (Wilkinson *et al.*, 1988). Inaccurate model profiles arise if the data used for profile learning are contaminated by overlapping diamond reflections. Sample peaks in the region of the most intense diamond reflections were over-exposed and omitted on this basis. Reflections in the region of weaker diamond reflections were identified by cross-checking predicted sample- and diamond-reflection coordinates; peaks were considered overlapped if they lay within 10 pixels of each other (pixels are 0.2 x 0.2 mm^2). The figure of 10 pixels was derived by trial and error and found to reject the weak (but relative to the sample, very intense) diamond peaks without rejecting a significant number of genuine sample reflections.

Integration of the high-pressure data was carried out pattern-by-pattern following a similar procedure as described above for the ambient-pressure data sets. Under ambient conditions there is no change in resolution with ϕ. With the high-pressure cell, the path of a ray through the cell body or diamonds is strongly dependent on ϕ and as a result the resolution limit (minimum observable d-spacing by the criterion defined in §2.3.4) changes with ϕ.

2.3.5.3 Cell-body transmission

In high-pressure single-crystal X-ray diffraction the detector is partially masked by the metallic body of the diamond anvil cell, which leads to low completeness for all but high-symmetry cubic samples. The penetrating power of neutrons means that diffracted beams can pass through the small cell body to provide useable diffraction spots on the detector, greatly augmenting data from diffracted beams passing only through the diamond anvils. However, absorption corrections associated with these two classes of reflection are different, and it is necessary to take the difference into account during data reduction.

Figures 2.3.5(a) and (b) illustrate the distribution of reflections on the detector surface for one pattern of data set $\mathbf{B}_{\mathrm{DAC},150}$ (at $\phi = -30°$, corresponding to the observed pattern shown in Figure 2.3.4) and one of data-set $\mathbf{A}_{300}$. Reflection locations are expressed using the horizontal and vertical scattering angles γ and ν and the magnitude of $I/\sigma(I)$ is illustrated using colour. In Figure 2.3.5(a) reflections passing through the diamonds with ($\psi < 39°$ or $\psi > 141°$) are shown as diamonds, and those passing through the cell body ($39° < \psi < 141°$) as circles. The black ellipse and half-ellipse mark the boundaries between these two types of reflection; these are centred at 30° and 150° because $\phi = -30°$ for this image. Figures 2.3.5(c) and (d) show the distributions of $I/\sigma(I)$. In Figure 2.3.5(c), values are plotted against scattering angle ψ rather than 2θ to distinguish between reflections passing through the diamonds and the cell body.

The maximum $I/\sigma(I)$ values of $\mathbf{B}_{\mathrm{DAC},150}$ are lower than those of $\mathbf{A}_{300}$ reflecting the small sample size, and attenuation of the incident and scattered beams by the mini-DAC. The average $I/\sigma(I)$ values for the patterns above are 15.9 for the 157 reflections in the $\mathbf{B}_{\mathrm{DAC},150}$ pattern and 20.4 for the 273 reflections in the $\mathbf{A}_{300}$ pattern. Attenuation of the diffracted beams and the higher background due to scattering from the cell accounts for the 25 % reduction in average $I/\sigma(I)$.

Of the 157 reflections in Figure 2.3.5(a) 30 (19 %) pass only through the diamonds. The very low neutron absorption cross-section of diamond ($\sigma_{abs} = 0.0035$ barn) compared to that of the cell-body (Be-Cu alloy, ca. 99.5% Cu, $\sigma_{abs} = 3.78$ barn for Cu, $\sigma_{abs} = 0.0076$ barn for Be) means that these reflections are essentially unattenuated.

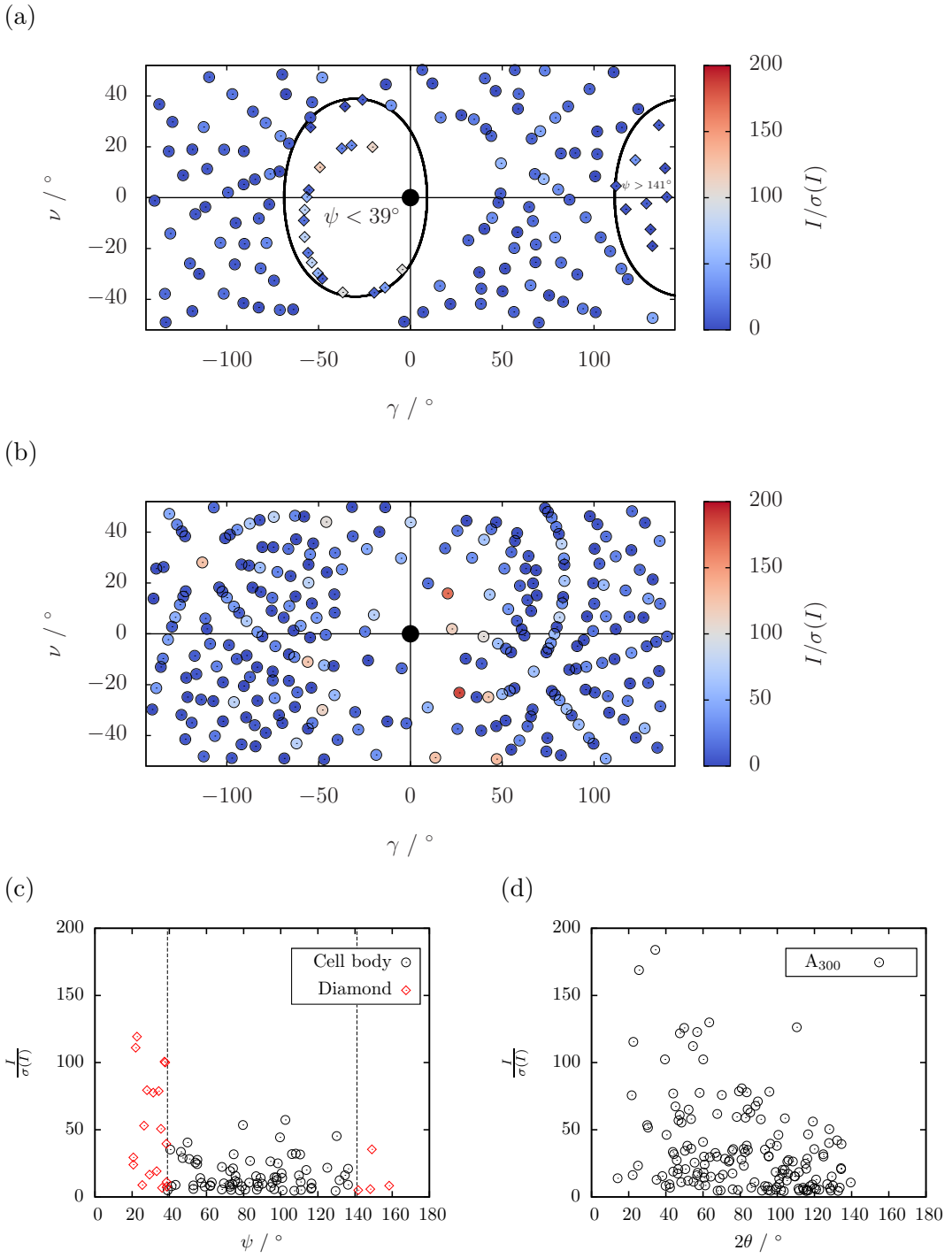

Figure 2.3.5: Simulated patterns for (a) $\mathbf{B}_{\mathrm{DAC},150}$ with $\phi = -30°$ and (b) $\mathbf{A}_{300}$. Reflections are coloured according to $I/\sigma(I)$; reflections passing through the cell body in (a) are shown as circles, those passing through the diamonds are marked by diamonds; (c) A plot of $I/\sigma(I)$ against scattering angle ψ for the pattern (a) for $\mathbf{B}_{\mathrm{DAC},150}$. Scattering angle ψ is used rather than 2θ to make a clear distinction between reflections passing through the diamonds (red diamonds) and the cell body (black circles); (d) Shows the plot of $I/\sigma(I)$ against 2θ for the pattern shown in (b) for $\mathbf{A}_{300}$.

However, the data in Figure 2.3.5(a) and (c) indicate that it is possible to collect reflections over the whole image plate, not just in the areas where reflections pass only through the diamonds, without prohibitive reductions in data quality (*cf.* Figures 2.3.5 (c) and (d)). Some 'back-scattered' reflections pass through the diamond on the incident-beam side of the mini-DAC, visible at $\gamma > 120°$ and are recorded at $\psi > 141°$ (Figures 2.3.5(a) and (c), respectively). This is particularly advantageous, as these reflections are typically high-resolution and composed of a single wavelength. When the cell axis is aligned with the incident beam (*i.e.* in the setting with $\phi = 0°$) these reflections are masked by the erasing lamps and casings.

The majority of the most intense reflections in Figures 2.3.5(a) and (b) are harmonically overlapped and, though they are used for defining integration model profiles, they are omitted from the final intensity data set used for structure analysis.

2.3.5.4 Correction for cell attenuation

The degree of attenuation of a diffracted beam is dependent upon the path length through the cell, the materials encountered en route to the detector, and wavelength of the reflection (attenuation increases with wavelength). For each reflection the path to the detector is characterised by a set of ψ- and ϕ-dependent angles. A set of angular limits were derived from the dimensions of the mini-DAC, dividing the mini-DAC into a series of zones for which the path lengths through the gasket, diamonds, and cell-body can be determined and an attenuation factor defined. Details are available in the Appendix. The wavelength-dependent linear attenuation coefficients of diamond, steel, Ti-Al-V, and beryllium-copper (Be-Cu) alloy were calculated from the chemical compositions and densities using the NIST Neutron Attenuation and Activation tool (NIST, 2005). Since the linear attenuation of diamond is approximately 300 times smaller than that of Be-Cu, the attenuation by the anvils was neglected for all reflections with $\psi < \omega$.

The most intense wavelength in the KOALA spectrum is 1.3 Å and for this wavelength there is no region of the detector plate for which the attenuation factor I/I_0 is less than 0.75, and $I/I_0 > 0.9$ for around 60 % of the detector surface. These figures are wavelength specific; attenuation is greater for longer wavelengths and lower for shorter

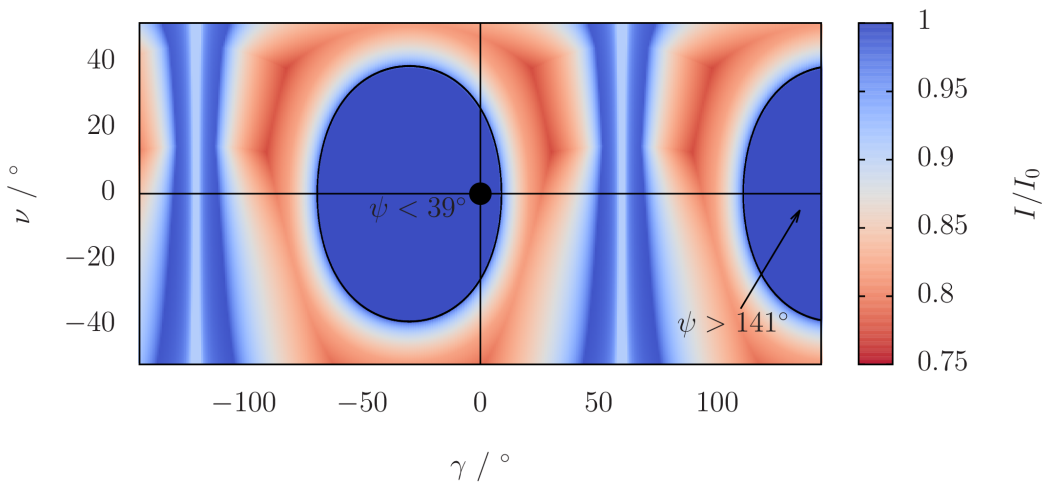

Figure 2.3.6: The attenuation as calculated pixel-by-pixel for $\lambda = 1.3$ Å at $\phi = -30°$, corresponding to Figures 2.3.4 and 2.3.5(a).

wavelengths. For example, in both data sets $\mathbf{B}_{\mathrm{DAC},300}$ and $\mathbf{B}_{\mathrm{DAC},150}$, approximately 90 % of the sample reflections occur at wavelengths less than 2.4 Å, at this approximate upper limit no region of the image plate exhibits $I/I_0 < 0.65$, with $I/I_0 > 0.8$ for around 60 % of the detector area. The distribution of attenuation at $\lambda = 1.3$ Å over the image plate is shown in Figure 2.3.6 for the cell rotated to $\phi = -30°$ for comparison to Figures 2.3.4 and 2.3.5(a).

Attenuation in the upper half of Figure 2.3.6 is greater than in the lower half because the cell is triangular and mounted with its widest section uppermost (Figure 2.3.3(a)). The vertical areas where $I/I_0 \approx 1.0$ in Figure 2.3.6 around $-120°$ and $60°$ correspond to beam paths exiting through the side of the cell between the two halves of the cell body, and for the narrow range $I/I_0 < 1.0$, through the gasket.

There are additional attenuation processes that can occur as a result of the mini-DAC for which corrections were not applied. Firstly, the diamonds diffract intensity away from diffracted sample rays that pass through them if the Bragg condition is met for the wavelength of the diffracted ray. This effect is referred to as a *diffracted-beam event*. Secondly, attenuation arises in the incident beam due to the reactor-side diamond diffracting significant intensity away from the sample, an effect referred to as an *incident-beam event* or *diamond dip*. Diamond dips have been examined for monochromatic X-ray diffraction from both laboratory and synchrotron sources, and in the monochromatic case, occur when the diamonds and sample diffract in the same

setting, reducing diffracted intensities by up to 50% (Loveday *et al.*, 1990). In Laue diffraction, intensity is integrated over wavelength rather than angle of sample rotation, nevertheless such incident- or diffracted-beam events will only occur for a particular sample reflection if the Bragg condition is met by a diamond anvil for the wavelength of the sample reflection. Since the beam divergence in the neutron Laue experiment is usually smaller than the beam divergence in the monochromatic experiment, the likelihood of an event occurring for a particular sample reflection is lower, although the reduction in the integrated observed intensity when an event occurs will be higher. For the complete data set, the mean effect of incident- and diffracted-beam events on the observed sample intensities will be the same for the Laue and monochromatic experiments on the same sample and pressure cell.

A further possible source of error in the intensities of transmitted reflections arises as a result of Bragg edges, which are discontinuities in transmission profiles at certain energies as a result of elastic scattering by the transmitting crystalline material (Fermi *et al.*, 1947). The location of Bragg edges can be easily predicted by Bragg's law, although the exact nature of the transmission *versus* wavelength relationship for a material is highly dependent upon the microstructure, a dependence which is exploited in neutron imaging to determine strain and texture distributions. In copper there are several Bragg edges in the wavelength range used on KOALA (Kockelmann *et al.*, 2007). Measuring transmission profiles through the miniature DAC could provide additional correction terms which are also likely to depend upon ψ to account for varying strain distributions within the cell body.

Wavelength overlaps between sample and diamond reflections were calculated for the five strongest classes of diamond reflections: 111, 220, 311, 400, and 440 pattern-by-pattern. The overlaps were checked against the list of outliers for the merged dataset. During merging and normalisation (see §2.3.5.5), a reflection was rejected as an outlier if the difference between reflection intensity I and average reflection intensity $\bar{I}$ was more than $10\sigma(\bar{I})$. Of the outliers in the normalised data for $\mathbf{B}_{\mathrm{DAC},150}$ and $\mathbf{B}_{\mathrm{DAC},300}$, less than 10 % overlapped with a strong diamond reflection suggesting that the effect of incident-beam events is largely removed during the normalisation procedure.

2.3.5.5 Normalisation

Since the Bragg condition is met for many reflections over the diffraction volume at various wavelengths during the experiment, it is necessary to scale the intensities to one common wavelength for refinement. A reflection (and its symmetry equivalents) can be measured at several wavelengths and the diffracted intensity is dependent upon the wavelength spectrum of the instrument. The normalisation routine in *LAUE4* scales the intensities of measured reflections to a common reference using a least-squares fit to this distribution, the resulting refined incident-beam spectrum can then be used as the basis for a second iteration, improving the merging statistics.

For ambient pressure data, redundancy is typically high enough that the spectrum accepted can be reduced to the most intense band 0.85-1.7 Å, however the high-pressure data sets contain fewer well-measured reflections and so a wider wavelength spectrum from 0.8-3.5 Å is utilised. This introduces weaker, long-wavelength data resulting in increased R_{merge} values, but increases the number of reflections for refinement.

Due to the various attenuations in incident and diffracted beams described above, the effective incident-beam spectrum is significantly different for samples within the mini-DAC. Figure 2.3.7 shows refined incident beam spectra for crystal **B** data sets and the nominal KOALA spectrum. Comparison of data sets $\mathbf{B}_{300}$ and $\mathbf{B}_{300,\mathrm{DAC}}$ shows the detrimental effect due to these attenuations for a relatively sparse data set, $\mathbf{B}_{300}$ consists of 30 groups of equivalent reflections, essentially the same as $\mathbf{B}_{300,\mathrm{DAC}}$ with just 29 groups of equivalent reflections not rejected due to outliers. The large fluctuations in the refined spectrum reflect the absence (or severe attenuation) of data at certain wavelengths, however the effects on the normalisation process are minimal, both data sets produce usable data (§2.4.2). For data sets $\mathbf{B}_{150}$ and $\mathbf{B}_{150,\mathrm{DAC}}$ the improved quality and increased number of reflections (66 and 57 groups of equivalent reflections, respectively) results in refined spectra which closely resemble the nominal spectrum (Figure 2.3.7(b)).

When constrained to the nominal incident-beam spectrum, the normalised reflection intensities are under- or over-inflated to match the spectrum exactly. Allowing the incident beam spectrum to refine removes this constraint and allows the normalisation

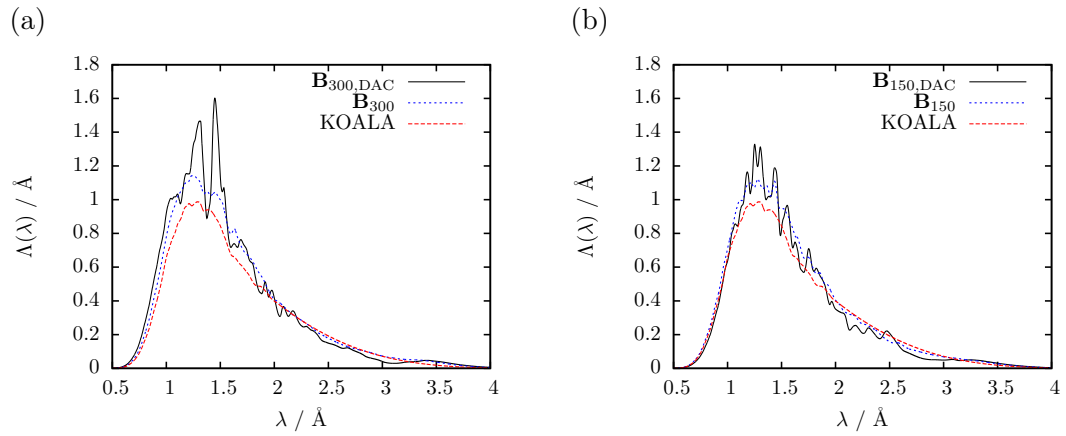

Figure 2.3.7: Refined and nominal incident beam spectra for crystal **B** data sets. (a) Shows data for **B** at 300 K under ambient conditions and within the DAC; (b) Shows data for **B** at 150 K under ambient conditions and within the DAC.

procedure to remove data affected by incident- and diffracted-beam events throughout the data set. While this may result in significant deviations in the refined spectra, this serves as a diagnostic indicator of data quality rather than leading to unusable data as is the case for a constrained normalisation. As shown above, the large number of equivalent data collected by the Laue method allows the normalisation procedure to remove reflections affected by diamond dips and Bragg edges for which no explicit correction has been attempted.

2.4 Results

2.4.1 Ambient-pressure neutron diffraction of HMT

While crystal **A** was large by X-ray standards, it is on the lower limit for usable samples on KOALA. For $\mathbf{A}_{300}$ the resolution limit (§2.3.4) was 0.72 Å, giving a data set with $\langle I/\sigma(I)\rangle = 59.62$; the value of $\langle I/\sigma(I)\rangle$ to a resolution of 1 Å was 119.38. Diffraction data for crystal **B**, which had a volume approximately five times smaller than crystal **A**, extended to 1.04 Å with $\langle I/\sigma(I)\rangle = 46.76$. Cooling substantially improves the statistics for **B**, and at 150 K (data-set $\mathbf{B}_{150}$) data could be integrated to 0.77 Å with $\langle I/\sigma(I)\rangle = 36.99$; $\langle I/\sigma(I)\rangle$ to 1.0 Å was 63.90. Data quality statistics are given for all data sets in Table 2.4.1. Completeness values for Laue diffraction cannot reach beyond the theoretical maximum of 83.3 % due to harmonic overlap (Cruickshank *et al.*, 1987,

Data set	Resolution / Å	R_{merge}	Completeness	Redundancy	$\langle I/\sigma(I)\rangle$ (to 1 Å)	Total number of reflections
$\mathbf{A}_{300}$	0.72	4.3%	74.2%	19.8	59.62 (119.38)	997
$\mathbf{B}_{300}$	1.04	10.3%	74.1%	17.4	46.76	475
$\mathbf{B}_{150}$	0.77	10.8%	73.2%	15.2	36.99 (63.90)	850
$\mathbf{B}_{\mathrm{DAC},300}$	1.04	14.6%	70.4%	24.8	59.13	670
$\mathbf{B}_{\mathrm{DAC},150}$	0.79	19.5%	67.9%	16.6	32.30 (39.83)	878

Table 2.4.1: Crystallographic statistics for all HMT data sets

1991).

The atomic coordinates used to initiate refinement were taken from Cambridge Database (Allen, 2002) entry HXMTAM07 (Terpstra *et al.*, 1993). For $\mathbf{A}_{300}$ all atoms were refined anisotropically without restraints giving a final R-factor ($R1[F > 4\sigma(F)]$) of 3.68 %. However data set $\mathbf{B}_{300}$ at the same temperature consisted of just 20 unique reflections and unrestrained refinement was limited to an isotropic treatment for all atoms, giving a data-to-parameter ratio of 2.5. In comparing data-to-parameter ratios it should be noted that hydrogen atom parameters are refined, unlike most refinements against X-ray data. The R-factor for the free refinement was 6.08 %. The effective data-to-parameter ratio for anisotropic refinement was increased by applying shift-limiting restraints to anisotropic displacement parameters (ADPs), as well as rigid-body and rigid-bond restraints to the C and N atoms. This stabilised a fully anisotropic refinement of all atoms, yielding a final R-factor of 2.72 %.

The 150 K data-set ($\mathbf{B}_{150}$) consisted of 41 unique data, and the model was freely refined with anisotropic displacement parameters for all atoms, yielding $R = 3.46$ % with a data-to-parameter ratio of 2.9.

2.4.2 Diamond-anvil cell data for HMT

The most remarkable result from this study is that there is a no significant reduction in completeness for data collected from the mini-DAC (Table 2.4.1). In contrast to

high-pressure X-ray diffraction, the use of neutrons, which are highly penetrating and can pass through the cell body, allows the observation and incorporation of data without angular restriction. This is particularly advantageous for low-symmetry crystals where the restriction for X-rays leads to very low completeness values; by contrast Laue diffraction is subject to a theoretical maximum completeness of 83.3 % regardless of crystal symmetry, and is only marginally affected by the use of a high-pressure cell.

Data collected from crystal **B** in the mini-DAC at 300 K ($\mathbf{B}_{\mathrm{DAC,300}}$) on KOALA were integrated to a resolution range of 0.90-1.04 Å (the maximum resolution obtained for each image depending on the orientation of the cell, see §2.3.5.2). Given the low number of unique reflections (19), the unrestrained refinement was limited to an isotropic model giving a final $R = 5.90$ %. Use of the restraints described above for anisotropic refinement yields $R = 3.88$ %.

The same integration procedure was applied to $\mathbf{B}_{\mathrm{DAC,150}}$ resulting in a significant improvement in resolution range to 0.79-0.92 Å. At this temperature the data set consisting of 35 unique reflections was used to refine a fully anisotropic model with rigid-body and rigid-bond restraints applied to C and N atoms only, the final R-factor was 7.62 %. For comparison, a freely-refined isotropic model gave $R = 7.97$ %.

The larger R-factor for $\mathbf{B}_{\mathrm{DAC,150}}$ compared to $\mathbf{B}_{\mathrm{DAC,300}}$ reflects the inclusion of numerous weaker high-resolution data. At room temperature weaker data are either absent or rejected as outliers during normalisation. Agreement factors for structures determined by neutron Laue diffraction are usually higher than those determined by monochromatic techniques, and the magnitude of the standard uncertainties of the structural parameters provides a more robust indication of the structure quality (McIntyre *et al.*, 2006). The R-factors for $\mathbf{B}_{300}$ and $\mathbf{B}_{\mathrm{DAC,300}}$ are in fact unusually low reflecting the almost complete absence of weak data.

Location of hydrogen atom positions is one of the principal uses of neutron diffraction, Figure 2.4.1 shows the (a) $F_{obs} - F_{calc}$ and (b) F_{obs} scattering density isosurfaces for $\mathbf{B}_{\mathrm{DAC,150}}$. For a model without H atoms, the difference map clearly identifies the absent hydrogen atom position, and since the sample is undeuterated, the increased contrast of the strong negative scattering length of H aids this identification.

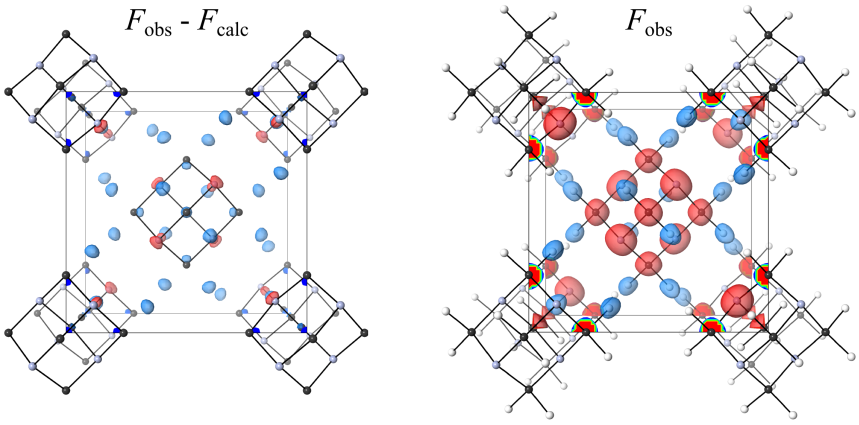

Figure 2.4.1: Isosurface plots of $\mathbf{B}_{DAC,150}$ (a) Fourier difference map for a model phased with just the C and N positions. Strong negative scattering density can be seen at the H atom position, along with other residual density. Isosurface levels are at ±4 fm $^{-3}$; (b) Observed scattering density for $\mathbf{B}_{DAC,150}$ clearly showing the negative scattering density associated with the H atoms, isosurface levels are at ±9 fm $^{-3}$. Positive scattering density is shown in red, negative scattering density in blue. Images were generated in *VESTA 3* (Momma and Izumi, 2011).

2.4.3 Validation of structural parameters of HMT

HMT has not been studied previously by neutron diffraction at 150 K so comparison was made to a reported structure at 160 K by Kampermann *et al.* (1995). Room-temperature data are compared to the refinements of Terpstra *et al.* (1993). Bond lengths and angles of all structures are listed in Table 2.4.2.

$\mathbf{A}_{300}$ reproduces the literature bond distances to within three standard deviations with the largest discrepancy being in the C-H bond, elongated by 0.031(8) Å. The reduction in sample volume between $\mathbf{A}_{300}$ and $\mathbf{B}_{300}$ introduced a significant discrepancy of 0.08(1) in C-H bond length compared to the literature value, while the C-N distance was reproduced accurately. It appears that these discrepancies arise from the short counting times of just four hours per pattern for both crystals. Counting time was increased to 12 hours for $\mathbf{B}_{150}$, as a result all bond lengths and angles for $\mathbf{B}_{150}$ were within 1.5 standard deviations of literature values. Restraining the bond distances to the literature values increases the R-factor for $\mathbf{B}_{150}$ to 3.64 % (+0.18 %) and for $\mathbf{B}_{300}$ the R-factor increases to 3.82 % (+1.1 %). For data set $\mathbf{B}_{DAC,300}$ both C-N and C-H bond distances were statistically equal to the literature values. Likewise $\mathbf{B}_{DAC,150}$ closely reproduced the literature data at 160 K, with all structural parameters within one standard deviation. Despite the higher R-factor, the refined structure for $\mathbf{B}_{DAC,150}$

Bond length or angle	Literature data		$\mathbf{A}_{300}$	$\mathbf{B}_{300}$[3]	$\mathbf{B}_{150}$	$\mathbf{B}_{\mathrm{DAC},300}$[3]	$\mathbf{B}_{\mathrm{DAC},150}$[3]
	300 K[1]	160 K[2]					
N-C / Å	1.462(5)	1.4660(15)	1.462(3)	1.462(3)	1.463(4)	1.454(5)	1.457(4)
C-H / Å	1.071(6)	1.097(3)	1.102(8)	1.148(8)	1.109(8)	1.10(2)	1.133(13)
C-N-C / °	108.0(3)	107.89(9)	107.78(16)	107.08(17)	108.0(2)	107.6(3)	107.6(4)
N-C-N / °	112.4(3)	112.54(9)	112.8(3)	114.1(3)	112.4(4)	113.0(5)	113.1(7)
N-C-H / °	108.1(3)	108.3(4)	108.3(4)	107.8(4)	108.6(4)	108.6(4)	108.7(3)
H-C-H / °	112.2(6)	110.8(7)	110.8(7)	111.7(6)	109.9(7)	109.5(15)	108.8(9)

[1](Terpstra *et al.*, 1993), [2](Kampermann *et al.*, 1995), [3]Values derived from restrained anisotropic refinements.

Table 2.4.2: Bond distances and angles for HMT data collected at ambient pressure and using the mini-DAC with reference literature values.

shows estimated standard deviations that are very similar to those of $\mathbf{B}_{150}$. A graphical summary of the refined structures under various conditions is given in Figure 2.4.2; crystallographic data for each refined structure are given in Table 2.5.1.

(a) A_{300}

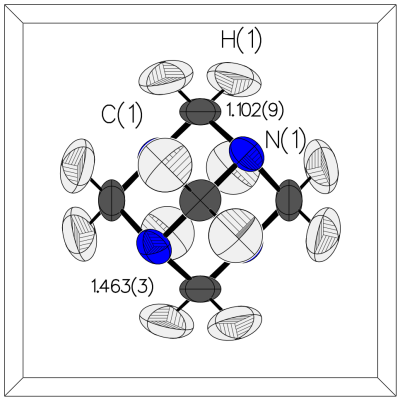

(b) B_{150}

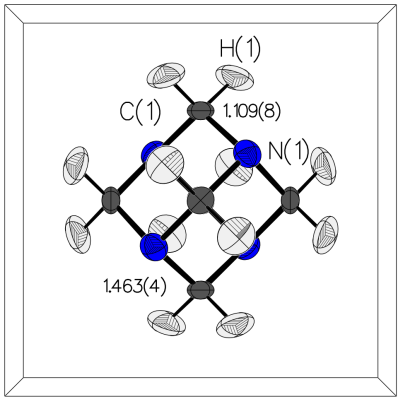

(c) $B_{DAC,300}$

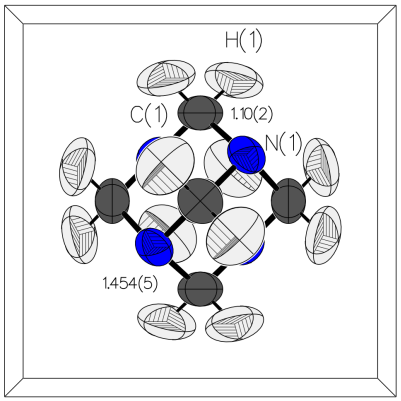

(d) $B_{DAC,150}$

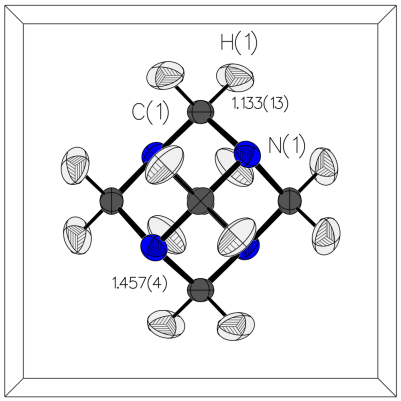

Figure 2.4.2: Summary of refined HMT structures illustrating bond distances. (a) Room-temperature, ambient-pressure structure of $\mathbf{A}_{300}$; (b) 150 K, ambient-pressure structure of $\mathbf{B}_{150}$; (c) Room-temperature, high-pressure structure of $\mathbf{B}_{\mathrm{DAC},300}$; (d) 150 K, high-pressure structure of $\mathbf{B}_{\mathrm{DAC},150}$.

2.4.4 Analysis of anisotropic displacement parameters of HMT

Both data sets collected at ambient conditions, $\mathbf{A}_{300}$ and $\mathbf{B}_{300}$ show similar ADP parameters. Although the C atom in $\mathbf{B}_{300}$ is slightly more oblate, ($U_3/U_1 = 3.99$ *vs.* 2.57 for $\mathbf{A}_{300}$) U_{eq} values for all atoms are within one estimated standard deviation of each other.

For data sets $\mathbf{B}_{150}$ and $\mathbf{B}_{\mathrm{DAC},150}$ there is no statistically significant difference between U_{eq} parameters for C, N, and H atoms and both H atoms show very similar U_3/U_1 values, with $U_3/U_1 = 3.69$ *vs.* 3.45 at ambient pressure.

In refinements at both ambient and high pressure, where the H ADP's were freely refined, there was no significant difference in mean-square displacement along the C-H bonds (*i.e.* $\langle z^2_{C,H}\rangle - \langle z^2_{H,C}\rangle = 0$) implying that the H ADP's pass the Hirshfeld rigid-bond test (Hirshfeld, 1976; Eriksson and Hermansson, 1983). Displacement distances, U_3/U_1, and U_{eq} values for all data sets are given in Table 2.4.3.

Data set	U_{eq} / Å^2			U_3/U_1			$\langle z^2_{A,B}\rangle - \langle z^2_{B,A}\rangle$	
	N	C	H	N	C	H	N-C	C-H
$\mathbf{A}_{300}$	0.0466(7)	0.0516(11)	0.088(3)	2.05	2.57	3.20	0.002(2)	0.017(5)
$\mathbf{B}_{300}$	0.0469(6)	0.0503(12)	0.0907(14)	2.10	3.99	2.25	0.000(2)[1]	0.015(3)
$\mathbf{B}_{150}$	0.0285(8)	0.0220(11)	0.043(2)	1.40	2.42	3.45	0.007(2)	0.005(4)
$\mathbf{B}_{\mathrm{DAC},300}$	0.0545(8)	0.0653(14)	0.1017(19)	1.95	1.89	3.86	0.000(3)[1]	0.007(4)
$\mathbf{B}_{\mathrm{DAC},150}$	0.0262(9)	0.0243(13)	0.0463(17)	1.43	1.56	3.69	0.000(3)[1]	0.001(4)

[1]Value is restrained to 0

Table 2.4.3: Displacement distances, U_3/U_1, and U_{eq} values for refined structures. Values are derived from the restrained anisotropic refinements.

2.4.5 L-arginine dihydrate

Data for crystal $\mathbf{R}_{300}$ could be integrated to a resolution of 0.96 Å, giving a dataset with $\langle I/\sigma(I)\rangle = 20.26$, increasing to 23.11 at 1.0 Å. For the crystal placed inside the cell, $\mathbf{R}_{\mathrm{DAC}}$, the integration limit was also 0.96 Å, with $\langle I/\sigma(I)\rangle = 25.37$, increasing to 27.07 at a resolution of 1.0 Å. Most importantly as can be seen in Table 2.4.4, completeness values are not affected by placing the sample inside the mini-DAC. The increased redundancy and $\langle I/\sigma(I)\rangle$ values for $\mathbf{R}_{\mathrm{DAC}}$ are due to the much longer exposure time for the sample in the DAC.

(a) $\mathbf{R}_{300}$ (b) $\mathbf{R}_{\mathrm{DAC}}$

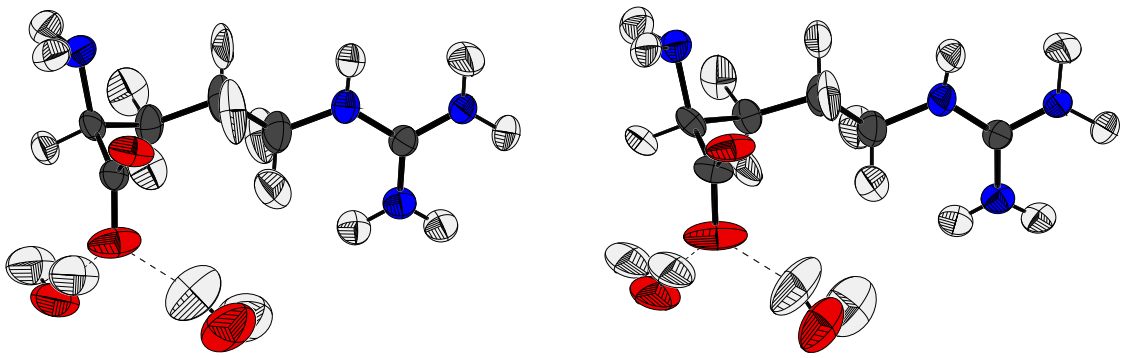

Figure 2.4.3: Refined structures of L-arginine dihydrate from data collected under (a) normal conditions, and (b) from within the mini-DAC.

Data set	Resolution / Å	R_{merge}	Completeness	Redundancy	$\langle I/\sigma(I)\rangle$(to 1 Å)	Total number of reflections
$\mathbf{R}_{300}$	0.96	11.2%	77.0%	16.9	20.26 (23.11)	7872
$\mathbf{R}_{\mathrm{DAC}}$	0.96	19.3%	77.1%	18.4	25.37 (27.07)	8926

Table 2.4.4: Crystallographic statistics for L-arginine dihydrate data sets

Refinement of both data sets required the use of rigid-body and rigid-bond restraints applied to all atoms. In addition, bond-angle and bond-distance restraints were applied to both water molecules. Combined these restraints help alleviate the low data-to-parameter ratios for both data sets: 1.61 for $\mathbf{R}_{300}$ and 1.68 for $\mathbf{R}_{\mathrm{DAC}}$. The resulting agreement factors are $R = 7.50$ % for $\mathbf{R}_{300}$, and $R = 10.11$ % for $\mathbf{R}_{\mathrm{DAC}}$, the final refined asymmetric units are shown in Figure 2.4.3.

Comparison of geometric parameters between $\mathbf{R}_{300}$ and $\mathbf{R}_{\mathrm{DAC}}$ structures shows that all bond lengths are reproduced in the DAC data within statistical significance, and of the 29 interatomic bonds, 25 show differences less than three standard deviations. Likewise, all intermolecular contacts are reproduced within statistical significance.

2.5 Conclusions

We have shown that high-pressure single-crystal neutron diffraction data can be collected from a sample in the miniature DAC with no significant reductions in completeness or resolution compared to equivalent data collected at ambient pressure. The data are of similar quality, as judged by R-factors, geometric parameters, and estimated standard deviations, to those obtained at ambient pressures without the mini-DAC. This is achieved mainly by the ability to measure diffracted intensity directly through the body of the mini-DAC, the geometric simplicity of the mini-DAC facilitating the derivation of the necessary attenuation corrections. The DAC used in this study is in essence identical to those used for conventional high-pressure X-ray diffraction and spectroscopic measurements, so that a full set of characterisation data can be obtained under precisely the same conditions with a single sample loading. The cell would also be suitable for gas-loading techniques.

There are certain experimental difficulties associated with using the miniature DAC. The centring process takes a significant proportion of the experiment time, which is an important consideration when beam time is limited. The procedure also relies on successfully identifying sample spots in the short one-hour exposures used during this process; centring by maximising the intensities of the diamond or gasket reflections mis-centres the sample and leads to unusable data. Determining the orientation of the sample within the DAC by X-ray diffraction prior to the neutron experiment would allow spot positions to be predicted and cross-checked to avoid this pitfall.

The high-pressure methods described are also suitable for low-temperature high-pressure experiments where the improved diffraction quality counter balances the continuing use of small crystals, particularly of high symmetry. The cryofurnace on the KOALA instrument allows the entire cell to be cooled easily, although changes in the cell pressure caused by cooling cannot currently be probed by on-line measurement due to the lack of optical access and the intrinsic limitation of the Laue technique that unit-cell dimensions cannot be known absolutely, only the ratios of $a : b : c$. It should be noted that facilities for carrying out identical low-temperature high-pressure experiments using X-rays are also still far from routine (Ridley and Kamenev, 2014).

For opposed-anvil pressure cells, the cell generates a load which is converted to pressure applied to the sample, the magnitude of this pressure is determined by the combination of culet size, and gasket dimensions and material. The loads generated by the mini-DAC are equal to those generated by standard Merrill-Bassett-type cells which are routinely capable of reaching 20-25 GPa with 600 μm culets and 250 μm gasket holes. The pressure limit for neutron experiments with the mini-DAC will therefore be somewhat reduced by the need to use a larger sample crystal and therefore larger culets and gasket holes, and the upper pressure limit for the current culet and gasket dimensions is estimated to be 5 GPa.

A trial of a panoramic moissanite-anvil cell from the Geophysical Lab was carried out on the VIVALDI diffractometer at ILL using a 1 x 1 x 0.5 mm^3 crystal of natrolite (Xu *et al.*, 2002; McIntyre *et al.*, 2005). This cell design has two advantages over the miniature DAC; firstly that the illuminated volume of the anvils is significantly reduced by directing the beam perpendicular to the cell axis through the gasket; as a result the contaminating anvil reflections are reduced in number and intensity. Also the strongly-supported anvil design allows large samples to be taken well beyond the pressure limits of the miniature DAC. However the optical access afforded by this design would prohibit joint X-ray-neutron studies of the type envisaged for the miniature DAC.

Despite the limitations imposed on the crystal volume, fully anisotropic refinements resulted in C-N and C-H bond lengths within experimental error of the benchmark neutron literature values for the high-symmetry hexamine structure. Further experiments using L-arginine dihydrate demonstrate that the benefits of high completeness extend to more complex, lower-symmetry structures. By using crystals significantly smaller than those used in previous high-pressure single-crystal neutron diffraction studies this technique can be applied to a far wider range of materials where the growth of large (several mm^3) crystals is not possible. The way is now open towards X-ray and neutron diffraction studies of more complex systems at high pressures, giving the capability to perform joint diffraction studies under the same conditions on the same crystal.

Data set	$\mathbf{A}_{300}$	$\mathbf{B}_{300}$	$\mathbf{B}_{150}$	$\mathbf{B}_{\mathrm{DAC},300}$	$\mathbf{B}_{\mathrm{DAC},150}$
Crystal Data					
Formula	$C_6H_{12}N_4$				
Formula weight	140.19				
Crystal system	Cubic				
Space group	$I\bar{4}3m$				
a (Å)	7.028(2)	7.028(2)	6.963(4)	7.028(2)	6.963(4)
V (Å^3)	347.1(3)	347.1(3)	337.6(6)	347.1(3)	337.6(6)
Z	2				
ρ_{calc} (g cm^{-3})	1.341	1.341	1.379	1.341	1.379
Crystal size (mm)	0.4 x 0.4 x 0.3	0.15 x 0.20 x 0.30	0.15 x 0.20 x 0.30	0.15 x 0.20 x 0.30	0.15 x 0.20 x 0.30
Data Collection					
Temperature (K)	300	300	150	300	150
Pressure (GPa)	Ambient	Ambient	Ambient	ca. 0.25	*ca.* 0.25
Radiation (Å)	Neutrons 0.8-3.5 Å				
$h_{min} : h_{max}$	−7:8	−6:6	−9:2	−6:4	−8:5
$k_{min} : k_{max}$	−9:8	−6:6	−6:7	−4:6	−5:7
$l_{min} : l_{max}$	−9:2	−2:6	−9:7	−5:6	−6:8
Total, unique data, R_{int}	997, 81, 0.043	475, 30, 0.103	850, 66, 0.108	670, 29, 0.146	878, 57, 0.195
Observed data ($I > 2\sigma(I)$)	71	30	55	30	46
Refinement					
N_{ref}, N_{par}, N_{ref}/N_{par}	49, 14, 3.5	20, 14, 1.43	41, 14, 2.93	19, 14, 1.36	35, 14, 2.5
($R[F^2 > 2\sigma(F^2)]$)	0.0368	0.0272	0.0346	0.0388	0.0762
$wR2$	0.0956	0.0757	0.0881	0.1039	0.329
S	0.92	1.02	0.98	1.50	1.12
$\Delta\rho_{min}, \Delta\rho_{max}$/ fm Å^{-3}	−0.41, 0.46	−0.35, 0.43	−1.50, 1.07	−0.28, 0.33	−2.01, 3.30

Table 2.5.1: Crystallographic data for all HMT data sets

Data set	$\mathbf{R}_{300}$	$\mathbf{R}_{\mathrm{DAC}}$
Crystal Data		
Formula	$C_6H_{14}N_4O_2$, $2(H_2O)$	
Formula weight	210.23	
Crystal system	Orthorhombic	
Space group	$P2_12_12_1$	
a (Å)	5.6243(11)	
b (Å)	11.808(2)	
c (Å)	15.541(3)	
V (Å^3)	1032.1(3)	
Z	4	
ρ_{calc} (g cm^{-3})	1.353	
Crystal size (mm)	0.5 x 0.5	0.4 x 0.5
	x 0.6	x 0.60
Data Collection		
Temperature (K)	300	
Pressure (GPa)	Ambient	0.25
Radiation (Å)	Neutrons 0.8-3.5 Å	
$h_{min} : h_{max}$	0:5	0:5
$k_{min} : k_{max}$	0:12	0:12
$l_{min} : l_{max}$	0:15	0:156
Total, unique data, R_{int}	7872, 592, 0.181	8926, 726, 0.264
Observed data ($I > 2\sigma(I)$)	482	573
Refinement		
N_{ref}, N_{par}, N_{ref}/N_{par}	464, 289, 1.61	485, 289, 1.68
($R[F^2 > 2\sigma(F^2)]$)	0.0716	0.1011
$wR2$	0.2104	0.3938
S	1.01	1.25
$\Delta\rho_{min}, \Delta\rho_{max}$/ fm Å^{-3}	−0.81, 0.62	−1.03, 1.14

Table 2.5.2: Crystallographic data for L-arginine dihydrate data sets

Appendix - Determining attenuation correction

The path length of a ray passing through the cell-body was determined in a reference axis system attached to the cell where $\mathbf{y}_{cell}$ lies along the cell axis, $\mathbf{z}_{cell}||\mathbf{z}$, and $\mathbf{x}_{cell} = \mathbf{y}_{cell} \times \mathbf{z}_{cell}$. The cell has three-fold symmetry about $\mathbf{y}_{cell}$ and can be divided into six sectors based on the angle, χ_i between the projection of a reflection $\mathbf{h}_i$ in the $\mathbf{xz}_{cell}$ plane of the cell reference system and the $\mathbf{z}_{cell}$ axis (Figure 2.5.1).

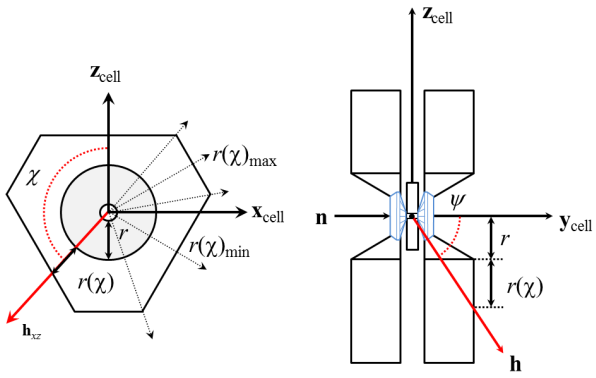

Figure 2.5.1: (Left) The mini-DAC has three-fold rotational symmetry allowing six sectors to be defined on the basis of angle χ; (Right) The value of $r(\chi)$ is used to define a further set of sectors creating limiting values of ψ. Within each sector a trigonometric expression determines the total path length through the cell body. The thickness of the gasket and sample is exaggerated for clarity.

For the cell rotated to an angle ϕ, the cell axis system of unit vectors is determined by applying rotation matrix $\mathbf{\Phi}$ to each axis.

$$\mathbf{x}_{cell} = \mathbf{\Phi} \cdot \mathbf{x} = \begin{pmatrix} \cos\phi & \sin\phi & 0 \\ -\sin\phi & \cos\phi & 0 \\ 0 & 0 & 1 \end{pmatrix} \cdot \begin{pmatrix} 1 \\ 0 \\ 0 \end{pmatrix} \tag{2.5.1}$$

$$\mathbf{y}_{cell} = \mathbf{\Phi} \cdot \mathbf{y} = \begin{pmatrix} \cos\phi & \sin\phi & 0 \\ -\sin\phi & \cos\phi & 0 \\ 0 & 0 & 1 \end{pmatrix} \cdot \begin{pmatrix} 0 \\ 1 \\ 0 \end{pmatrix} \tag{2.5.2}$$

$$\mathbf{z}_{cell} = \mathbf{\Phi} \cdot \mathbf{z} = \begin{pmatrix} \cos\phi & \sin\phi & 0 \\ -\sin\phi & \cos\phi & 0 \\ 0 & 0 & 1 \end{pmatrix} \cdot \begin{pmatrix} 0 \\ 0 \\ 1 \end{pmatrix} \tag{2.5.3}$$

The model of the cell is constructed from a $\chi-$independent section denoted r (5.25 mm) and a χ-dependent length, $r(\chi)$ to account for the change in cell shape with rotation about $\mathbf{y}_{cell}$ between upper and lower limits of 6.25 and 3.25 mm. For each reflection, the detector coordinates ($x_{D,i}$, $z_{D,i}$) and radius R, determine the ray $\mathbf{h}_i$ by equations 2.5.4, 2.5.5 and 2.5.6.

$$\gamma = \frac{x_{D,i}}{R} \tag{2.5.4}$$

$$\nu = \arctan\left(\frac{y_{D,i}}{R}\right) \tag{2.5.5}$$

$$\mathbf{h}_i = \begin{pmatrix} R\sin\gamma \\ R\cos\gamma \\ R\sin\nu \end{pmatrix} \tag{2.5.6}$$

The angles χ_i and ψ_i and consequently value of $r(\chi_i)$:

$$\chi_i = \arccos\left(\frac{\mathbf{h}_{xz,d}\cdot\mathbf{z}_{cell}}{|\mathbf{h}_{xz,d}||\mathbf{z}_{cell}|}\right) \tag{2.5.7}$$

$$\psi_i = \arccos\left(\frac{\mathbf{h}_{d}\cdot\mathbf{y}_{cell}}{|\mathbf{h}_{d}||\mathbf{y}_{cell}|}\right) \tag{2.5.8}$$

For example, in the range $0^\circ < \chi < 45^\circ$ $r(\chi)$ is given by equation 2.5.9, $r(\chi)_{min}$ is determined at 0°, $r(\chi)_{max}$ at 60°. The other limiting angles are $\chi = 75^\circ$, 120°, and 165° between which similar expressions are used with $r(\chi)_{min}$ or $r(\chi)_{max}$ as appropriate.

$$r(\chi) = \frac{r + r(\chi)_{min}}{\cos\chi} - r \tag{2.5.9}$$

For the backing-plate thickness, cell body separation, gasket dimensions, and $r(\chi_i)$ a set of limiting ψ_i angles are calculated to determine whether the diffracted ray passes through the diamonds, gasket, and cell body.

For rays passing through the cell body, the path length is determined by calculating points of intersection with the cell faces. Path lengths through the gasket are calculated

by a simple trigonometric expression. Once the path lengths through the cell body $l_{i,cb}$, diamonds $l_{i,d}$, and gasket $l_{i,g}$, are determined, the attenuation for each reflection i is then calculated using the expression 2.5.10. Since the attenuation due to the diamonds is so low relative to the gasket and cell body, this term is omitted for $\psi > \omega$. The guide pins (Cu-Be) and screws (Fe) are omitted from the model. The gasket was circular in shape simplifying the correction term. Details are given in Tables 2.5.3 and 2.5.4.

$$a_i(\psi_i, \chi_i, \lambda_i) = \frac{I}{I_0} = e^{-\mu_{cb}(\lambda_i) l_{i,cb}(\psi_i,\chi_i)} e^{-\mu_g(\lambda_i) l_{i,g}(\psi_i,\chi_i)} e^{-\mu_d(\lambda_i) l_{i,d}(\psi_i,\chi_i)} \tag{2.5.10}$$

ψ limits for cell body	
$\omega = \arctan\left(\frac{r}{b_t+b_s}\right)$	Cell opening angle
$\psi_1 = \arctan\left(\frac{r+r(\chi)}{b_s}\right)$	High-angle limit of cell body

Cell body model

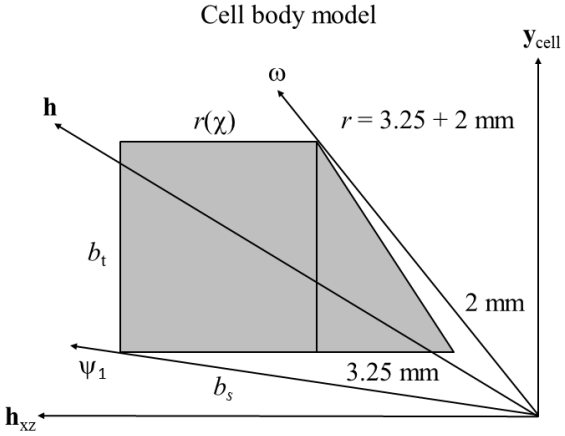

Gasket model

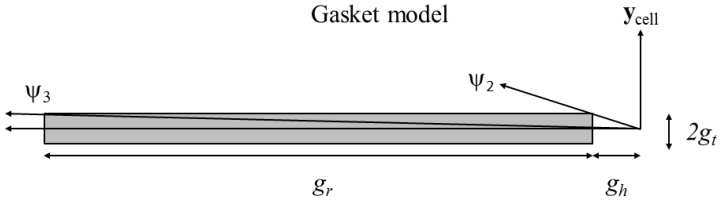

ψ limits for gasket	
$\psi_2 = \arctan\left(\frac{g_h}{g_t}\right)$	Low-angle limit of gasket
$\psi_3 = \arctan\left(\frac{g_h+g_r}{g_t}\right)$	High-angle limit of gasket

Table 2.5.3: Angular limits for the mini-DAC

ψ range	Expression for l_i
$\psi \leq \omega$	$l_{i,d} = \frac{d_h}{\cos\psi}$
$\omega < \psi \leq \psi_1$	Diffracted ray has equation $y_{\mathbf{h}} = \frac{x}{\tan\psi}$ Intercepts are determined between $y_{\mathbf{h}}$ and the two possible entry points: Conic opening face: $y_{cone} = \left(\frac{b_t}{r_{cone}}\right) x + b_s - \left(\frac{b_r d_r}{r_{cone}}\right)$ Cell rear face: $y_r = b_s$ The point furthest from the origin is the first intercept. The second set of intercepts is determined between: Cell front face: $y_f = b_s + b_t$ Cell side wall: $x = r + r(\chi)$ The point closest to the origin in the second intercept. The path length $l_{i,cb}$ is the distance between these points.
$\psi_1 < \psi \leq 90°$	Ray passes between cell bodies, gasket attenuation only.
Gasket terms	**Expression for l_i**
$\psi_2 < \psi \leq \psi_3$	$l_{i,g} = \frac{g_t - \left(g_h \tan(90° - \psi)\right)}{\sin(90° - \psi)}$
$\psi_3 < \psi \leq 90°$	$l_{i,g} = \frac{g_r}{\sin\psi}$
Linear attenuation functions $\mu(\lambda)$	
Diamond	$\mu_d(\lambda) = 0.0005\lambda$
BERYLCO-25	$\mu_{cb}(\lambda) = 0.1611\lambda + 0.042$
(Cu 0.87 Be 0.13, density 8.249 g cm^{-3})	
Ti-Al-V	$\mu_{cb}(\lambda) = 0.18\lambda + 0.159$
(Ti 0.9 Al 0.06 V 0.04, density 4.42 g cm^{-3})	
Iron (density 7.874 g cm^{-3})	$\mu_g(\lambda) = 0.1208\lambda + 0.0332$

Table 2.5.4: Expressions for determining angular limits and path lengths l_i. Calculations are carried out in the plane containing the diffracted beam $\mathbf{h}$ and the cell axis $\mathbf{y}_{cell}$. b_t is the cell body thickness (5 mm), b_s is half the cell body separation (1.625 mm), r is the fixed cell radius (5.25 mm) which is the sum of the radius of the cell opening d_r (2 mm) and the inner cone radius r_{cone} (3.25 mm), $r(\chi)$ is the χ-dependent cell radius (maximum value 6.25 mm, minimum value 3.25), g_t is half the gasket thickness, g_h is the gasket hole radius and g_r is the gasket radius. The diamond height, d_h is 3 mm, set into the body by 1.5 mm.

2.6 References

Allen F H 2002 *Acta Crystallographica Section B* **58**(3 Part 1), 380–388.

Angel R J, Alvaro M and Gonzalez-Platas J 2014 *Zeitschrift für Kristallographie - Crystalline Materials* **229**(5), 405–419.

Berman R 1988 *Journal of Petrology* **29**(2), 445–522.

Besson J M, Klotz S, Hamel G, Makarenko I, Nelmes R J, Loveday J S, Wilson R M and Marshall W G 1995 *High Pressure Research* **14**(1-3), 1–6.

Betteridge P W, Carruthers J R, Cooper R I, Prout K and Watkin D J 2003 *Journal of Applied Crystallography* **36**(6), 1487.

Boehler R, Guthrie M, Molaison J, dos Santos A, Sinogeikin S, Machida S, Pradhan N and Tulk C 2013 *High Pressure Research* **33**(3), 546–554.

Bull C L, Guthrie M, Archer J, Fernandez-Diaz M T, Loveday J S, Komatsu K, Hamidov H and Nelmes R J 2011 *Journal of Applied Crystallography* **44**(4), 831–838.

Bull C L, Guthrie M, Nelmes R J, Loveday J S, Hamidov H and Gutmann M J 2009 *High Pressure Research* **29**(4), 644–648.

Cipriani F, Castagna J C, Wilkinson C, Oleinek P and Lehmann M S 1996 *Journal of Neutron Research* **4**(1-4), 79–85.

Crawford S, Kirchner M, Bläser D, Boese R, David W, Dawson A, Gehrke A, Ibberson R, Marshall W, Parsons S and Yamamuro O 2009 *Angewandte Chemie International Edition* **48**(4), 755–757.

Cruickshank D W J, Helliwell J R and Moffat K 1987 *Acta Crystallographica Section A* **43**(5), 656–674.

Cruickshank D W J, Helliwell J R and Moffat K 1991 *Acta Crystallographica Section A* **47**(4), 352–373.

Davidson A J, Oswald I D H, Francis D J, Lennie A R, Marshall W G, Millar D I A, Pulham C R, Warren J E and Cumming A S 2008 *CrystEngComm* **10**, 162–165.

Dickinson R G and Raymond A L 1923 *Journal of the American Chemical Society* **45**(1), 22–29.

Duckworth J A K, Willis B T M and Pawley G S 1970 *Acta Crystallographica Section A* **26**(2), 263–271.

Edwards A J 2011 *Australian Journal of Chemistry* **64**(7), 869–872.

Eriksson A and Hermansson K 1983 *Acta Crystallographica Section B* **39**(6), 703–711.

Fermi E, Sturm W and Sachs R 1947 *Physical Review* **71**(9), 589.

Fortes A D, Wood I G, Alfredsson M, Vočadlo L, Knight K S, Marshall W, Tucker M and Fernandez-Alonso F 2007 *High Pressure Research* **27**(2), 201–212.

Fortes A D, Wood I G, Tucker M G and Marshall W G 2012 *Journal of Applied Crystallography* **45**(3), 523–534.

Funnell N P, Dawson A, Francis D, Lennie A R, Marshall W G, Moggach S A, Warren J E and Parsons S 2010 *CrystEngComm* **12**, 2573–2583.

Guthrie M 2015 *Journal of Physics: Condensed Matter* **27**(15), 153201.

Guthrie M, Boehler R, Tulk C A, Molaison J J, dos Santos A M, Li K and Hemley R J 2013 *Proceedings of the National Academy of Sciences* **110**(26), 10552–10556.

Hirshfeld F L 1976 *Acta Crystallographica Section A* **32**(2), 239–244.

ISIS 1996 *ISIS 96 - ISIS Facility Annual Report 1995-96* **RAL-TR-96-050**, 61–62.

ISIS 1997 *ISIS 97 - ISIS Facility Annual Report 1996-97* **RAL-TR-97-050**, 28–29.

Kampermann S P, Sabine T M, Craven B M and McMullan R K 1995 *Acta Crystallographica Section A* **51**(4), 489–497.

Karle I L and Karle J 1964 *Acta Crystallographica* **17**(7), 835–841.

Klotz S, Besson J M, Hamel G, Nelmes R J, Loveday J S, Marshall W G and Wilson R M 1995 *Applied Physics Letters* **66**(14), 1735–1737.

Klotz S, Hamel G and Frelat J 2004 *High Pressure Research* **24**(1), 219–223.

Kockelmann W, Frei G, Lehmann E, Vontobel P and Santisteban J 2007 *Nuclear Instruments and Methods in Physics Research Section A: Accelerators, Spectrometers, Detectors and Associated Equipment* **578**(2), 421 – 434.

Lehmann M S, Verbist J J, Hamilton W C and Koetzle T F 1973 *J. Chem. Soc., Perkin Trans. 2* pp. 133–137.

Loveday J S, McMahon M I and Nelmes R J 1990 *Journal of Applied Crystallography* **23**(5), 392–396.

Loveday J S, Nelmes R J, Guthrie M, Belmonte S A, Allan D R, Klug D D, Tse J S and Handa Y P 2001 *Nature* **410**(6829), 661–663.

Mallik T and Kar T 2005 *Journal of Crystal Growth* **285**(1-2), 178 – 182.

McIntyre G J, Lemée-Cailleau M H and Wilkinson C 2006 *Physica B: Condensed Matter* **385-386, Part 2**, 1055–1058.

McIntyre G J, Moggach S A, Parsons S and Binns J 2015 'Personal communication'.

McIntyre G, Mélési L, Guthrie M, Tulk C, Xu J and Parise J 2005 *Journal of Physics: Condensed Matter* **17**(40), S3017.

McMahon M I 2015 *Philosophical Transactions of the Royal Society of London A: Mathematical, Physical and Engineering Sciences* **373**(2036).

McMahon M I, Loa I, Stinton G W and Lundegaard L F 2013 *High Pressure Research* **33**(3), 485–500.

Merrill L and Bassett W A 1974 *Review of Scientific Instruments* **45**(2), 290–294.

Moggach S A, Allan D R, Parsons S and Warren J E 2008 *Journal of Applied Crystallography* **41**(2), 249–251.

Moggach S A, Marshall W G and Parsons S 2006 *Acta Crystallographica Section B* **62**(5), 815–825.

Momma K and Izumi F 2011 *Journal of Applied Crystallography* **44**(6), 1272–1276.

Nelmes R J, Loveday J S, Strässle T, Bull C L, Guthrie M, Hamel G and Klotz S 2006 *Nature Physics* **2**(6), 414–418.

NIST 2005 'Compute neutron attenuation and activation'.

Piermarini G J, Block S, Barnett J D and Forman R A 1975 *Journal of Applied Physics* **46**(6), 2774–2780.

Piltz R O 2011 *Acta Crystallographica Section A* **A67**, C155.

Piltz R O 2015 'Personal communication'.

Prince E, Wilkinson C and McIntyre G J 1997 *Journal of Applied Crystallography* **30**(2), 133–137.

Ridley C J and Kamenev K V 2014 *Zeitschrift für Kristallographie - Crystalline Materials* **229**(3), 171–199.

Stevens E D and Hope H 1975 *Acta Crystallographica Section A* **31**(4), 494–498.

Terpstra M, Craven B M and Stewart R F 1993 *Acta Crystallographica Section A* **49**(5), 685–692.

Wilkinson C, Khamis H W, Stansfield R F D and McIntyre G J 1988 *Journal of Applied Crystallography* **21**(5), 471–478.

Xu J, Mao H K, Hemley R J and Hines E 2002 *Journal of Physics: Condensed Matter* **14**(44), 11543.

Chapter 3

Study of Hydrogen-Bonded Ferroelectric Rubidium Hydrogensulfate

3.1 Synopsis

The pressure- and temperature-dependent phase transitions in the ferroelectric material rubidium hydrogen sulfate ($RbHSO_4$) were investigated by a combination of neutron Laue diffraction and high-pressure X-ray diffraction. The observation of disordered oxygen atom positions in the hydrogensulfate anions is in agreement with previous spectroscopic measurements in the literature. Contrary to the mechanism observed in other hydrogen-bonded ferroelectric materials, hydrogen atom positions are well-defined and ordered in the paraelectric phase.

Under applied pressure $RbHSO_4$ undergoes a ferroelectric transition before a transition to a third high-pressure phase. The symmetry of this phase has been correctly determined and the structural changes through this transition characterised.

In addition, rubidium hydrogensulfate was the subject of a high-pressure single-crystal experiment on KOALA. The difficulties encountered during this experiment and resulting developments are described.

3.2 Introduction

Rubidium hydrogensulfate, ($RbHSO_4$) is one member of the family of solid-acid proton conductors, $MHAO_4$, where M = Na^+, K^+, Rb^+, Cs^+, or $NH_4{}^+$ and A = S or Se. These materials have attracted attention as model hydrogen-bonded ferroelectric materials and for the superprotonic conduction phases achievable under relatively mild thermodynamic conditions.

Ferroelectric behaviour in $RbHSO_4$ was first reported by Pepinsky & Vedam (1960). Their efforts to understand ferroelectricity in ammonium hydrogen sulfate (NH_4HSO_4) focused on ordering within the N-H...O hydrogen bonds. To their surprise, isomorphous $RbHSO_4$ also showed a low temperature ferroelectric phase without the requirement of cation-anion hydrogen bonds. Further measurements have shown ferroelectric transitions to be prevalent throughout the $MHAO_4$ family (Sinitsyn, 2010). Subsequent dielectric studies have revised the transition temperature, and recent piezoresponse force microscopy settled on the generally accepted Curie temperature of 264 K (Lilienblum *et al.*, 2013).

Initial structural investigations of the $MHAO_4$ family in general focused on low temperatures and to some degree high pressures in order to understand the ferroelectric transitions in these materials. Following the discovery of superprotonic conductivity, the high temperature high pressure regions of the PT phase diagrams were explored using electrical conductivity measurements (Ponyatovskii *et al.*, 1985). Collating over a range of M and A has allowed a general phase diagram to be produced (Sinitsyn, 2010).

Despite the topological similarity between the PT phase diagrams of members of the $MHAO_4$ family, corresponding phases are not necessarily isostructural. $RbHSO_4$ and $RbHSeO_4$ share a phase sequence on cooling: *superprotonic* $\rightarrow$ *paraelectric* $\rightarrow$ *ferroelectric*, which occurs at ambient pressure for $RbHSeO_4$ and at pressures $\geq$0.28 GPa in $RbHSO_4$, reflecting the 'chemical pressure' induced by substituting Se for S (Suzuki *et al.*, 1979). However, neither the paraelectric or ferroelectric phases are isostructural; $RbHSeO_4$ has space group $P1$ in the ferroelectric phase and $I2$ in the paraelectric phase (Waskowska *et al.*, 1980; Brach *et al.*, 1983), the space groups of the corresponding phases in $RbHSO_4$ are Pc (phase II, ferroelectric) and $P2_1/c$ (phase I, paraelectric), respectively. In $RbHSeO_4$ the ferroelectric transition is due to proton ordering over a disordered hydrogen bond in contrast to the proposed mechanism, described below, in $RbHSO_4$ (Itoh and Moriyoshi, 2003).

The ambient-pressure phases of the well-studied analogue $CsHSO_4$ (referred to here as $CsHSO_4$-II and $CsHSO_4$-III) are not isostructural with $RbHSO_4$ and do not exhibit a low-temperature ferroelectric transition, both phases have space group symmetry $P2_1/c$. $CsHSO_4$ also shows a very strong isotopic dependence, with metastable phase $CsHSO_4$-III only observed in the undeuterated material (Chisholm and Haile, 2000). The PT phase-diagram of $RbHSO_4$ is shown in Figure 3.2.1.

Pepinsky & Vedam performed the first structural characterisation of $RbHSO_4$; they determined unit-cell parameters of phase I in both a pseudo-orthorhombic $B2_1/a$ and monoclinic $P2_1/c$ setting. They deduced the ferroelectric transition from phase I to II requires the loss of the 2_1 screw symmetry element and determined the ferroelectric phase must have symmetry Pc, later confirmed by systematic absence analysis (Pepinsky and Vedam, 1960).

The structures of phases I and II were investigated by X-ray and neutron diffraction

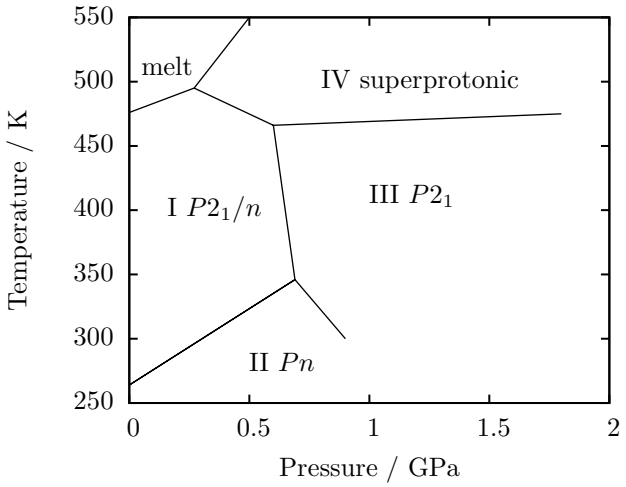

Figure 3.2.1: Pressure-temperature phase-diagram of RbHSO4 following Sinitsyn (2010) and references within.

by Ashmore and Petch (1975). The neutron study revealed that the hydrogen atom positions are fully ordered in the paraelectric phase, in contrast to paraelectric phases in analogous hydrogen-bonded ferroelectrics materials. By analogy with the disorder-order transition observed in NH_4HSO_4, attempts were made to refine a disordered sulfate model, but results were inconclusive.

Dielectric measurements by Ozaki suggested that disorder should play an intrinsic role in the phase transition, and in an attempt to confirm this, Itoh *et al.* report a disordered paraelectric structure for phase I (Ozaki, 1980; Itoh *et al.*, 1995). Itoh *et al.* cite the large anisotropic displacement parameters of the oxygen and hydrogen atoms of one HSO_4^- group, and the successful refinement of a disordered paraelectric phase of NH_4HSO_4, as supporting the disordered model.

In a subsequent study Itoh and Moriyoshi analysed the temperature dependence of anisotropic displacement parameters above and below the Curie temperature, and determined the ferroelectric structure for the first time (Itoh and Moriyoshi, 2003). Again they conclude that one HSO_4^- anion shows disorder however, narrowed down to two oxygen atom positions rather than all four (Itoh and Moriyoshi, 2003).

A Raman spectroscopy study by Toupry *et al.* found the temperature dependence of the O−H frequency to be consistent with a change in ionic orientation. No evidence of a soft mode was found (Toupry *et al.*, 1981).

To complicate matters, an X-ray diffraction study by Nalini and Row (2003) has

cast doubt on the disordered paraelectric model. They find no evidence of distortion in the sulfate geometries or significant residual electron density; they record notable distortions to the sulfate moieties only after cooling into the ferroelectric phase II.

While investigating the pressure dependence of the I $\rightarrow$ II transition, Gesi and Ozawa identified a high-pressure phase which was subsequently investigated by Asahi and Hasebe (Gesi and Ozawa, 1975; Asahi and Hasebe, 1996). This phase III is described as monoclinic $P2_1$.

Clearly there remains some uncertainty as to the structure of the paraelectric phase I, which modern neutron diffraction data can help answer. Confirmation of the ordered proton positions as well as accurate O$-$H bond lengths will go some way to clarifying the mechanism of ferroelectricity in rubidium hydrogen sulfate.

3.3 Methods

Crystals of rubidium hydrogensulfate ($RbHSO_4$) were grown from aqueous solutions of equimolar quantities of $RbSO_4$ and H_2SO_4, $RbHSO_4$ crystallises in large, clear blocks.

X-ray diffraction data were collected on a Bruker SMART APEX II diffractometer with graphite-monochromated Mo Kα radiation (λ = 0.71073 Å), equipped with an Oxford Cryosystems variable-temperature device. High-pressure X-ray diffraction experiments were carried out using a Merrill-Bassett diamond-anvil cell with a tungsten carbide gasket (Merrill and Bassett, 1974; Moggach *et al.*, 2008). The sample and a chip of ruby were loaded with Fluorinert FC70 as the hydrostatic medium. Pressure-dependent ruby fluorescence was used as a pressure measure (Piermarini *et al.*, 1975).

Diffraction data were integrated using *SAINT*. Dynamic masks were applied to account for cell-body shading in the high-pressure data-sets (Dawson *et al.*, 2004). Absorption corrections were carried out in *SADABS* (Sheldrick, 1996). The program *SHADE* was used to identify and discard partially shaded and diamond reflections (Parsons, 2004). Structures were solved by direct methods or charge flipping using *SIR92* or *SUPERFLIP* (Altomare *et al.*, 1993; Palatinus and Chapuis, 2007).

Neutron Laue diffraction data were collected at 300 K and 150 K at ambient pressure on the KOALA Quasi-Laue diffractometer, ANSTO, using a crystal of dimensions 1.2

x 1.1 x 0.8 mm^3. Patterns were collected for 4 hours each, a total of twelve patterns were collected at 300 K, fourteen at 150 K. In both cases the z rotation angle was 15° to account for the low symmetry of these structures.

Laue diffraction patterns were indexed and processed using the program *LaueG* (Piltz, 2011). Reflection intensities were integrated with a modified two-dimensional version of the algorithm formulated by Wilkinson *et al.* (1988) and Prince *et al.* (1997). The data were normalised to a single common incident wavelength using the program *LAUE4* for a wavelength spectrum of 0.85−1.7 Å (Piltz, 2011). For phase I, data were integrated to a resolution of $d = 0.78$ Å. A total of 8517 reflections were merged to a common incident wavelength giving an $R_{merge} = 9.1$ % with a completeness of 77.1 %. Data for phase II were integrated to a resolution of $d = 0.67$ Å. A total of 13194 reflections were normalised and merged to a common incident wavelength with $R_{merge} = 9.7$ % and a completeness of 74.3 %. Laue diffraction suffers an intrinsic harmonic overlap problem that limits completeness values to a theoretical maximum of 83.3 % (Cruickshank *et al.*, 1987, 1991).

All structure refinements were carried out against $|F|^2$ in *CRYSTALS*, initial atomic coordinates were derived from X-ray diffraction data (Betteridge *et al.*, 2003). Hydrogen atoms were refined with standard riding model constraints in the refinements against X-ray data. In the refinements against neutron data H-atom positional and anisotropic displacement parameters were refined freely. Crystal and refinement data are given in Table 3.4.1.

3.3.1 High-pressure single-crystal neutron diffraction

High-pressure single-crystal neutron Laue diffraction data were collected on a sample crystal of 0.4 x 0.4 x 0.4 mm^3 loaded in a 0.5 mm steel gasket with fluorinert FC70 as the hydrostatic medium, the applied pressure was 0.4 GPa. The applied pressure was determined using ruby fluorescence measured using a Raman spectrometer at University of New South Wales. This experiment aimed to collect data at room temperature and 0.4 GPa to study the pressure-induced ferroelectric transition to phase II, before subsequent heating to reach phase IV.

Centering of the sample in the DAC was attempted over a total of fourteen 1 hour

exposures with x, y, and z off-set values incremented around the initial optical centering. Eight patterns were then collected for 12 hours each, at $\phi = -30°$ to $30°$ in $10°$ steps. Collecting data on phase IV required heating the mini DAC to 490 K. Patterns were collected for six temperatures over the heating process from 400 to 490 K. Each measurement was for 4 hours at $\phi = 0°$. Once at 490 K the vertical off-set of the DAC was checked and attempts to recenter the sample were repeated. During the first attempted heating vibrations due to the heating apparatus resulted in the cell shaking loose and required cooling and remounting. As with the room-temperature collections, the centering appears to have been based on scattering from the gasket and no discernible diffraction pattern was collected for the sample reheated to 490 K.

As mentioned in Chapter 2, scattering from the gasket material can result in significant structured scattering in the diffraction patterns; this is particularly detrimental during the indexing process where the sample centering is based on optimising the few observed reflections not originating from the diamonds. During the centring of the $RbHSO_4$ sample, peaks arising from the gasket material were used to optimise the sample position and as a result the patterns could not be indexed suggesting the incident beam was directed almost entirely onto the gasket.

Figure 3.3.1 shows a diffraction pattern collected from the sample at 0.4 GPa at room temperature. In the left inset a number of spots are visible at low-angle, these are typically the strongest reflections and are visible after the one hour centering exposures and are used to determine off-sets.

The shape of a peak in Laue neutron diffraction is the projection of the illuminated crystal volume in the direction of diffracted beam direction and so the sample spots should reflect the fairly isotropic sample crystal shape. Many of the peaks in Figure 3.3.1 were misshapen and could therefore be rejected during indexing. However, selecting groups of well-shaped spots on each frame (such as those shown in the right inset of Figure 3.3.1) did not lead to self-consistent indexing solutions and figures of merit were no better than a random orientation.

The difficulties presented by the high-pressure experiments with $RbHSO_4$ prompted the testing of a variety of possible gasket materials to reduce the noise present in the patterns. Samples of stainless steel, Inconel alloy (72% Ni, 14% Cr, 6% Fe), Ti-6Al-4V,

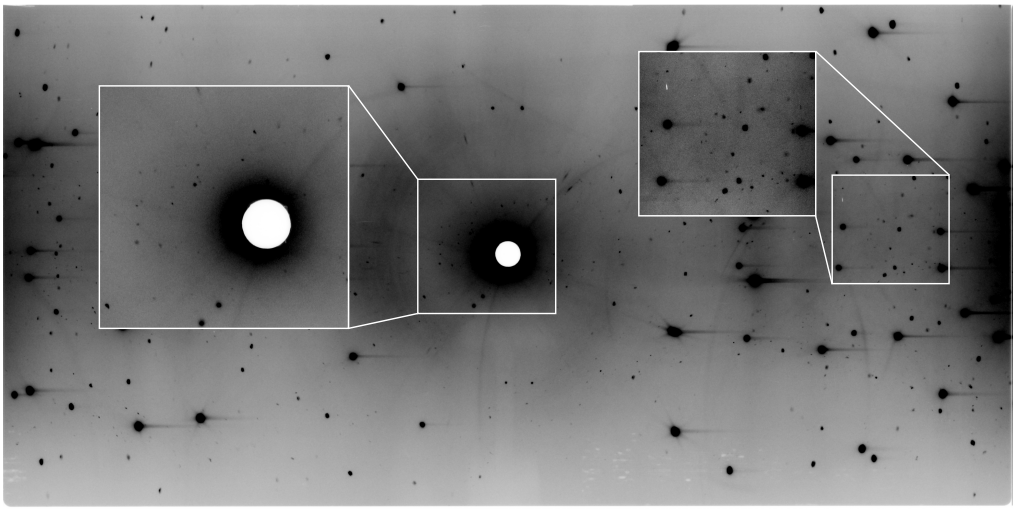

Figure 3.3.1: Laue diffraction pattern collected at 0.4 GPa, $\phi = -10°$. Two insets highlight the large number of peaks visible in the patterns, in particular around the incident beam shown in the left inset. These low-angle peaks were used to center the sample. While there may be peaks present from the sample, there is no consistent indexing possible for these patterns.

and Manganin (86% Cu, 12% Mn, 2% Ni) were selected on the basis of moderate to low scattering densities and mechanical properties. All tested gasket materials were 1 mm thick sheet cut to 10 x 10 mm^2 squares and placed on a standard aluminium pin with fluoridated grease. Ti-Al-V produced the least noise during the tests and so a set of gaskets of 5 x 5 x 1 mm were manufactured by laser-cutting. An initial gasket hole of 0.5 mm was drilled during the cutting process, which was later widened to 0.6 or 0.7 mm using a drill at ANSTO. The Ti-Al-V gaskets were used for experiments with samples of L-arginine dihydrate (Chapter 2).

Determining the orientation of the sample crystal prior to the indexing process on KOALA would further mitigate against miscentering. Single-crystal X-ray diffraction data were collected on the sample of $RbHSO_4$ after the experiment at the University of Sydney, which showed the sample had broken into a number of poorly diffracting fragments during heating and cooling cycles. Development of facilities to collect single-crystal X-ray diffraction data at ANSTO would make this a routine process allowing the input of the orientation matrix directly into *LaueG* prior indexing.

3.4 Results and Analysis

3.4.1 Ferroelectric phase II

The structure of rubidium hydrogensulfate phase II was determined at 150 K in the non-standard polar space group Pn, with a = 14.2651(5), b = 4.5853(2), c = 14.2789(5) Å, and β = 117.999(2)°. In the standard Pc setting, used by Pepinsky and Vedam (1960) and Itoh and Moriyoshi (2003), the unit cell dimensions are a = 14.265, b = 4.585, c = 14.701 Å, and β = 120.955°. The Pn setting was used on account of its (slightly) smaller value of β and because it makes the underlying pseudo-orthorhombic and pseudo-hexagonal symmetry more obvious. Co-set decomposition of mmm to m suggested up to four domains related by two-fold rotations about the orthorhombic axes. Refinement of the twin scale factors showed none of these possible twin domains were populated and gave no improvement in R-factor. No signs of peak splitting were observed indicating the absence of twinning due to the pseudo-hexagonal symmetry.

Neutron diffraction data were used to refine structures derived from ambient-pressure X-ray diffraction and the refined structures from each radiation are the same within error, with the exception of hydrogen-atom positions and displacement parameters. Geometric parameters quoted in the following discussion of the ambient-pressure structures are derived from neutron diffraction data.

The asymmetric unit in phase II consists of four rubidium cations and four hydrogensulfate anions. HSO_4^- anions form infinite hydrogen-bonded chains in the b-direction, running parallel to rows of Rb atoms (Figure 3.4.1(a)). These chains have similar O...H distances ranging from 1.551(6) to 1.580(7) Å, but different ∠O−H...O ranging from 174.2(7)° to 168.0(8)° reflecting the range of orientations adopted by the disordered anions on cooling. The S−O(−H) bond are elongated by 0.12(1) Å on average relative to the other three S−O bonds and O−S−O bond angles range from 103.13(12)° to 113.35(15)°. The remaining twelve S−O bond lengths and range in length from 1.438(7) to 1.466(6) Å. Each Rb atom is coordinated by six HSO_4^- anions, four anions coordinate in a bidentate fashion, the remaining two coordinate *via* a single oxygen atom giving a total coordination number of ten. Rb−O coordination distances vary between 2.881(4) and 3.443(6) Å, with the two shortest Rb−O bonds formed with the

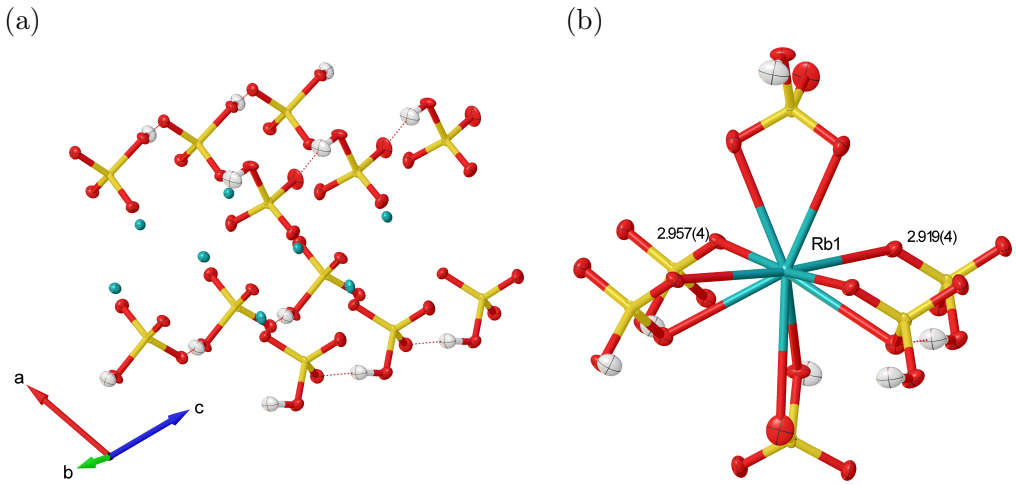

Figure 3.4.1: (a) (a) Four unique hydrogen-bonded chains of hydrogensulfate anions along the b-axis in the asymmetric unit of phase II at 150 K; (b) The ten-atom coordination environment of Rb1, essentially identical to Rb2-4. The shortest Rb-O distances are given in the figure and are formed to the monodentate hydrogensulfate anions. Rb atoms are shown in blue, S shown in yellow, O shown in red, and H shown in white. Ellipsoids are shown at 50 % probability level.

monodentate HSO_4^- anions (Figure 3.4.1(b)). The origin of this structure was selected to match that of phase I to facilitate comparison. Final agreement factor for the neutron diffraction data for phase II is $R1([F > 4\sigma(F)]) = 4.82$ %.

3.4.2 Paraelectric phase I

At 298 K rubidium hydrogen sulfate has unit cell dimensions $a = 14.3602(19)$, $b = 4.6156(6)$, $c = 14.413(2)$ Å, and $\beta = 118.069(8)°$, space group $P2_1/n$, the non-standard setting was used to give a smaller β angle.

In light of the disagreement in the literature regarding the disordered nature of $HS(1)O_4^-$ anion, both ordered and disordered models were refined against the neutron diffraction data, and the corresponding asymmetric units are shown in Figure 3.4.2(a) and (b). The asymmetric unit of phase I consists of two Rb^+ cations and two HSO_4^- anions. The H-bonded chains of anions observed in phase II persist in phase I, and indeed the structures of both phases are generally very similar. Each HSO_4^- is distorted by the elongation of the S−O(−H) bond by 0.121(4) Å. Beyond the elongation of the S−O(−H) bond, the remaining S−O bonds are statistically equal, bond angles within HSO_4^- units range from 103.60(15)° to 116.7(16)°. At 300 K, one rubidium cation (Rb1) is coordinated to six hydrogensulfate anions in the same manner as at 150 K,

Table 3.4.1: Crystal Data and Details of the Structure Determination of $RbHSO_4$ phases I and II by neutron Laue diffraction

Crystal Data	Phase II	Phase I
Formula	$HO_4S{\cdot}Rb$	$HO_4S{\cdot}Rb$
M_r	182.54	182.54
Crystal system	Monoclinic	Monoclinic
Temperature (K)	150	300
Space group	$P2_1/n$ (No. 14)	Pn (No. 7)
a, b, c (Å)	*14.3602(19), 4.6156(6), 14.413(2)*[i]	*14.2651(5), 4.5853(2), 14.2789(5)*[i]
β (°)	*118.069(8)*[i]	*117.999(2)*[i]
Volume (Å^3)	*843.0(2)*[i]	*824.66(6)*[i]
Z	8	8
Radiation type	Neutron, $\lambda = 0.85$ Å	Neutron, $\lambda = 0.85$ Å
Crystal size (mm)	0.80 x 1.10 x 1.20	0.80 x 1.10 x 1.20
	Data collection	
Diffractometer	KOALA diffractometer	KOALA diffractometer
Absorption correction	-	-
No. of measured, independent and observed $[I > 2.0\sigma(I)]$ reflections	8517, 1612, 1073	13194, 2365, 1909
R_{int}	0.091	0.097
$(\sin\theta/\lambda)_{max}$ (Å^{-1})	1.113	1.114
	Refinement	
$R[F^2 > 2\sigma(F^2)]$, $wR(F^2)$, S	0.051, 0.096, 0.91	0.048, 0.112, 0.96
No. of reflections	1073	1909
No. of parameters	146	253
H-atom treatment	All H-atom parameters refined	All H-atom parameters refined
$\Delta\rho_{max}$, $\Delta\rho_{min}$ (e Å^{-3})	0.40, -0.41	0.64, -0.63

[i] Values derived from X-ray diffraction

Computer programs: *MAATEL/ANSTO* control program, *LaueG* (Piltz, 2011), *Argonne boxes* (Wilkinson *et al.*, 1988), *LaueG*, *SIR92* (Altomare *et al.*, 1993), *CRYSTALS* (Betteridge *et al.*, 2003)

four HSO_4^- bonding in a bidentate fashion, the remaining two being monodentate. The other Rb atom (Rb2) is 9-coordinate at 300 K, with three bidentate HSO_4^- and three monodentate HSO_4^- anions. Rubidium-oxygen bond distances vary over a similar range to those in phase II, from 2.924(3) to 3.256(4) Å. The reduction in coordination number is caused by the shift in HSO_4^- orientation through the II-I transition which results in a long Rb-O distance of 4.107(4) Å compared to the bonding distance of 3.443(6) Å in phase II. In phase I, both hydrogen-bonded chains are statistically similar, including the two hydrogen bonds formed by the disordered $HS(1)O_4^-$ anions. For $HS(1)O_4^-$ chains the O...H distance is 1.604(14) Å to O30, and 1.521(15) to O31, $\angle$O−H...O angles are 170.3(5)° and 172.7(5)° respectively. Hydrogen-bond chains formed by $HS(2)O_4^-$ anions have O...H distances of 1.610(4) Å with an $\angle$O-H...O angle of 171.2(3)°.

As Itoh and Moriyoshi note, anomalously large atomic displacement parameters (ADPs) are observed for the oxygen atoms of the $HS(1)O_4^-$ tetrahedron, in particular O(3) which acts as the donor in the O(1)−H(1)...O(3) hydrogen-bonded infinite chain (Figure 3.4.2(a)) (Itoh and Moriyoshi, 2003). These results, along with earlier spectroscopic work by Ozaki (1980) and Toupry *et al.* (1981), are consistent with dynamic disorder in the two oxygen positions (Toupry *et al.*, 1981; Itoh and Moriyoshi, 2003). Two oxygen atoms of $HS(1)O_4^-$ can be refined against the neutron data obtained in the present study over two split positions each with refined occupancies of 0.51(2) and 0.49(2) for O(20/21) and 0.50(2) for O(30/O31). Hydrogen atoms, located in difference maps, occupy well-defined positions with no indication of split occupancy. The final agreement factor for the ordered model was $R = 5.52$ %, that for the disordered model is $R = 5.08$ %. The paraelectric to ferroelectric transition therefore involves the ordering of two alternative anionic orientations representing minima between which $HS(1)O_4^-$ ions are able to oscillate in the paraelectric phase. Below T_c, interaction between HSO_4^- ions within the chains outweighs thermal motion (Toupry *et al.*, 1981). Symmetry analysis using *ISODISTORT* (Campbell *et al.*, 2006) indicates that the phase I to II transition occurs *via* a mode of $\Gamma 2-$ symmetry, though it is also notable that Toupry *et al.* did not observe any mode-softening in their Raman study of this transition.

Comparison of the phase I and II structures in Figure 3.4.2(c) and (d) shows the two disordered sites in the $HS(1)O_4$-I unit are overlapped orientations of the $HS(1)O_4$-II

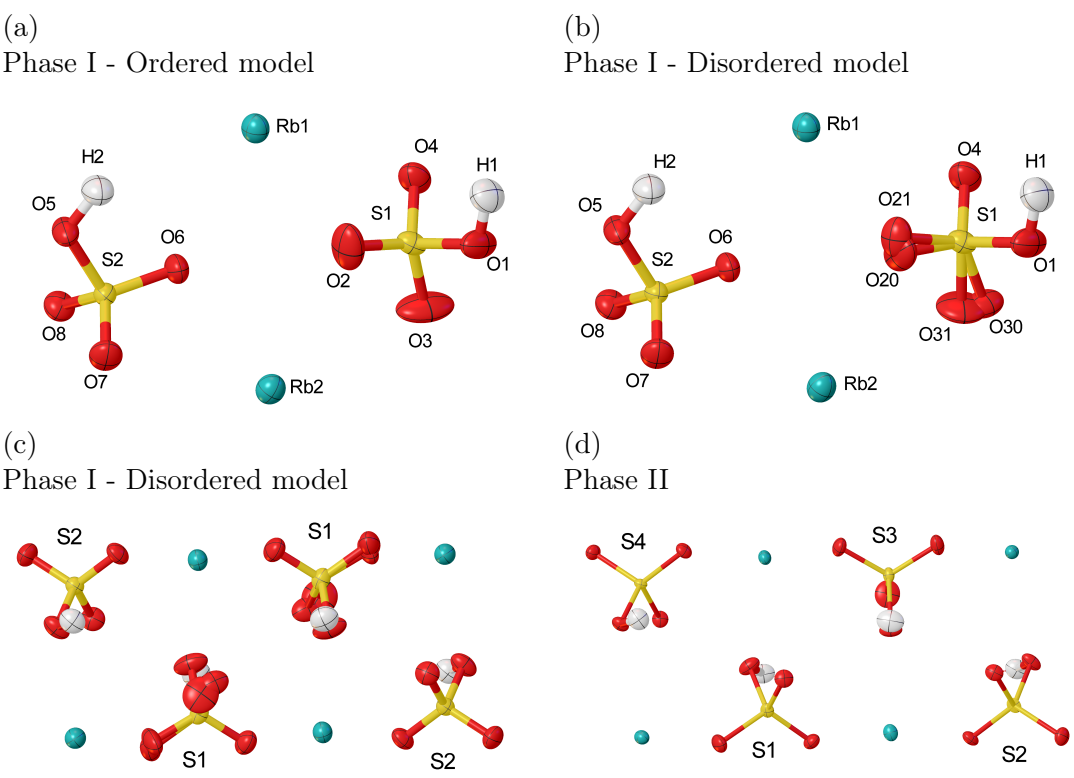

Figure 3.4.2: (a) Asymmetric unit of $RbHSO_4$ phase I, ordered model. The enlarged ADPs of O(2) and O(3) are clearly visible; (b) Asymmetric unit of $RbHSO_4$ phase I, disordered model, splitting of O(2) and O(3) sites results in a lower *R*-factor and is supported by dielectric and Raman spectroscopic measurements. The two orientations of the disordered $HS(1)O_4^-$-I anions shown in (c) are approximately equivalent to the phase II anions $HS(1)O_4^-$-II and $HS(3)O_4^-$-II shown in (d).

and $HS(3)O_4$-II units in the ferroelectric phase II. Figure 3.4.2(c) shows two asymmetric units in phase I related by inversion symmetry. As the sample is cooled half the $HS(1)O_4$-I units occupy the orientation of $HS(1)O_4$-II with the other half occupying the $HS(3)O_4$-II orientation as shown in 3.4.2(d). This breaks the inversion symmetry creating a non-centrosymmetric polar structure and giving rise to spontaneous electric polarisation.

As is implied by the ferroic nature of this transition, this transition occurs *via* a *translationengeleiche* maximal group-subgroup relationship between phases I and II. In such a transition unit-cell dimensions remain essentially fixed and the point group symmetry of the crystal is decreased (Müller, 2013).

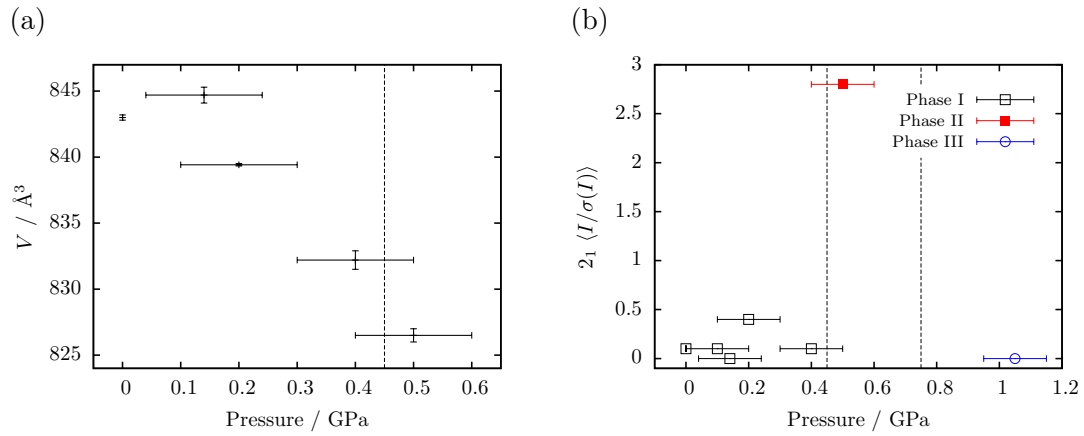

Figure 3.4.3: (a) Change in unit cell volume for phases I and II with pressure; (b) Change in $\langle I/\sigma(I)\rangle$ for reflections in the $0k0$ zone with pressure showing the clear presence of a 2_1 screw symmetry element in phases I and III.

3.4.3 High-pressure X-ray diffraction

$RbHSO_4$ is reported to undergo two phase transitions with pressure at room temperature. Above 0.4 GPa, phase I ($P2_1/n$) undergoes a transition, which has been described as second-order (Kalevitch *et al.*, 1995; Itoh and Moriyoshi, 2003), to phase II (Pn), which then undergoes a first-order transformation at 0.75 GPa to phase III reported to be $P112_1$ (Asahi and Hasebe, 1996).

In this work single-crystal X-ray data were collected at pressures of 0.15(10), 0.2(1), 0.4(1), 0.5(1), and 1.05(10) GPa.

Up to 0.4 GPa the unit cell volume decreases by 10.8(8) Å^3 (1.3 %), axial compression is small, the most significant change is in c with a reduction of 0.052(9) Å, a decreases by 0.026(5) Å, and b remains unchanged within error. The β angle increases by 0.871(3)° (0.73 %). Over the I—II phase transition, the unit-cell volume falls continuously, β decreases by 1.26(4)°, this is accompanied by decreases in a and b of −0.166(7) and −0.021(2) Å respectively, and as a result unit-cell volume falls by −5.7(9) Å^3 (0.7 %) (Figure 3.4.3(a)). Systematic absences were strongly suggestive of a loss of the 2_1 screw axis, although refinements were attempted in both $P2_1/n$ and Pn.

The structure of phase III has previously been described by Asahi and Hasebe (1996) as non-standard monoclinic, $P112_1$, a = 7.360(4), b = 7.346(4), c = 7.756(2) Å, β = 110.86(4)° at 1.00(3) GPa. X-ray diffraction measurements at 1.1(1) GPa have found phase III to be monoclinic, $P2_1/c$, a = 7.3202(7), b = 7.765(2), c = 7.3247(8) Å, β =

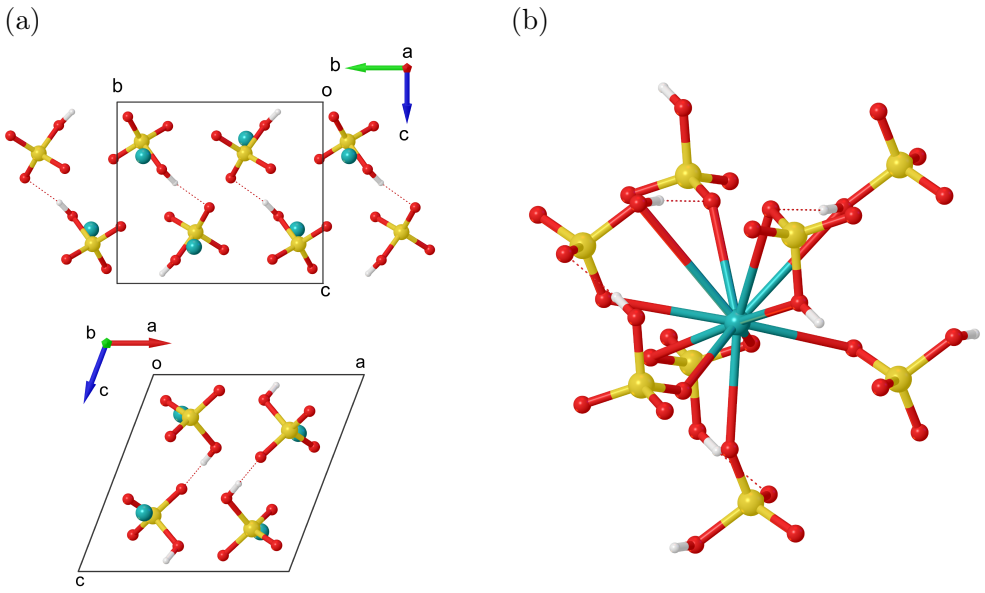

Figure 3.4.4: (a) Unit cell of $RbHSO_4$ phase III, two alternating HSO_4^- hydrogen-bonded chains form along the c axis; (b) Coordination environment of Rb in phase III.

110.938(7)°.

Change in $\langle I/\sigma(I)\rangle$ for reflections in the $0k0$ zone with pressure are shown in Figure 3.4.3(b), showing the clear presence of the 2_1 screw symmetry element in phases I and III. For phase II, refinement in $P2_1/n$ resulted in a significantly higher agreement factor, $R = 9.91$ % versus $R = 4.37$ % in Pn, confirming the systematic absence analysis.

In phase III, of the 279 reflections effected by the presence of c-glide symmetry, three have $I/\sigma(I) > 3$, $\langle I/\sigma(I)\rangle = 0.5$, $\langle I\rangle = 0.3$. The resulting structure for phase III is similar to that described by Asahi and Hasebe, although with space-group symmetry fully assigned. This structure is isostructural with the corrected structure of $CsHSO_4$-II reported by Chisholm and Haile (2000).

The diffraction pattern showed clear signs of pseudo-merohedral twinning, with two domains indexed to the above cell related by a two-fold rotation about the (101) direction, reflections are related by the twin law expressed in 3.4.1 as determined using the program *CELL NOW* (Sheldrick, 2005).

$$\begin{pmatrix} 0 & 0 & \bar{1} \\ 0 & \bar{1} & 0 \\ \bar{1} & 0 & 0 \end{pmatrix} \tag{3.4.1}$$

The twinning reflects the pseudo-orthorhombic symmetry of the lattice (present because $a \approx c$) leading to a two-domain twin. The refined twin scale factor was 0.541(11). Given the very minor structural differences between phases I and II, the following discussion of the structural changes is applicable to both I and II.

The rows of ions along the $[101]_{III}$ direction (equivalent to $[010]_I$) are preserved through the transition, with a shift in Rb^+ positions occurring within the ac_I-plane (equivalent to the [101]-$\mathbf{b}_{III}$-plane). The Rb^+ cations shift by $\pm 0.99(2)$ Å along the $[101]_I$ direction (along $\mathbf{b}_{III}$) in an alternating fashion (Figure 3.4.5). Accompanying this shift, the HSO_4^- anions reorient, breaking the infinite hydrogen-bonded chains along $\mathbf{b}_I$. The new arrangement consists of two symmetry-related, zig-zagging infinite chains along the $\mathbf{c}_{III}$ direction, with a O(H)...O distance of 2.576(15) Å. These new chains form at an angle of $\beta/2 = 55.5°$ to the direction of the chains in phase I. As a result, the asymmetric diamond-shaped channels in the $\mathbf{b}_I$ direction (along which the infinite $HSO_4^- \ldots HSO_4^-$ chains form) transform to staggered hexagonal channels to accommodate the HSO_4^- reorientations. The alternating chain direction regenerates the inversion symmetry of phase-I, removing the polarisation present in phase II.

Throughout this pressure range up to 1.1 GPa there are no statistically significant changes to bond lengths within the HSO_4^- anions. In phase III rubidium cations are coordinated by 11 oxygen atoms, an increase in coordination number of one as shown in Figure 3.4.4(b). Two HSO_4^- anions bind in a bidentate fashion through two oxygen atoms, the remaining anions bind in a monodentate manner. Rubidium-oxygen bonds adopt a wider range of lengths in this phase, from 2.861(9) to 3.589(12) Å, and as a result the average Rb−O bond length (3.121(9) Å) is the same within error as at ambient pressure (3.077(3) Å). This is an example of the widely-observed 'pressure-distance paradox' whereby pressure-driven coordination number increases are accompanied by an increase in bond lengths (Kleber and Wilke, 1969).

The pressure response of hydrogen bond O(H)...O distances is shown in Figure 3.4.6. Up to 0.4 GPa the hydrogen bonding distances in HS(1)O_4-I and HS(2)O_4-II chains remain distinct with the difference in O(H)...O distances increasing from 0.074(6) Å at ambient pressure to 0.13(2) Å at 0.4 GPa. Upon the transition to phase II, O(H)...O distances are not statistically distinguishable for each symmetry-independent

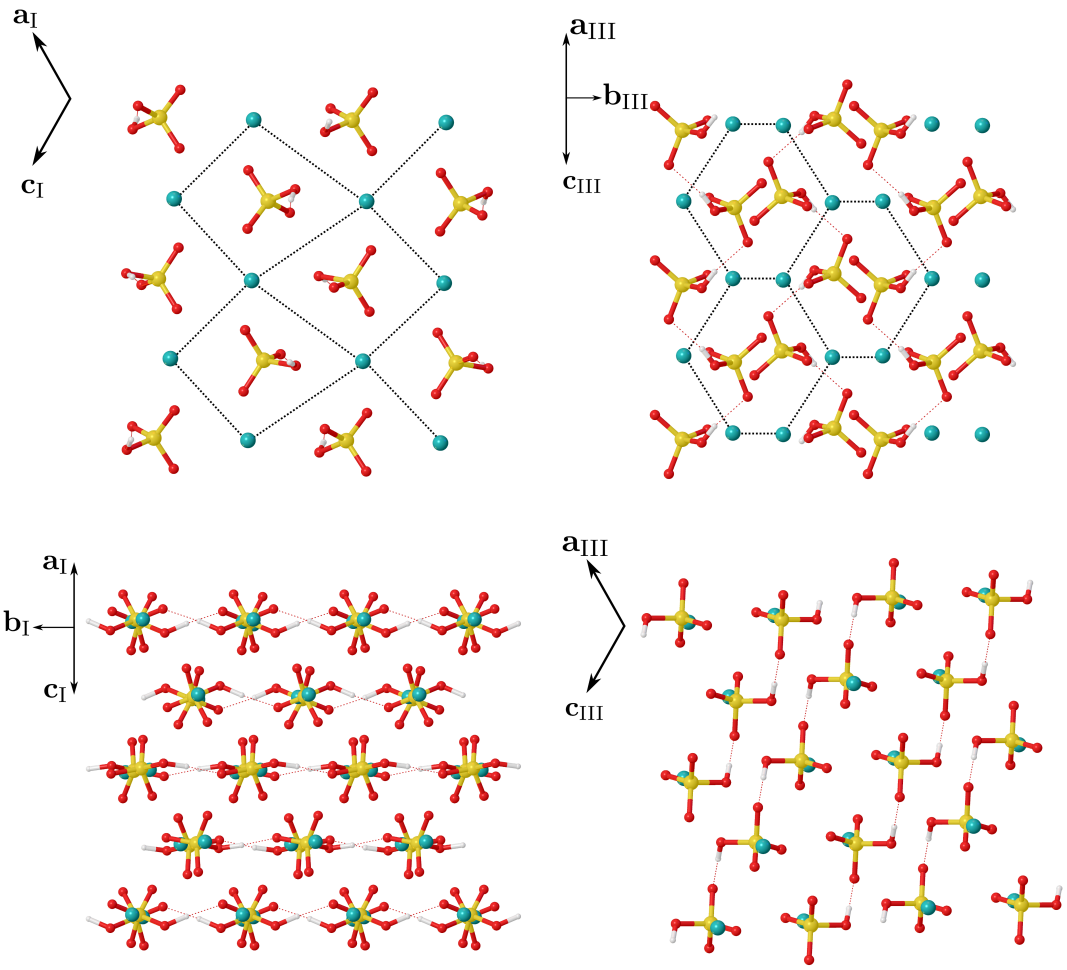

Figure 3.4.5: Reorientation of Rb^+ cations and HSO_4^- anions through the pressure-induced phase transition; (Top) Illustrates the asymmetric diamond channels in phase I, shifts in Rb^+ positions leading to the formation of staggered hexagonal channels containing reoriented HSO_4^- anions; (Bottom) Formation of a new hydrogen-bonding system in phase III. The linear chains along $\mathbf{b}_{\mathrm{I}}$ are broken by the movement of HSO_4^- anions to form new zig-zagging chains along the $\mathbf{c}_{\mathrm{III}}$ direction.

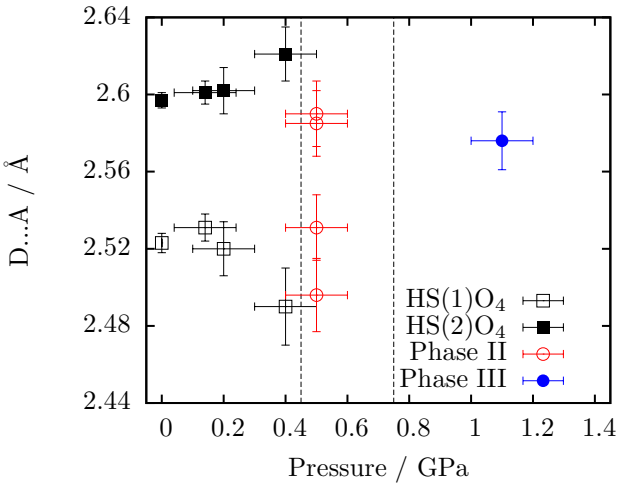

Figure 3.4.6: Changes in hydrogen-bonding with pressure in $RbHSO_4$. The two symmetry-independent hydrogen-bonded chains in phase I are shown in open and closed black squares. Phase II data are shown in open red circles. Phase III data shown in closed blue circles.

chain. The increase in symmetry over the phase II→III transition means that phase-III contains only one unique hydrogen bond, in which the O(H)...O distance is 2.576(15) Å, which is not significantly different to the ambient pressure values. Table 3.4.2 lists crystal structure determination details for each phase at high-pressure.

3.5 Conclusions

The paraelectric → ferroelectric transition in RHS has been investigated with neutron Laue diffraction. Hydrogen atoms were refined to singly-occupied positions with no sign of possible double-well occupancy. One HSO_4 moiety could be refined with two disordered oxygen atoms; this disordered model resulted in better agreement with the neutron data over an ordered model with distended oxygen ADPs. This disordered model for the paraelectric phase is in clear disagreement with Nalini and Row (2003), however literature dielectric and Raman spectroscopic results corroborate this conclusion. In contrast to other hydrogen-bonded ferroelectrics, the hydrogen atoms do not appear to play a critical role in the ferroelectric transition; the importance of oxygen atom disorder, illustrated by this finding, explains the notable lack of a strong isotopic effect reported in the literature.

An isothermal pressure series up to 1.1(1) GPa was carried out by single-crystal X-ray diffraction covering the two pressure-driven phase transitions observed to date. The first-order reconstructive phase transition from ferroelectric phase II to phase III was investigated, and the prior structural analysis had incorrectly described the symmetry of phase III as non-centrosymmetric $P2_1$ rather than centrosymmetric $P2_1/c$. This transition results in an increase in rubidium coordination number without a reduction in Rb−O bond lengths, a typical example of the pressure-distance paradox.

Table 3.4.2: Selected crystal data and details of the structure determination of $RbHSO_4$ phases I, II, and III by high-pressure X-ray diffraction

Crystal data					
Pressure (GPa)	0.15(10)	0.2(1)	0.4(1)	0.5(1)	1.05(10)
Phase	I	I	I	II	III
Formula	$HO_4S{\cdot}Rb$				
M_r	182.54				
Crystal system	Monoclinic				
Space group	$P2_1/n$ (No. 14)	$P2_1/n$ (No. 14)	$P2_1/n$ (No. 14)	Pn (No. 7)	$P2_1/c$ (No. 14)
a,b,c (Å)	14.324(3),	14.3405 (7),	14.334 (5),	14.166(5),	7.3202(7),
	4.6263(9),	4.6150 (2),	4.6197 (17),	4.5982(9),	7.765(2),
	14.401(7)	14.3723 (12)	14.361 (9)	14.326(4)	7.3247(8)
β (°)	117.74(3)	118.054 (4)	118.94 (3)	117.68(3)	110.938(7)
Volume (Å^3)	844.6(5)	839.42 (9)	832.2 (7)	826.4(5)	388.85(12)
Z	8	8	8	8	4
Radiation type	Mo $K\alpha$				
μ (mm^{-1})	12.088	12.16	12.27	12.355	13.129
Crystal size (mm)	0.10 x 0.12 x 0.20	0.10 x 0.15 x 0.20	0.10 x 0.15 x 0.20	0.10 x 0.12 x 0.20	0.10 x 0.12 x 0.20
Data collection					
Diffractometer	Bruker Kappa Apex2 diffractometer				
Absorption correction	Multi-scan SADABS (Sheldrick, 1996)				
T_{min}, T_{max}	0.26, 0.30	0.09, 0.30	0.08, 0.29	0.24, 0.29	0.17, 0.27
No. of measured, independent	3119, 754, 620	4260, 781, 673	4115, 754, 658	4613, 1240, 1149	1844, 295, 254
and observed $[I > 2.0\sigma(I)]$ reflections					
R_{int}	0.025	0.046	0.048	0.025	0.030
$(\sin\theta/\lambda)_{max}$ (Å^{-1})	0.617	0.595	0.588	0.620	0.602
Refinement					
$R[F^2 > 2\sigma(F^2)]$, $wR(F^2)$, S	0.023, 0.055, 1.02	0.056, 0.157, 0.99	0.069, 0.139, 1.04	0.044, 0.116, 0.83	0.032, 0.073, 0.98
No. of reflections	620	780	658	1149	254
No. of parameters	110	110	110	99	55
No. of restraints	0	20	28	2	13
H-atom treatment	H-atom parameters constrained				
$\Delta\rho_{min}$, $\Delta\rho_{max}$ (e Å^{-3})	0.35, -0.35	1.03, −0.73	1.27, −0.99	0.84, −1.01	0.50, −0.35
Absolute structure	-	-	-	Flack (1983), 562 Friedel-pairs	-
Absolute structure parameter	-	-	-	0.236 (18)	-

Computer programs: *Apex2* (Bruker, 2007), *SIR92* (Altomare *et al.*, 1993), *CRYSTALS* (Betteridge *et al.*, 2003), *CAMERON* (Watkin *et al.*, 1996).

3.6 References

Altomare A, Cascarano G, Giacovazzo C and Guagliardi A 1993 *Journal of Applied Crystallography* **26**(3), 343–350.

Asahi T and Hasebe K 1996 *Journal of the Physical Society of Japan* **65**(10), 3233–3236.

Ashmore J P and Petch H E 1975 *Canadian Journal of Physics* **53**(24), 2694–2702.

Betteridge P W, Carruthers J R, Cooper R I, Prout K and Watkin D J 2003 *Journal of Applied Crystallography* **36**(6), 1487.

Brach I, Jones D J and Rozière J 1983 *Journal of Solid State Chemistry* **48**(3), 401 – 406.

Bruker 2007 '*SAINT*'.

Campbell B J, Stokes H T, Tanner D E and Hatch D M 2006 *Journal of Applied Crystallography* **39**(4), 607–614.

Chisholm C R and Haile S M 2000 *Materials Research Bulletin* **35**(7), 999 – 1005.

Cruickshank D W J, Helliwell J R and Moffat K 1987 *Acta Crystallographica Section A* **43**(5), 656–674.

Cruickshank D W J, Helliwell J R and Moffat K 1991 *Acta Crystallographica Section A* **47**(4), 352–373.

Dawson A, Allan D R, Parsons S and Ruf M 2004 *Journal of Applied Crystallography* **37**(3), 410–416.

Flack H D 1983 *Acta Crystallographica Section A* **39**(6), 876–881.

Gesi K and Ozawa K 1975 *Journal of the Physical Society of Japan* **38**(2), 459–462.

Itoh K and Moriyoshi C 2003 *Ferroelectrics* **285**(1), 91–104.

Itoh K, Ohno H and Kuragaki S 1995 *Journal of the Physical Society of Japan* **64**(2), 479–484.

Kalevitch N, Arnscheidt B, Pelzl J and Rodin S 1995 *Journal of Molecular Structure* **348**, 361 – 364.

Kleber W and Wilke K T 1969 *Kristall und Technik* **4**(2), 165–199.

Lilienblum M, Hoffmann A, Soergel E, Becker P, Bohaty L and Fiebig M 2013 *Review of Scientific Instruments* **84**(4), 043703.

Merrill L and Bassett W A 1974 *Review of Scientific Instruments* **45**(2), 290–294.

Moggach S A, Allan D R, Parsons S and Warren J E 2008 *Journal of Applied Crystallography* **41**(2), 249–251.

Müller U 2013 *Symmetry relationships between crystal structures: applications of crystallographic group theory in crystal chemistry* Oxford University Press.

Nalini G and Row T G 2003 *Phase Transitions* **76**(11), 923–934.

Ozaki T 1980 *Journal of the Physical Society of Japan* **49**(1), 234–241.

Palatinus L and Chapuis G 2007 *Journal of Applied Crystallography* **40**(4), 786–790.

Parsons S 2004 '*SHADE*, program for empirical absorption corrections to high pressure data'.

Pepinsky R and Vedam K 1960 *Phys. Rev.* **117**, 1502–1503.

Piermarini G J, Block S, Barnett J D and Forman R A 1975 *Journal of Applied Physics* **46**(6), 2774–2780.

Piltz R O 2011 *Acta Crystallographica Section A* **A67**, C155.

Ponyatovskii E G, Rashchupkin V I, Sinitsyn V V, Baranov A I, Schuvalov L A and Shchagina N M 1985 *Jetp Letters* **41**(3), 139–141.

Prince E, Wilkinson C and McIntyre G J 1997 *Journal of Applied Crystallography* **30**(2), 133–137.

Sheldrick G M 1996 '*SADABS*, a program for empirical absorption correction of area detector data'.

Sheldrick G M 2005 '*CELL NOW*, program for unit cell determination'.

Sinitsyn V V 2010 *J. Mater. Chem.* **20**, 6226–6234.

Suzuki S, Osaka T and Makita Y 1979 *Journal of the Physical Society of Japan* **47**, 1741.

Toupry N, Poulet H and Le Postollec M 1981 *Journal of Raman Spectroscopy* **11**(2), 81–91.

Waskowska A, Olejnik S, Lukaszewicz K and Czapla Z 1980 *Crystal Structure Communications* **9**(3), 663–669.

Watkin D, Prout C and Pearce L 1996 '*CAMERON*, chemical crystallography laboratory'.

Wilkinson C, Khamis H W, Stansfield R F D and McIntyre G J 1988 *Journal of Applied Crystallography* **21**(5), 471–478.

Chapter 4

Mechanical Properties of a Cobalt Citrate Metal-Organic Framework Under Pressure

4.1 Synopsis

The mechanical behaviour of the metal-organic framework UTSA-16 was explored using three different hydrostatic media and was found to be highly dependent upon the compressing medium. The origin of these differences lies in coordination changes at the flexible cobalt tetrahedra. Under pure hydrostatic compression in FC70, these tetrahedra induce a negative linear compressibility effect *via* torsional flexing. In methanol, the filling of the pores and the shared coordination with ordered potassium cations suppresses this motion resulting in positive axial compressibilities. The pressure-driven transition observed in isopropyl alcohol results in the replacement of flexible cobalt tetrahedral with rigid octahedral units. The resulting reduced compressibility shows that these secondary-building units play a critical role in determining the mechanical strength of this framework material in both penetrating and non-penetrating hydrostatic media.

4.2 Introduction

Metal-organic framework (MOF) materials can display a wide-range of unusual physical properties which derive from both the chemical identities of the components as well as the topology of the framework. MOFs have been synthesised with a range of functional physical properties such as magnetism, nonlinear optics, negative thermal expansion, and negative linear compressibility (Kurmoo, 2009; Lock *et al.*, 2010; Yu *et al.*, 2012; Cairns *et al.*, 2013).

In general the mechanical response of a material to changes in temperature and pressure are described by thermal expansivities ($\alpha_V = (1/V)(\mathrm{d}V/\mathrm{d}T)$) or compressibilities ($\beta_V = -(1/V)(\mathrm{d}V/\mathrm{d}P)$). Thermal expansion coefficients are usually positive, corresponding to expansion on heating. Materials in which the volume decreases with heating exhibit negative thermal expansivity. The archetypal example is ZrW_2O_8, where the effect is the result of thermally-excited transverse vibrations (S. O. Evans, 1999; Mary *et al.*, 1996). While volume compressibility is thermodynamically required to be positive, the same restriction does not apply to linear compressibilities (Gatt and Grima, 2008). In a few materials, one or two dimensions increase under pressure, behaviour termed *negative linear compressibility* (NLC). It has been proposed that materials ex-

hibiting NLC might find use in high-performance pressure sensors or in more exotic applications such as body armour (Gagnon *et al.*, 2013).

Flexibility, both in the mechanical sense and in the ability to allow a range of small-molecule guests to diffuse into the pores, is one of the attractive properties of MOFs as functional materials; the properties of the crystalline material may be changed after synthesis by the inclusion, expulsion, or reaction of guest molecules, in addition to changes in temperature, pressure, or incident electromagnetic radiation.

Depending upon the host and guest, the framework may act as catalyst or container for a reaction within the material (Wang *et al.*, 2013) or allow selective guest adsorption (McKellar *et al.*, 2014), sensing (Kreno *et al.*, 2012), or separation (Li, Sculley and Zhou, 2012). Alternatively, the interest may be in the behaviour of the framework itself. Guest molecules can be used to perturb the structure, altering some intrinsic physical property; guests can be removed or substituted by heat, pressure, or immersion in some other liquid or gas. The often highly specific interactions of guest molecules and labile metal centres have been exploited to produce frameworks with guest-dependent functional responses such as changes in magnetic susceptibility (Maspoch *et al.*, 2003), metal spin state (Halder *et al.*, 2002; Duriska *et al.*, 2009), or luminescence (Allendorf *et al.*, 2009).

The application of pressure is a powerful technique for investigating the mechanical and physical properties of porous framework materials and in particular host-guest interactions (Tan and Cheetham, 2011; Li *et al.*, 2014). In a high-pressure experiment the sample is surrounded by some hydrostatic medium which applies pressure to the sample. A judicious choice of hydrostatic medium can allow new host-guest interactions to form by the diffusion of penetrating molecules into the pores. This can lead to functional host-guest systems or to structural transitions *increasing* pore size with pressure (Fairen-Jimenez *et al.*, 2011; Graham *et al.*, 2011; Moggach *et al.*, 2009). Alternatively, perturbing the system by applying greater pressure can alter the intrinsic properties of the system with the ultimate aim of providing novel functional materials (Chapman *et al.*, 2008).

The porous material originally formulated $([KCo_3(cit)(Hcit)(H_2O)_2]\cdot 8H_2O)_n$, (cit = $C_6H_4O_7^{4-}$) known as UTSA-16, (UTSA = University of Texas at San Antonio) attrac-

ted attention due to the notably high carbon dioxide adsorption, despite being relatively dense, indicating strong framework-pore interactions (Xiang *et al.*, 2005, 2012). However, understanding the native mechanical properties of a framework without the complication of host-guest interactions requires a non-penetrating hydrostatic medium. Due to the large size of the perfluorohydrocarbon molecules that make up FC70, this pressure-transmitting medium does not penetrate the pores of UTSA-16, resulting in pure hydrostatic compression. Our aim here has been to investigate how UTSA-16 responds to the application of hydrostatic pressure by both penetrating (methanol and isopropyl alcohol) and non-penetrating hydrostatic media (Fluorinert FC70).

4.3 Methods

Crystals of UTSA-16 were prepared by hydrothermal reaction according to the literature preparation (Xiang *et al.*, 2005) by the Murrie Group at the University of Glasgow. A solution of $Co(OAc)_2{\cdot}4H_2O$ (0.249 g, 1 mmol, Ac = acetate), citric acid monohydrate (0.21 g, 1 mmol), and potassium hydroxide (0.168 g, 3 mmol), in a 1:1 mixture of H_2O and EtOH (9 ml) was heated under solvothermal conditions in a Teflon-lined Parr acid-digestion bomb at 393 K for 48 hours, then cooled to ambient temperature at a rate of 4 K hr^{-1}. A violet crystalline solid was obtained. This was filtered, washed with Et_2O, and air-dried giving a yield of 20 %.

The chemical composition of both single-crystal and powder samples of UTSA-16 were investigated using energy-dispersive X-ray spectroscopy (EDS) of samples placed in a scanning electron microscope (SEM). A mixture of powder and single crystals were mounted in epoxy resin and polished to a 1 μm diamond finish. A layer of carbon, approximately 50 Å thick, was evaporated onto the surface under vacuum to prevent charging. The SEM was a Zeiss Ultra Plus with an attached Oxford Instruments X-max 80 mm^2 Silicon Drift Detector X-ray microanalysis system operated at an accelerating voltage of 15 kV. A total of six measurements were made, three on powder samples and three on single-crystals identified at the surface of the resin.

Single-crystal diffraction data were collected on a Bruker SMART APEX II diffractometer with graphite-monochromated Mo Kα radiation ($\lambda = 0.71073$ Å). Data were

integrated using *SAINT*, absorption corrections were carried out in *SADABS* (Bruker, 2007; Sheldrick, 1996). Unless otherwise stated below, all structures were solved with *Sir92*; refinement was carried in *CRYSTALS* (Altomare *et al.*, 1993; Betteridge *et al.*, 2003).

Ambient pressure diffraction data were also collected on a single-crystal sample submerged in methanol using the capillary technique presented by McKellar *et al.* (2014). The crystal was mounted inside a MiTeGen MicroRT^{TM} capillary attached to a goniometer head, sealed and filled with methanol. Scattering from the surrounding methanol produces significant background in the diffraction frames; however the structure could be solved and refined without difficulty.

High-pressure single-crystal diffraction experiments were carried out using a Merrill-Bassett diamond anvil cell (DAC) (Merrill and Bassett, 1974) with a tungsten carbide backing disk and tungsten gasket (Moggach *et al.*, 2008). The sample and a chip of ruby were loaded with Fluorinert FC70, methanol (MeOH), and isopropyl alcohol (IPA) as hydrostatic media. Ruby fluorescence was used to measure the pressure (Piermarini *et al.*, 1975). High-pressure data were integrated in *SAINT* using dynamic masks to mask regions of the frames shaded by the cell body (Dawson *et al.*, 2004). The program *SHADE* was used to omit partially shaded and diamond reflections (Parsons, 2004), absorption corrections were applied using *SADABS* (Sheldrick, 1996).

High-pressure data were collected on UTSA-16 in MeOH (referred to as UTSA-16_{MeOH}) from 0.35 to 5.85 GPa in increments of approximately 2 GPa, in FC70 (UTSA-16_{FC70}) from 0.3 to 1.7 GPa in increments of approximately 0.5 GPa, and in IPA (similarly, UTSA-16_{IPA}) from 0.5 to 3.3 GPa in approximately 1 GPa increments. On increasing pressure above 0.5 GPa, UTSA-16_{IPA} underwent a single-crystal to single-crystal phase transition (hereafter referred to as UTSA-16_{IPA}-I to UTSA-16_{IPA}-II), lowering the space group symmetry from $I\bar{4}2d$ to $P2_12_12_1$.

4.3.1 Refinement of high-pressure data

Single-crystal diffraction data collected at high-pressure suffers from low completeness as a result of shading of reciprocal space by the pressure cell, approximately 70 % for most data sets, as well as other systematic errors as a result of the cell (Dawson *et al.*,

2004). As a result rigid-bond, rigid-body restraints in addition to bond-angle and bond-length restraints were applied to the citrate anions; these maintained the C−O bond lengths and angles within the carboxylate and alkoxide groups, and were derived from the ambient pressure structure collected at 300 K. With the exception of UTSA-16$_{\mathrm{IPA}}$-II and the highest pressure structure of UTSA-16$_{\mathrm{MeOH}}$-I, C−C bonds and angles were refined freely. All metal-oxygen distances and angles were refined freely.

The pressure-induced phase transition induces a lowering of symmetry from a tetragonal body-centred to a primitive orthorhombic lattice causing the crystal to become twinned. Coset decomposition of point group $4/mmm$ with respect to point group 222 gives a total of four possible domains which in this case were related by inversion, a four-fold rotation about **c**, expressed by the twin law Eq. 4.3.1, as well as its inverse Eq. 4.3.2. Twin scale factors for all four domains could not be refined, using a two-domain model with the four-fold rotation about **c** resulted in refined twin scale factors of 0.657(6) at 1.5 GPa and 0.671(6) at 2.4 GPa.

$$\begin{pmatrix} 0 & 1 & 0 \\ \bar{1} & 0 & 0 \\ 0 & 0 & 1 \end{pmatrix} \tag{4.3.1}$$

$$\begin{pmatrix} 0 & \bar{1} & 0 \\ 1 & 0 & 0 \\ 0 & 0 & \bar{1} \end{pmatrix} \tag{4.3.2}$$

The structure was solved in space group $P2_12_12_1$ with dimensions (for UTSA-16$_{\mathrm{IPA}}$-II at 1.5 GPa) $a = 13.059(3)$, $b = 13.0708(13)$, and $c = 30.010(4)$ Å. Checks for absent symmetry were carried out using the *ADDSYM* routine implemented in *PLATON* Spek (2009). An initial model for refinement was generated using the UTSA-16$_{\mathrm{IPA}}$-I structure transformed to a primitive cell. Additional potassium ion and solvent oxygen sites were located in Fourier difference maps.

4.4 Results and Discussion

4.4.1 Structure and composition of UTSA-16 at ambient temperature and pressure

The interactions of the pressure medium and sample crystal are normally limited to considerations of the sample solubility and the hydrostatic limit of the medium. However for metal-organic frameworks, the penetration of the medium into the MOF can induce structural changes even at ambient pressure (McKellar *et al.*, 2014). It was therefore necessary to collect two ambient-pressure structures, one with the crystal immersed in the medium and another standard collection in dry air.

Ambient pressure data collections were carried out at 300 K to provide a reference structure for high-pressure analysis and at 100 K to identify the pore content. At room temperature and ambient pressure the structure is tetragonal, space group $I\bar{4}2d$, a = 12.9994(1), and c = 30.2138(4) Å.

There are two crystallographically independent Co^{2+} centres and one unique citrate anion in the asymmetric unit. Co1 and the alkoxy oxygen atom (O3) from the citrate form S_4-symmetric Co_4O_4 cubanes. Carboxylate oxygen atoms O1, O4, and O6 from each citrate bind to the three Co atoms connected to O3, making each Co1 six coordinate (Figure 4.4.1(a)). Co2 is located on a two-fold axis and is pseudo-tetrahedrally coordinated to one pair of equivalent carboxylate atoms (O2) from the same cubane, and another pair (O7) derived from different cubanes. The cubanes are also connected through potassium cations (K1) which reside on two-fold axes and bind to the same carboxylate oxygen atoms (O1, O4, and O6) coordinated to Co1. The eight-fold coordination sphere of K1 is completed by two equivalent water molecules (O8).

Each cubane binds to six Co2-tetrahedra (two through pairs of O2 and four through O7), while each Co2-tetrahedron binds to three cubanes. Overall the topology of the structure is analogous to anatase, a form of TiO_2, where the cubanes correspond to titanium and the tetrahedra correspond to oxides. The space group of UTSA-16 ($I\bar{4}2d$) is related to that of anatase ($I4_1/amd$) by the loss of inversion symmetry as the result of the replacement of titanium and oxygen atoms with lower symmetry octahedra and tetrahedra. These nodes link to form orthogonal sheets of rhomboid rings intersecting at each octahedral node (*cf.* Figure 4.4.1(b) and (c)). The Co2 tetrahedra act as trigonal

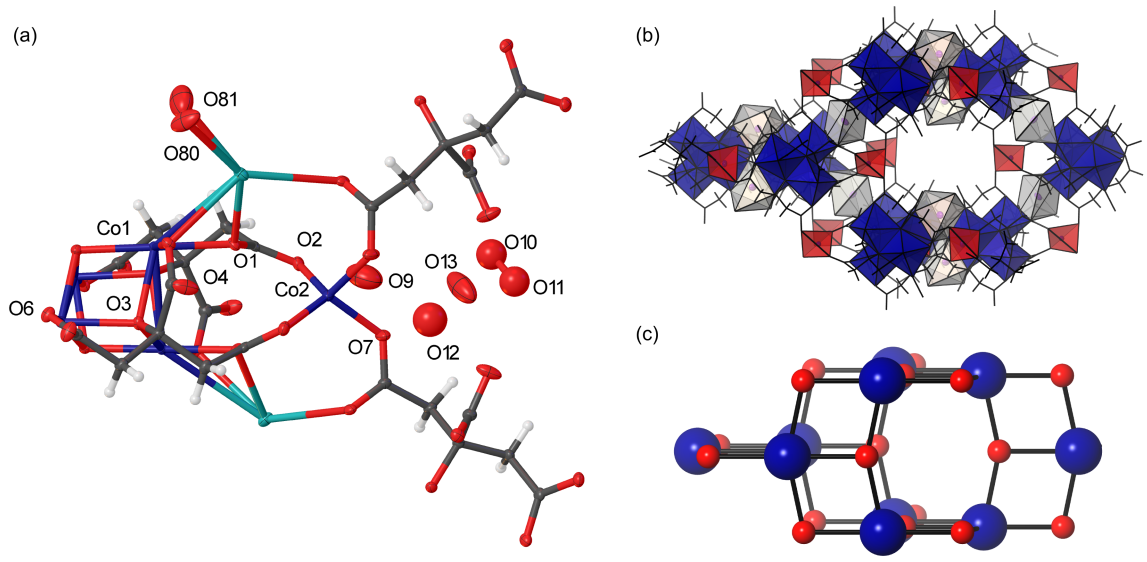

Figure 4.4.1: (a) Selected structural units in UTSA-16 at 100 K. Only two of the cubane-encapsulating citrate anions are shown for clarity; (b) Polyhedral representations of UTSA-16, cobalt octahedra are shown in dark blue, cobalt tetrahedra are shown in red, irregular potassium polyhedra are shown in white; (c) Structure of anatase, $I4_1/amd$, (Ti - blue, O - red) whose topology is analogous to UTSA-16.

nodes, and the Co_4O_4-citrate clusters act as octahedral nodes between Co2 tetrahedra while also coordinating *via* K^+ linkers in a tetrahedral fashion producing a series of channels approximately 13 × 10 Å.

At 100 K, the pore contents were refined to a model consisting of 3.6 water molecules, two of which occupy fully ordered sites (O9 and O13), with the remaining site split across three positions. The occupancies of the first two, O10 and O11, were constrained to one due to their close proximity resulting in occupancies of 0.54 and 0.46, respectively. Occupancy of the final position, O12, was freely refined to 0.6 (Figure 4.4.1(a)). The positions and refined occupancies are essentially the same as reported by Xiang *et al.* (2005). Sites O9-O12 form chains linked by hydrogen bonding and tethered to the citrate O5 atoms (O5...O11 = 2.73(2) Å). In addition, the potassium-coordinated O8 water ligand site is split into disordered sites O80/O81, binding to K1 at a distance of 2.806(9)/2.816(14) Å. Each K1 is coordinated by six citrate oxygen atoms and two symmetry related O80/81 sites to give a full 8-coordinate shell.

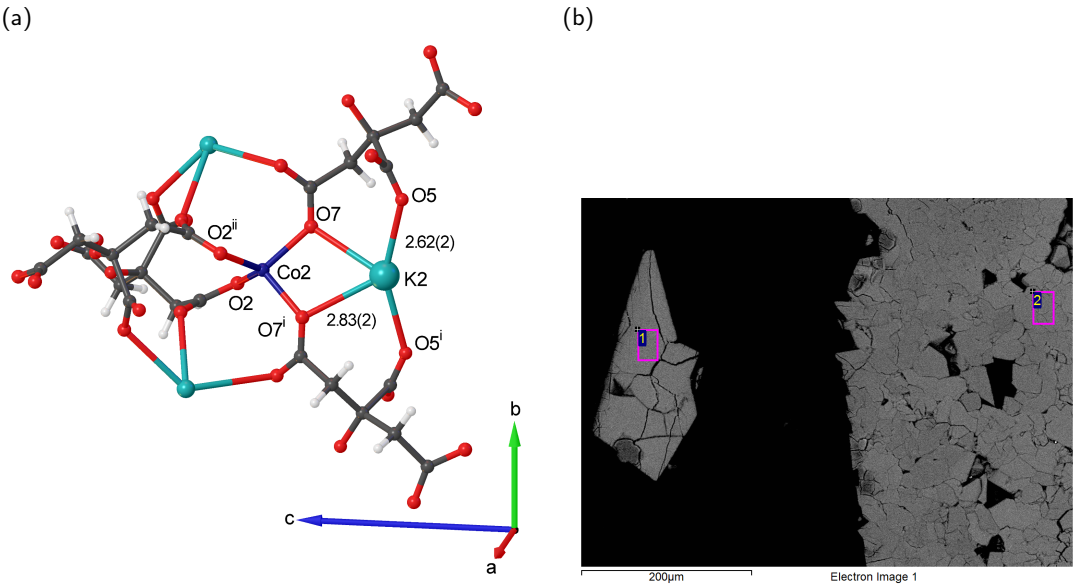

Figure 4.4.2: (a) Selected part of the UTSA-16$_{\mathrm{MeOH}}$ structure at ambient pressure submerged in MeOH illustrating the location of the 'channel' coordination site K2; (b) An SEM image at 200x magnification of UTSA-16 single-crystals (1) and powder (2) embedded in resin for EDS analysis. The rectangles mark the areas sampled. $^{i} = [-x, -y, z]$, $^{ii} = [1 - y, 1/2 - x, z + 1/4]$.

4.4.1.1 Structure and composition of UTSA-16-I submerged in methanol at ambient pressure

Single-crystal X-ray diffraction data were collected on a sample crystal of UTSA-16 immersed in methanol inside a MiTeGen MicroRT$^{\mathrm{TM}}$ capillary. Even in the absence of applied pressure, methanol enters the UTSA-16 structure causing a significant change in unit-cell dimensions. The a-axis increases from 13.069(4) to 13.36(3) Å, (+0.23(3) Å, +2 %), while the c-axis decreases from 30.157(1) to 30.05(1) Å (−0.11(1) Å, −0.4 %), giving a total volume increase of 218.73 Å^3 (+4.2 %).

Solution of the structure showed an unexpected additional electron density maximum of 5.4 e Å^{-3} within the pore on special position (1/2, 0, z), Wyckoff site c with point symmetry 2. The peak had four nearest neighbours; two otherwise unbound carboxylate oxygen atoms (O5 and O5$^i[-x, -y, z]$ at distances of 2.62(2) Å) and two O7 atoms (O7 and O7^i) at 2.83(2) Å. The combination of negatively charged nearest neighbours and similar interatomic distances to K1 suggests this additional peak to be a potassium cation. This coordination site, K2, will be referred to as the 'channel' site to distinguish from the K1 'linker' site and is shown in Figure 4.4.2(a).

K2 displays an equivalent isotropic displacement parameter of U_{eq} = 0.082 Å^2 ap-

proximately double that of K1 (U_{eq} = 0.045 Å^2) indicating the coordination site is poorly defined. The methanol-induced ordering of K2 causes very little change to the rest of the framework structure. The occupancy of K2 was refined giving a value of 0.85(5), corroborating with the composition determined by EDS (see §4.4.1.2 below).

There are only minor changes to the Co2 coordination environment despite sharing the O2 binding site with the newly ordered K2: the Co−O bond lengths remain unchanged however the torsion angle, ϕ (defined between planes O2−Co2−O2^{ii} and O7−Co2−O7^{i}), of the Co2 tetrahedra increases by 5.7° from 81.63(16)° to 87.3(9)°: K2 coordination twists the Co2 tetrahedron away from the ideal tetrahedral geometry.

This methanol-induced K2 'channel' coordination is fully reversible; when the sample is allowed to dry at ambient conditions the refined structure again matches the room-temperature structure shown above, with no sign of K2 and with unit-cell dimensions returning to within 0.1 Å of the original values.

4.4.1.2 The composition of UTSA-16 determined by EDS

UTSA-16 was originally formulated by Xiang *et al.* as $([KCo_3(cit)(Hcit)(H_2O)_2]\cdot 8H_2O)_n$. X-ray photoelectron spectroscopy (XPS) data and bond valence analysis both imply that cobalt is exclusively in the +2 oxidation state, and charge balance was attained by assuming that the citrate ligands exist in an mixture of half tri- and half tetra-deprotonated forms (Xiang *et al.*, 2012).

Our samples of UTSA-16 were prepared in the same manner as in (Xiang *et al.*, 2005) and consisted of clusters of well-formed single-crystals alongside a fine-grained powder (as shown in Figure 4.4.2(b)), EDS analysis showed no difference between powder and single-crystal regions and the average atomic percentages of K^+ and Co^{2+} were 10.8(5) % and 18.8(4) % respectively, implying a K:Co ratio of approximately 0.58, which deviates from the value of 0.33 expected on the basis of the original formulation. From the samples tested by EDS, one single-crystal contained a 2 % contribution from Na^+, but no other additional elements were identified. On the basis of the EDS analysis, the composition of UTSA-16 seems best described as $([K_{1+x}Co_3(C_6H_4O_7)(C_6H_{5-x}O_7)(H_2O)_2]\cdot mH_2O)_n$ with $x \approx 0.8$, which is consistent with the crystallographic analysis described above. Thermogravimetric analysis data presented by Xiang *et al.* (2005) show a weight

loss step at 412 K of 18.7 %, corresponding to removal of the eight water molecules per formula unit from the pore. Inclusion of the extra 0.8 moles of potassium in the interpretation of the TGA results increases the pore occupancy (m) slightly to 8.3 molecules, that is $([K_{1.8}Co_3(C_6H_4O_7)(C_6H_{4.2}O_7)(H_2O)_2]\cdot 8.3H_2O)_n$.

Elemental analysis is reported for carbon and hydrogen in the supplementary information provided by Xiang *et al.*, and was calculated for the composition $([KCo_3(C_6H_4O_7)(C_6H_5O_7)(H_2O)_2]\cdot 8H_2O)_n$ which gives C, 18.63 %; H, 3.78 %. The reported results are C, 18.59 %; H, 3.83 % taken to be in agreement with the calculated values (Xiang *et al.*, 2005). Calculated values for our formula are C, 17.81 %; H, 3.59 %. This suggests that the potassium/protonation ratio could vary significantly given the close match for composition presented by Xiang *et al.*

4.4.2 Mechanical properties in different hydrostatic media

The response of the UTSA-16 framework to hydrostatic pressure depends markedly on the hydrostatic medium. Figure 4.4.3 shows the normalised changes in unit-cell dimensions with pressure for FC70, MeOH, and IPA. There is a striking qualitative difference between the response to penetrating (IPA, MeOH) and non-penetrating (FC70) hydrostatic media. All pressure-volume data were fitted using second-order Birch-Murnaghan equations of state (Birch, 1986) in *EoSFit 7* (Angel *et al.*, 2014) to give bulk and axial compressibilities in the pressure ranges described below as shown in Table 4.4.1.

In FC70, up to 1.0 GPa, the unit-cell volume decreases by 335.6(5) Å^3 (6.5 %) corresponding to a bulk modulus of 13.3(15) GPa ($\beta_V = 75(9)$ TPa^{-1}), which is similar to other framework materials (Cairns *et al.*, 2013; Gagnon *et al.*, 2013). Beyond 1.0 GPa the material irreversibly loses crystallinity. This limit may be due to the onset of non-hydrostaticity in FC70 at this pressure, or could be an intrinsic property of the framework. The reduction in volume is due to compression along the a and b-axes, which shorten by 0.4612(5) Å (−3.5 %, $\beta_a = 43(6)$ TPa^{-1}). The c-axis displays negative linear compressibility, increasing in length by 0.1356(11) Å, a change of +0.45 % ($\beta_c = -5.1(8)$ TPa^{-1}).

When compressed with MeOH, the a-axis initially increases (relative to the values determined from the submerged, ambient-pressure structure) before decreasing with

further applied pressure. This behaviour has been observed in other MOFs and is due to solvent being forced into the pores and has been associated with increased pore electron density as measured using the *SQUEEZE* algorithm (Fairen-Jimenez *et al.*, 2011; Spek, 2015). Fitting pressure-volume data in the range 0.35 to 5.85 GPa (*i.e.* after the pore is saturated with methanol) yields a bulk modulus of 36(4) GPa at 0.5 GPa ($\beta_V = 28(3)$ TPa^{-1}) with all axes showing positive linear compressibilities; $\beta_a = 11(4)$ TPa^{-1}, and $\beta_c = 8(2)$ TPa^{-1}.

The most notable feature of the behaviour of UTSA-16 when compressed with IPA is the tetragonal-to-orthorhombic phase transition occurring between 0.5 and 1.5 GPa. The bulk modulus of the orthorhombic phase (referred to as UTSA-16_{IPA}-II) is 51(5) GPa at 0.5 GPa ($\beta_V = 19(2)$ TPa^{-1}), significantly higher than that of UTSA-16_{MeOH}-I (isostructural to UTSA-16_{IPA}-I) at the same pressure. All axes show significantly lower compressibilities in UTSA-16_{IPA}-II, although the effect is most pronounced along **c**: $\beta_a = 8.0(9)$ TPa^{-1}, $\beta_b = 9.0(9)$ TPa^{-1}, and $\beta_c = 3.4(17)$ TPa^{-1}.

FC70	Compressibility / TPa^{-1}
β_a	43(6)
β_c	−5.1(8)
β_V	75(9)
Methanol	At 0.5 GPa
β_a	11(4)
β_c	8(2)
β_V	28(3)
Isopropyl alcohol	At 0.5 GPa
β_a	8.0(9)
β_b	9.0(9)
β_c	3.4(17)
β_V	19(2)

Table 4.4.1: Bulk and axial compressibilities of UTSA-16 with three hydrostatic media.

4.4.3 The effect of pressure on UTSA-16 in FC70

On increasing pressure, no statistically significant changes in either bond distances or angles were observed within the cubane units and associated citrate anions. Tethering the linking carboxylate group to the cubane unit prevents any significant torsion in

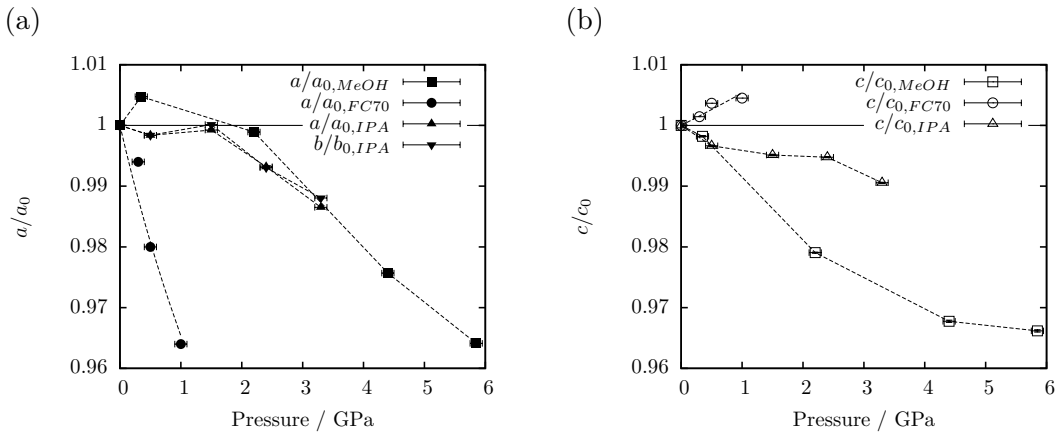

Figure 4.4.3: Normalised changes in unit-cell dimensions ((a) *a* and *b*-axes; (b) *c*-axis) of UTSA-16 in three hydrostatic media. Data from FC70 are illustrated by circles, MeOH by squares, and IPA by triangles.

these groups over the pressure range. By contrast, significant changes can be seen in tetrahedra based on Co2 (Figure 4.4.4). Up to 1.0 GPa, the volume of the Co2 tetrahedron, decreases by 0.186 Å^3 (−4.7 %) accompanied by a twisting motion between the planes O2-Co-O2^{ii} and O7-Co-O7^{i} reducing the dihedral angle ϕ from 98.34(16)° to 73.6(6)° (Figure 4.4.4(b)). The twisting of one Co2-tetrahedron allows the cubane-cubane distance to decrease across the pore. The contraction is replicated in an orthogonal direction by tetrahedra related by the two-fold rotation axes along the *a*- and *b*-axes, this concerted motion of the Co2 tetrahedra allows the framework to compress under pressure perpendicular to the *c*-axis (Figure 4.4.4(a)).

As a result of the reducing volume, and to avoid compression of the Co−O bond distances, the tetrahedra elongate along the *c*-axis direction giving rise to the negative linear compressibility. Thus the NLC arises as a result of a compensating change in the 'softer' torsion angle rather than the 'harder' bond distances.

Unlike other NLC-MOFs, in UTSA-16 the role of the rigid structural unit is not played by a simple organic linker as in zinc formate or silver(I) 2-methylimidazolate, but by the entire citrate-encapsulated cubane secondary building unit (Ogborn *et al.*, 2012). Changes in the length (l) of the tetrahedron parallel to the *c*-axis, and ϕ are shown in Figure 4.4.4(b).

The relative flexibility of the Co2 tetrahedra versus the Co1 octahedra arises from both the effect of ligand-sharing within the citrate-encapsulated cubanes as well as the

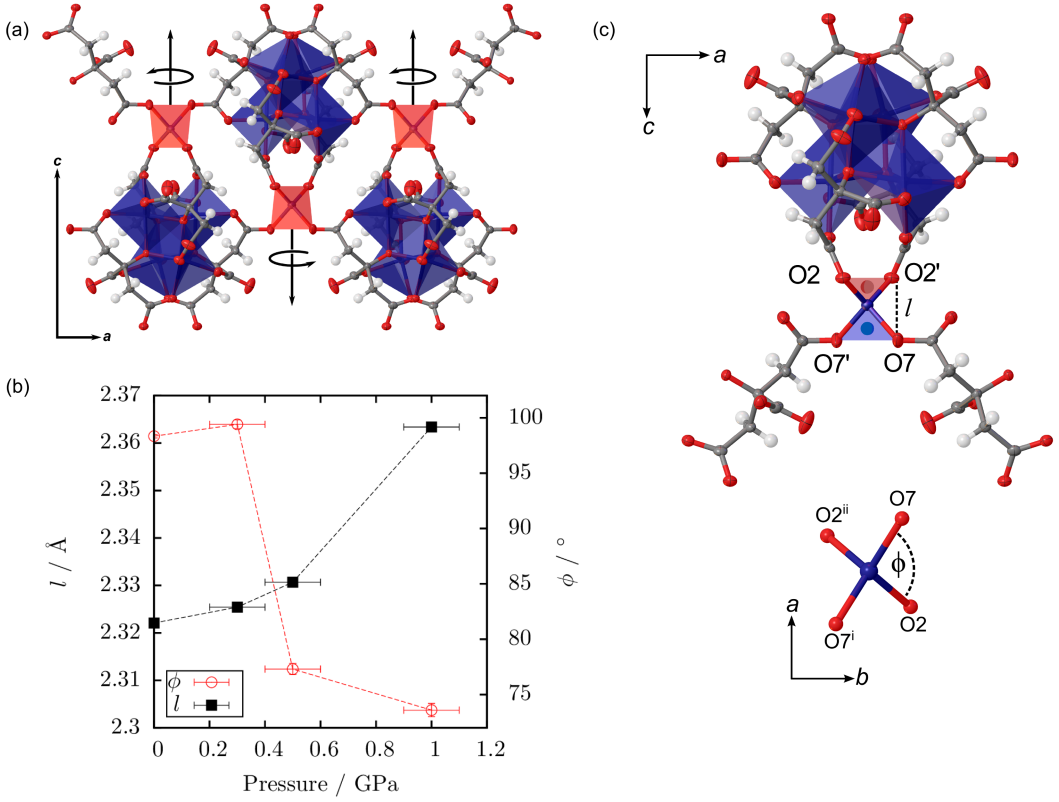

Figure 4.4.4: (a) NLC arises along the *c*-axis by the elongation of the Co tetrahedra. This elongation is a result of the twisting of the O−Co−O planes. In order to maintain rigid Co−O bond lengths the tetrahedron length, l, must increase; b) The planes O2−Co−O2' and O7−Co−O7' are shown in red and blue respectively, tetrahedron length parallel to **c** is labelled l; c) Decrease in dihedral angle ϕ and consequential increase in tetrahedron length l with increasing pressure. $^{i} = [1-x, 1-y, z]$ $^{ii} = [1-y, 1/2-x, z+1/4]$.

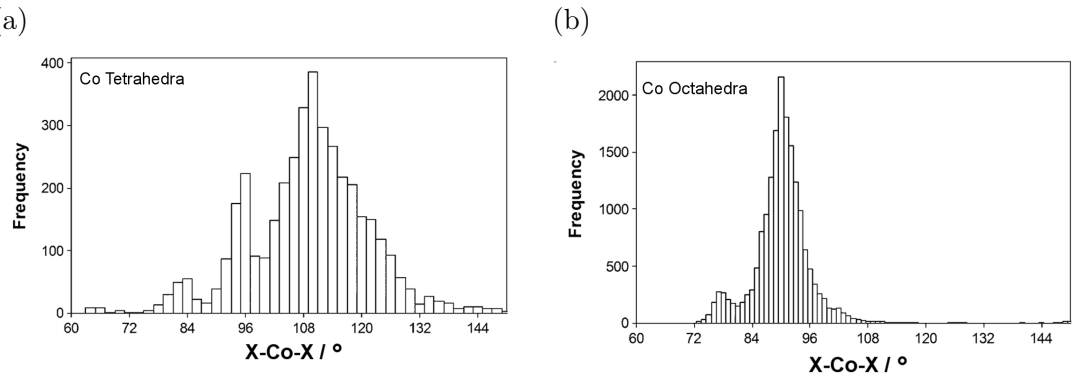

Figure 4.4.5: Distributions of X-Co-X bond angles for X = N and O for (a) tetrahedral and (b) octahedral complexes deposited in the Cambridge Structural Database.

inherently greater flexibility in tetrahedral coordination spheres as a result of lower steric hindrance and a smaller crystal field splitting. This flexibility can be observed in the far wider distribution of O/N−Co−O/N angles adopted within tetrahedral complexes compared to octahedral complexes for structures reported in the Cambridge Structural Database (Figure 4.4.5) (Allen, 2002)

4.4.4 The effect of pressure on UTSA-16 in MeOH

To understand the effect of K2 coordination on the mechanical properties of UTSA-16, high-pressure single-crystal diffraction data were collected at 0.35(10), 2.2(1), 4.4(1), and 5.9(1) GPa. Structures could be successfully refined to a pressure of 4.4 GPa, and up to this pressure the structure of UTSA-16_{MeOH} undergoes little change from the methanol-submerged structure (§4.4.1.1, Figure 4.4.2). As is the case under pure hydrostatic compression (*c.f.* §4.4.3), the most significant structural changes occur within the Co2 tetrahedra. Dihedral angle ϕ increases 7.9(15)° from 84.4(10)° to 92.3(12)° at 4.4 GPa, the reverse of the behaviour under pure compression, restoring normal positive linear compressibility. Associated with this torsion, the bond angle O2−Co2−$O2^{ii}$, which links citrate molecules bound to the same cubane, increases by 17(2)° from 117.5(12)° at ambient pressure to 134(2)° at 4.4 GPa. By contrast the bond angle O7−Co2−$O7^{i}$, which links citrate molecules across the pore and which shares coordination with K2, shows no significant change over the same pressure range (Figure 4.4.6).

It appears that the presence of K2 in the pore 'reinforces' the ∠O7 − Co2 − O7 and prevents the decrease in ϕ observed with FC70. As a result, the combination

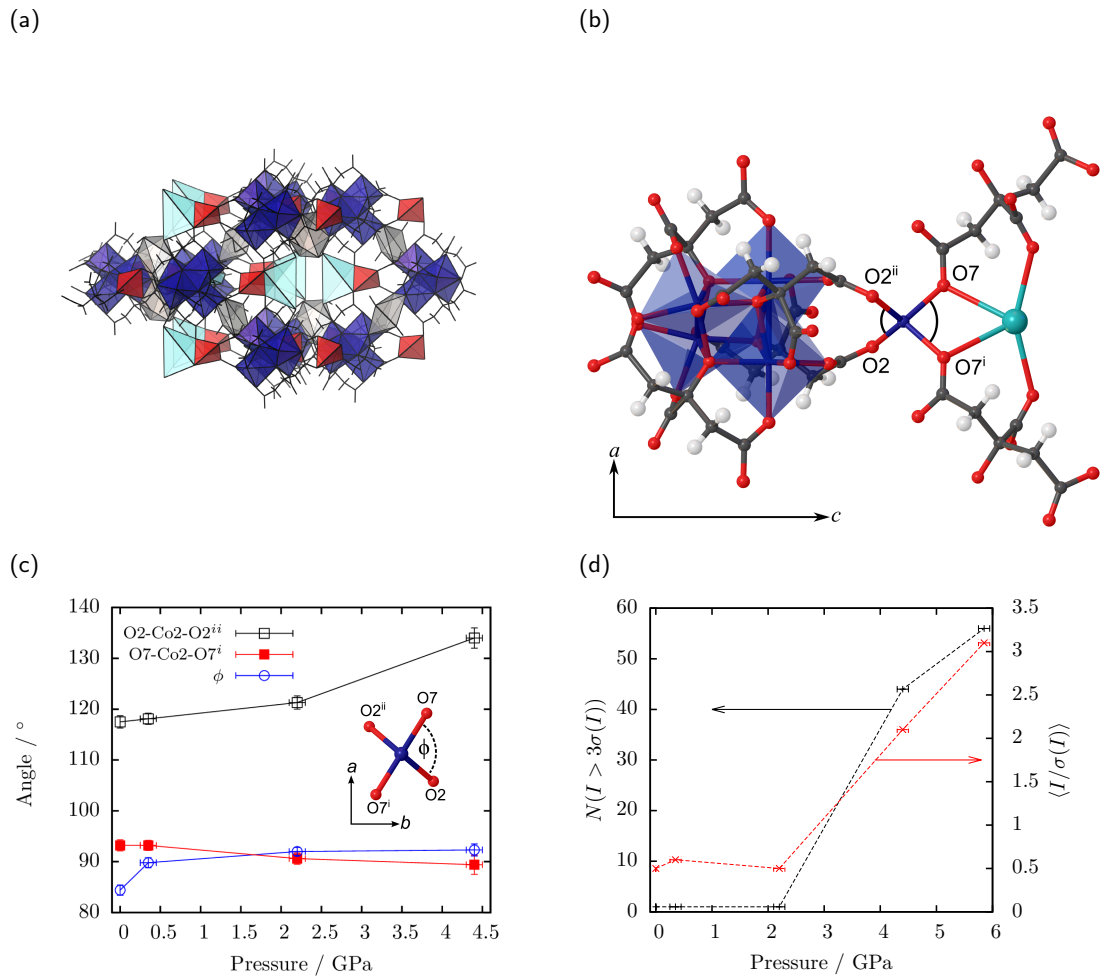

Figure 4.4.6: (a) UTSA-16$_{\mathrm{MeOH}}$ illustrating the location of the 'channel' coordination site shown as a light blue polyhedron; (b) Selected structural unit in UTSA-16, the angles discussed in the text are marked; (c) Pressure response of Co2 tetrahedral angles to hydrostatic pressure in the presence of methanol. $^{i} = [1-x, 1-y, z]$, $^{ii} = [1-y, 1/2-x, z+1/4]$; (d) Changes in the number and average $I/\sigma(I)$ of reflections violating d-glide symmetry with pressure.

of pore-filling and K^+ coordination markedly changes the mechanical properties of this framework; bulk compressibility decreases more than two-fold ($\beta_{V,\mathrm{MeOH}} = 29(3)$ TPa^{-1} *vs.* $\beta_{V,\mathrm{FC70}} = 75(9)$ TPa^{-1}) and the negative compressibility effect is supressed ($\beta_{c,\mathrm{MeOH}} = 8(2)$ TPa^{-1} *vs.* $\beta_{c,\mathrm{FC70}} = -5.1(8)$ TPa^{-1} in FC70).

While a structure could be sensibly refined in space group $I\bar{4}2d$ at 4.4(1) GPa, it was noticeable that additional intensity appeared for systematically-absent reflections (Figure 4.4.6(d)). These peaks were very weak and showed distinct smearing in the hk-plane. By 5.9(1) GPa these peaks had become more intense with $\langle I/\sigma(I)\rangle = 3.1$. Integration of the data could be carried out in a primitive orthorhombic cell with dimensions a = 12.890(2), b = 12.883(1), and c = 29.015(6) Å. The clear absence of odd

reflections in the zones $h00$ and $00l$ implies space group symmetry $P2_12_12_1$. Although by 5.9 GPa, the resolution of the data had dropped to 1.2 Å and the quality was too low to solve and refine a structure for this high-pressure phase.

4.4.5 The effect of pressure on UTSA-16 in IPA

The occurrence of a pressure-induced tetragonal-to-orthorhombic transition in the UTSA-16_{MeOH} host-guest crystal motivated an attempt to lower this critical pressure by means of increasing the steric bulk of the hydrostatic medium. The increased size of the hydrostatic medium induces an effective increase in pressure, a 'chemical pressure', so the transition occurring at 4.4 GPa in methanol can be observed at much lower pressures. Isopropyl alcohol (C_3H_7OH, IPA) was chosen as the smallest secondary alcohol with the advantage of a relatively high hydrostatic limit of 4.2 GPa in the pure form (Angel *et al.*, 2007). Single-crystal diffraction data were collected at 0.5(1), 1.5(1), 2.4(1), and 3.3(1) GPa. Changes in unit-cell dimensions are shown in Figure 4.4.7(a).

At 0.5 GPa the structure is tetragonal, space group $I\bar{4}2d$, $a = 13.0479(14)$, $c = 30.056(4)$ Å. In the presence of IPA at low applied pressure, a potassium coordination site appears in the pore channel as in UTSA-16_{MeOH} (Figure 4.4.7(b)). However, this K2 site no longer lies along the four-fold axis but is instead split between symmetry-equivalent sites displaced from the $(1/2, 0, z)$ position by $(\pm 0.035, \pm 0.082, 0)$ or its symmetry equivalent $(\pm 0.082, \pm 0.035, 0)$. This reduces the site point symmetry to 1. Each possible K2 site (K2 or K2^i[$1-x, 1-y, z$]) binds to three oxygen atoms, O5, O5^i and one of either O2 or O2^i (Figure 4.4.7(b)). Refining the occupancy of the K2 site gives a value close to 1/2 which, combined with the close K2−K2^i distance of 2.14(6) Å, justifies the assignment as a disordered K^+ site. Beyond a disordered oxygen atom site no further structure could be located in the pore.

The $K2_{\mathrm{IPA}}$ site shows similar coordination distances to $K2_{\mathrm{MeOH}}$ at 4.4 GPa: 2.48(4) Å to $O5_{\mathrm{IPA}}$ and 2.71(3) Å to $O2_{\mathrm{IPA}}$ compared to 2.65(2) Å to $O5_{\mathrm{MeOH}}$ and 2.80(3) Å to $O2_{\mathrm{MeOH}}$, suggesting the increased steric bulk of the IPA molecule induces an effective pressure increase in the pore. Unlike the structure of UTSA-16_{MeOH}, the potassium ions are disordered and no coordinating water atoms could be located.

Pressurising further to 1.5 GPa induces a lowering of symmetry from a tetragonal

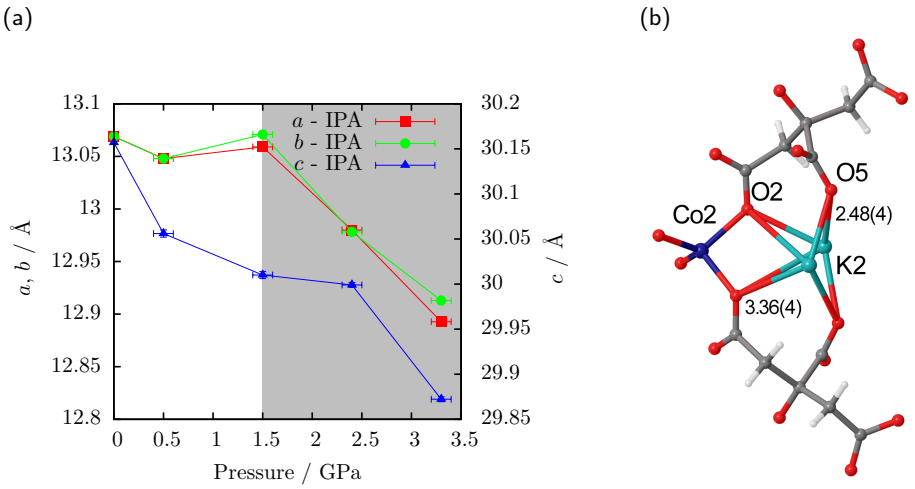

Figure 4.4.7: (a) Response of unit-cell dimensions to applied pressure for UTSA-16$_{\mathrm{IPA}}$; (b) Disorderd K2 site in UTSA-16$_{\mathrm{IPA}}$ at 0.5 GPa. Each K2 site binds to O5 and O5^{i} across the pore, and O2 and O2^{i}, shared with Co2.

body-centred to a primitive orthorhombic lattice with dimensions $a = 13.059(3)$, $b = 13.0708(13)$, and $c = 30.010(4)$ Å.

The structure of the tetragonal phase, transformed to the primitive setting, was used as a starting model. Additional potassium ions and solvent oxygen positions were located in Fourier difference maps.

Following the phase transition from $I\bar{4}2d$ to $P2_12_12_1$ (UTSA-16$_{\mathrm{IPA}}$-I to UTSA-16$_{\mathrm{IPA}}$-II), the asymmetric unit now contains four citrate anions and the four associated cobalt atoms Co1-4$_{\mathrm{II}}$ to form a single cubane along with two further cobalt atoms Co6$_{\mathrm{II}}$ and Co7$_{\mathrm{II}}$ forming the 'linker' polyhedra. The remaining components of the asymmetric unit are five potassium cations and associated coordinating oxygen atoms due to pore solvent.

Once again the cubane motif remains unaffected by changes in the rest of the structure; both bond angles and distances are not statistically different from their ambient pressure values. The most notable structural change is the presence of additional oxygen atoms coordinating to the previously tetrahedral Co2$_{\mathrm{I}}$ sites creating two new octahedral cobalt sites Co6$_{\mathrm{II}}$ and Co7$_{\mathrm{II}}$ as shown in Figure 4.4.8(a) and (b), along with neighbouring K atoms.

No further electron-density peaks could be discerned around the additional oxygen atoms suggesting they are due to pore water, the occupancies of the additional po-

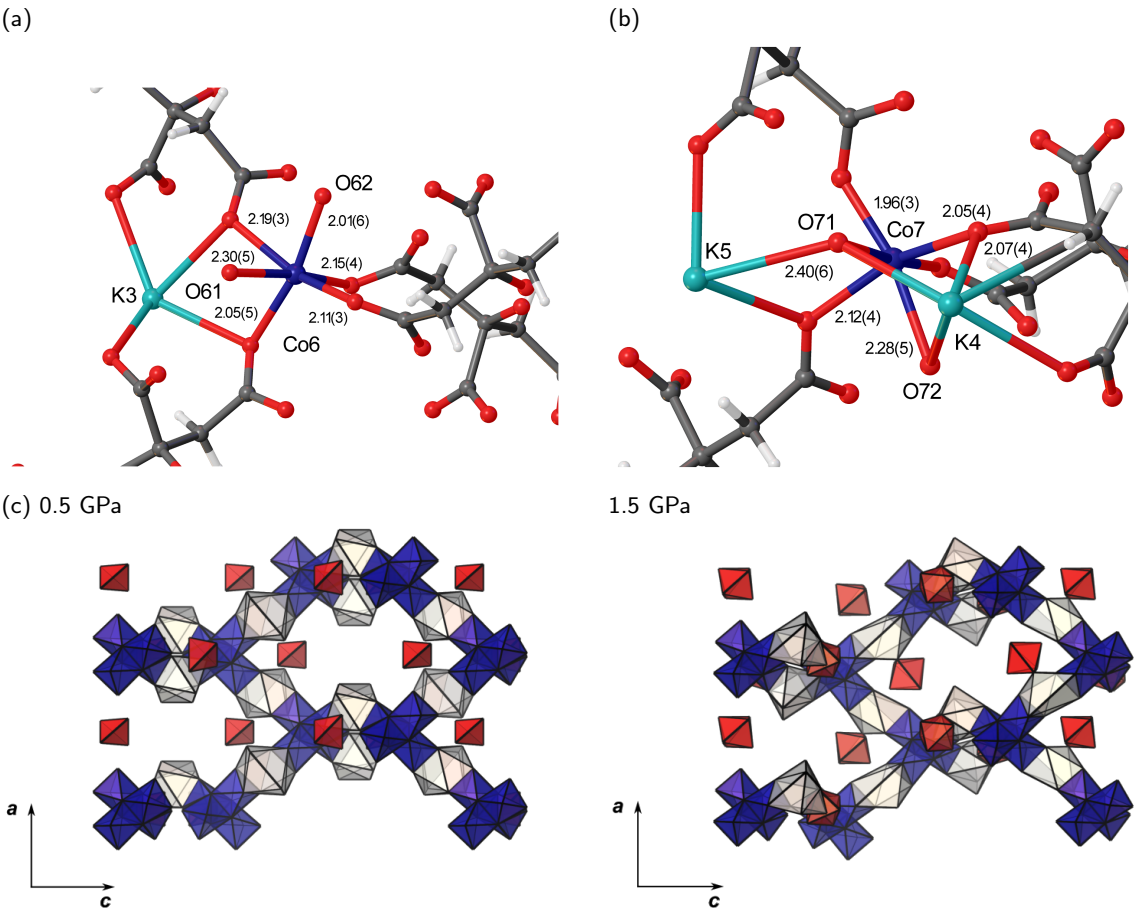

Figure 4.4.8: Structural changes during the tetragonal-orthorhombic phase transition of UTSA-16$_{IPA}$-I to UTSA-16$_{IPA}$-II. The tetrahedral Co2$_I$ site is transformed by oxygen atom coordination to two octahedral sites Co6$_{II}$ and Co7$_{II}$.; (a) K3 is fully ordered and binds to the edge of the Co6$_{II}$ octahedron; (b)K4$_{II}$ and K5$_{II}$ are partially occupied. K4$_{II}$ occupies a face-sharing site on the Co7$_{II}$ octahedron, K5$_{II}$ occupies the channel site like K3$_{II}$. Oxygen sites O61, O62, O71, and O72 appear to be formed by water molecules displaced from the pore during the UTSA-16$_{IPA}$-I→II phase transition; (c) The change from tetrahedral to octahedral symmetry of the Co2 tetrahedra induces significant framework distortion as illustrated by the polyhedral representations above and below the critical pressure. Cobalt octahedra are shown in dark blue (Co1$_I$ and Co1$_{II}$, Co2$_{II}$, Co3$_{II}$, and Co4$_{II}$), cobalt tetrahedra and former tetrahedra sites (Co2$_I$ and Co6$_{II}$, and Co7$_{II}$) are shown in red, irregular potassium polyhedra are shown in white.

tassium atoms were fixed to match the composition determined by EDS. Former $Co2_I$ sites $Co6_{II}$ and $Co7_{II}$, no longer lie on special positions and form six unique Co−O bonds.

The $Co6_{II}$ coordination environment (Figure 4.4.8(a)) is a distorted octahedron, average bond length 2.14(4) Å, with all bonds being statistically similar. The $Co6_{II}$ octahedra share two coordinating citrate oxygen atoms with one fully-occupied potassium ion site, $K3_{II}$, which adopts one of the possible channel sites disordered by symmetry in the tetragonal phase. These K−O bond lengths are not significantly different to those observed at 0.5 GPa.

The situation surrounding $Co7_{II}$ is more complex; two disordered K sites are apparent (Figure 4.4.8(b)). The first, $K4_{II}$, occupies the channel site, as was the case around $Co6_{II}$, again with similar K−O bond lengths compared to those observed at 0.5 GPa, the occupancy was fixed at 0.5. A second site, $K5_{II}$ (also with fixed occupancy 0.5) binds to the face of $Co7_{II}$ octahedron formed by the additional 'new' oxygen atoms O71, O72, and framework citrate atom O22. Both coordination environments are shown in Figure 4.4.8(b). In contrast to the environment of $Co6_{II}$, the Co7−O71 bond is 0.25(7) Å longer than the pre-existing framework bonds of an average 2.15(4) Å. This reflects the fact that O71 and O72 are both shared with coordinating potassium ion $K5_{II}$.

$Co6_{II}$ octahedra link cubanes within the *bc*-plane, $Co7_{II}$ through the *ac*-plane. The changes to the coordination environments of both the potassium and cobalt atoms have consequences for the relative arrangements of cubane structures; the symmetry-breaking coordination of oxygen to $Co6_{II}$ and $Co7_{II}$, and the induced changes in K-linker geometry, lead to significantly different cubane-K distances, altering the framework topology. K1 now shows two different K−Co distances: 3.450(19) and 3.65(3) Å, likewise for K2: 3.46(3) and 3.65(3) Å. The end result is a distorted framework with skewed cubane-cubane distances, especially pronounced in the *ac*-plane as shown in Figure 4.4.8(c). No further changes in coordination occur for the cobalt moieties up to 3.3 GPa. At 3.3 GPa two additional oxygen atom sites can be located in the pore, coordinating to $K3_{II}$ and $K5_{II}$.

Changes in cobalt coordination environment in framework materials are well documented and typically involve substitution (Takaoka *et al.*, 2005) or removal of small

solvent molecules either upon heating or exposure to a small molecule vapour or liquid (Maspoch *et al.*, 2003). In these transitions the coordination number of the cobalt site decreases on heating, examples include a decrease from octahedral (CN = 6) to trigonal bipyramid (CN = 5) or square pyramidal (CN = 5) upon removal of water (Zeng *et al.*, 2009). The substitution of ligands can proceed either by concerted ligand substitution (Bradshaw *et al.*, 2007) or *via* stable desolvated apohost structures (Chen *et al.*, 2005).

4.5 Conclusions

In conclusion, the framework material UTSA-16 has been shown to exhibit negative linear compressibility along the tetragonal *c*-axis. This behaviour is not a result of the network connectivity, as shown in other MOFs, but due to distortions within torsionally-flexible cobalt(II) tetrahedra which link together rigid Co_4O_4 units based on distorted cobalt(II) octahedra. The soft torsional distortion allows the framework to compress in the *a*- and *b*-directions while expanding along **c**.

The mechanism of NLC in UTSA-16 illustrates how the modular-nature of MOF structures might be exploited to create frameworks with a combination of inflexible function-specific secondary-building units and flexible linking units to induce NLC alongside other desired properties.

Interaction of MOF UTSA-16 with methanol at ambient pressure leads to ordering and subsequent observation of potassium ions, previously undetected in this material, driven by an excess of methanol. At 5.9 GPa this system undergoes a phase transition to a lower symmetry orthorhombic cell with $P2_12_12_1$ space-group symmetry. However the detrimental effects of high pressure on the crystal quality prohibited a structure solution.

At low applied pressure the tetragonal UTSA-16_{IPA}-I structure exhibits similar 'channel' potassium ions as observed in UTSA-16_{MeOH}. UTSA-16_{IPA}-I also undergoes a phase transition to an orthorhombic $P2_12_12_1$ structure (phase UTSA-16_{IPA}-II); however by substituting isopropyl alcohol for methanol, the critical pressure is reduced by 4.4 GPa from 5.9 GPa to 1.5 GPa. Solution and refinement of this new phase showed the symmetry-breaking coordination of oxygen atoms to the tetrahedral Co^{2+} sites which

drives this transition. As for a wide range of materials, increasing pressure leads to an increase in coordination number of the metal centre in UTSA-16$_{\mathrm{IPA}}$, but crucially only in the presence of a suitable small molecule guest. The origin of the differing mechanical properties (Figure 4.4.3 and Table 4.4.1) of UTSA-16 in the three hydrostatic media lies in coordination changes at the flexible Co tetrahedra. Under pure hydrostatic compression in FC70, these tetrahedra induce a negative linear compressibility effect *via* torsional flexing. In UTSA-16$_{\mathrm{MeOH}}$-I, the filling of the pores and the shared coordination with ordered potassium cations suppresses this motion resulting in positive axial compressibilities. The pressure-driven UTSA-16$_{\mathrm{IPA}}$-I→II transition results in the replacement of flexible Co tetrahedral with rigid octahedral units. The resulting reduced compressibility shows that these secondary-building units play a critical role in determining the mechanical strength of this framework material in both penetrating and non-penetrating hydrostatic media.

Pressure / GPa	Ambient	0.3(1)	0.5(1)	1.0(1)
Crystal data				
Formula	$([K_{1.8}Co_3(C_6H_4O_7)(C_6H_{4.2}O_7)(H_2O)_2]\cdot 8.3H_2O)_n$			
Formula weight	803.36			
Crystal system	Tetragonal			
Space group	$I\bar{4}2d$ (No. 122)			
a, c / Å	13.0691(4)	13.0005(5)	12.8201(5)	12.6111(5)
	30.157(1)	30.2002(11)	30.2685(12)	30.2999(11)
Volume / Å^3	5150.9(4)	5104.2(4)	4974.8(4)	4818.9(4)
Z	8			
Crystal size / mm	0.15 x 0.15	0.15 x 0.15	0.15 x 0.15	0.15 x 0.15
	x 0.50	x 0.45	x 0.45	x 0.45
Data collection				
θ_{min}, θ_{max} / °	1.7, 25.3	3.7, 24.1	3.7, 24.7	3.7, 24.4
Radiation / Å	Mo$K\alpha$ (0.71073)			
$h_{min} : h_{max}$	−11: 11	−8: 8	−7: 7	−7: 7
$k_{min} : k_{max}$	0: 15	0: 13	0: 13	0: 13
$l_{min} : l_{max}$	0: 36	0: 34	0: 34	0: 34
Total and unique data, R_{int}	24384, 2365,	7155, 1476,	7130, 1515,	6416, 1397,
	0.046	0.048	0.050	0.052
Observed data ($I > 2\sigma(I)$)	2187	1282	1337	1217
Refinement				
N_{ref}, N_{par}	2187, 164	1282, 149	1260, 154	1155, 154
R, $wR2$, S	0.0353, 0.0944,	0.0576, 0.3531,	0.0672, 0.2657,	0.0774, 0.2688,
	1.13	0.95	1.02	1.02
Flack x	0.04(2)	0.07(5)	0.08(5)	0.13(7)
$\Delta\rho_{min}$, $\Delta\rho_{max}$ / e Å^{-3}	−0.57, 0.76	−0.52, 1.14	−0.77, 1.39	−0.72, 2.25

Table 4.5.1: Crystallographic data for the UTSA-16$_{\mathrm{FC70}}$ pressure series.

Pressure / GPa	Ambient (MeOH)	0.35(10)	2.2(1)	4.4(1)
Crystal data				
Formula	$([K_{1.8}Co_3(C_6H_4O_7)(C_6H_{4.2}O_7)(H_2O)_2]\cdot 8.3H_2O)_n$			
Formula weight	803.36			
Crystal system	Tetragonal			
Space group	$I\bar{4}2d$ (No. 122)			
a, c / Å	13.367(3), 30.052(9)	13.4246(15), 30.015(5)	13.3530(5), 29.424(3)	13.0417(7), 29.096(4)
Volume / Å^3	5370(3)	5409.3(15)	5246.4(7)	4948.8(9)
Z	8			
Crystal size / mm	0.10 x 0.10 x 0.20	0.10 x 0.15 x 0.30	0.10 x 0.10 x 0.20	0.10 x 0.10 x 0.20
Data collection				
θ_{min}, θ_{max} / °	1.7, 17.2	3.3, 17.1	3.4, 22.0	3.1, 18.6
Radiation / Å	Mo$K\alpha$ (0.71073)			
$h_{min} : h_{max}$	−7: 7	−7: 6	−9: 9	−8: 8
$k_{min} : k_{max}$	0: 11	0: 11	2: 14	2: 11
$l_{min} : l_{max}$	0: 24	0: 24	0: 21	0: 18
Total and unique data, R_{int}	3852, 814, 0.148	3312, 731, 0.095	6482, 1140, 0.077	5317, 699, 0.081
Observed data ($I > 2\sigma(I)$)	679	591	952	644
Refinement				
N_{ref}, N_{par}	802, 90	722, 88	1122, 72	690, 68
R, $wR2$, S	0.1068, 0.2120, 0.95	0.0768, 0.2090, 1.18	0.1061, 0.3206, 0.97	0.1637, 0.3824, 0.93
Flack x	0.16(15)	0.01(14)	0.05(13)	0.6(2)
$\Delta\rho_{min}$, $\Delta\rho_{max}$ / e Å^{-3}	−2.20, 1.66	−1.03, 1.59	−1.79, 2.32	−1.86, 1.56

Table 4.5.2: Crystallographic data for the UTSA-16$_{\mathrm{MeOH}}$ pressure series.

Pressure / GPa	Ambient	0.5(1)	2.4(1)
Crystal data			
Formula	$([K_{1.8}Co_3(C_6H_4O_7)(C_6H_{4.2}O_7)(H_2O)_2]\cdot 8.3H_2O)_n$		
Formula weight	803.36		
Crystal system	Tetragonal	Tetragonal	Orthorhombic
Space group	$I\bar{4}2d$ (No. 122)	$I\bar{4}2d$ (No. 122)	$P2_12_12_1$ (No. 19)
a, b, c / Å	13.0691(4), 13.0691(4), 30.157(1)	13.0479(14), 13.0479(14), 30.056(4)	12.9782(10), 12.9799(16), 29.999(3)
Volume / Å^3	5150.9(4)	5117.0(13)	5053.5(9)
Z	8		
Crystal size / mm	0.15 x 0.15 x 0.50	0.12 x 0.12 x 0.16	0.12 x 0.12 x 0.16
Data collection			
θ_{min}, θ_{max} / °	1.7, 25.3	3.7, 18.9	3.1, 17.7
Radiation / Å	Mo$K\alpha$ (0.71073)		
$h_{min} : h_{max}$	−11: 11	−8: 7	−11: 11
$k_{min} : k_{max}$	0: 15	0: 11	0: 9
$l_{min} : l_{max}$	0: 36	0: 27	0: 25
Total and unique data, R_{int}	24384, 2365, 0.046	4354, 903, 0.098	8122, 2610, 0.108
Observed data ($I > 2\sigma(I)$)	2187	899	2574
Refinement			
N_{ref}, N_{par}	2187, 164	899, 93	2574, 280
R, $wR2$, S	0.0353, 0.0944, 1.13	0.0765, 0.2042, 1.07	0.1150, 0.3267, 0.96
Flack x	0.04(2)	0.01(11)	-
$\Delta\rho_{min}$, $\Delta\rho_{max}$ / e Å^{-3}	−0.57, 0.76	−0.92, 0.95	−1.42, 1.55

Table 4.5.3: Crystallographic data for the UTSA-16$_{\mathrm{IPA}}$ pressure series.

4.6 References

Allen F H 2002 *Acta Crystallographica Section B* **58**(3 Part 1), 380–388.

Allendorf M D, Bauer C A, Bhakta R K and Houk R J T 2009 *Chem. Soc. Rev.* **38**, 1330–1352.

Altomare A, Cascarano G, Giacovazzo C and Guagliardi A 1993 *Journal of Applied Crystallography* **26**(3), 343–350.

Angel R J, Alvaro M and Gonzalez-Platas J 2014 *Zeitschrift für Kristallographie - Crystalline Materials* **229**(5), 405–419.

Angel R J, Bujak M, Zhao J, Gatta G D and Jacobsen S D 2007 *Journal of Applied Crystallography* **40**(1), 26–32.

Betteridge P W, Carruthers J R, Cooper R I, Prout K and Watkin D J 2003 *Journal of Applied Crystallography* **36**(6), 1487.

Birch F 1986 *Journal of Geophysical Research: Solid Earth (1978-2012)* **91**(B5), 4949–4954.

Bradshaw D, Warren J E and Rosseinsky M J 2007 *Science* **315**(5814), 977–980.

Bruker 2007 '*SAINT*'.

Cairns A B, Catafesta J, Levelut C, Rouquette J, Van Der Lee A, Peters L, Thompson A L, Dmitriev V, Haines J and Goodwin A L 2013 *Nature materials* **12**(3), 212–216.

Chapman K W, Halder G J and Chupas P J 2008 *Journal of the American Chemical Society* **130**(32), 10524–10526.

Chen C L, Goforth A M, Smith M D, Su C Y and zur Loye H C 2005 *Angewandte Chemie International Edition* **44**(41), 6673–6677.

Dawson A, Allan D R, Parsons S and Ruf M 2004 *Journal of Applied Crystallography* **37**(3), 410–416.

Duriska M B, Neville S M, Moubaraki B, Cashion J D, Halder G J, Chapman K W, Balde C, Létard J F, Murray K S, Kepert C J *et al.* 2009 *Angewandte Chemie* **121**(14), 2587–2590.

Fairen-Jimenez D, Moggach S, Wharmby M, Wright P, Parsons S and Düren T 2011 *Journal of the American Chemical Society* **133**(23), 8900–8902.

Gagnon K J, Beavers C M and Clearfield A 2013 *Journal of the American Chemical*

Society **135**(4), 1252–1255.

Gatt R and Grima J N 2008 *Physica Status Solidi (RRL) - Rapid Research Letters* **2**(5), 236–238.

Graham A J, Allan D R, Muszkiewicz A, Morrison C A and Moggach S A 2011 *Angewandte Chemie* **123**(47), 11334–11337.

Halder G J, Kepert C J, Moubaraki B, Murray K S and Cashion J D 2002 *Science* **298**(5599), 1762–1765.

Kreno L E, Leong K, Farha O K, Allendorf M, Duyne R P V and Hupp J T 2012 *Chemical Reviews* **112**(2), 1105–1125.

Kurmoo M 2009 *Chem. Soc. Rev.* **38**, 1353–1379.

Li J R, Sculley J and Zhou H C 2012 *Chemical Reviews* **112**(2), 869–932.

Li W, Henke S and Cheetham A K 2014 *APL Mater.* **2**(12).

Lock N, Wu Y, Christensen M, Cameron L J, Peterson V K, Bridgeman A J, Kepert C J and Iversen B B 2010 *The Journal of Physical Chemistry C* **114**(39), 16181–16186.

Mary T A, Evans J S O, Vogt T and Sleight A W 1996 *Science* **272**(5258), 90.

Maspoch D, Ruiz-Molina D, Wurst K, Domingo N, Cavallini M, Biscarini F, Tejada J, Rovira C and Veciana J 2003 *Nature Materials* **2**(3), 190–195.

McKellar S C, Graham A J, Allan D R, Mohideen M I H, Morris R E and Moggach S A 2014 *Nanoscale* **6**, 4163–4173.

Merrill L and Bassett W A 1974 *Review of Scientific Instruments* **45**(2), 290–294.

Moggach S A, Allan D R, Parsons S and Warren J E 2008 *Journal of Applied Crystallography* **41**(2), 249–251.

Moggach S, Bennett T and Cheetham A 2009 *Angewandte Chemie* **121**(38), 7221–7223.

Ogborn J M, Collings I E, Moggach S A, Thompson A L and Goodwin A L 2012 *Chem. Sci.* **3**, 3011–3017.

Parsons S 2004 '*SHADE*, program for empirical absorption corrections to high pressure data'.

Piermarini G J, Block S, Barnett J D and Forman R A 1975 *Journal of Applied Physics* **46**(6), 2774–2780.

S. O. Evans J 1999 *J. Chem. Soc., Dalton Trans.* pp. 3317–3326.

Sheldrick G M 1996 '*SADABS*, a program for empirical absorption correction of area

detector data'.

Spek A L 2009 *Acta Crystallographica Section D* **65**(2), 148–155.

Spek A L 2015 *Acta Crystallographica Section C* **71**(1), 9–18.

Takaoka K, Kawano M, Tominaga M and Fujita M 2005 *Angewandte Chemie International Edition* **44**(14), 2151–2154.

Tan J C and Cheetham A K 2011 *Chem. Soc. Rev.* **40**, 1059–1080.

Wang X S, Chrzanowski M, Wojtas L, Chen Y S and Ma S 2013 *Chemistry - A European Journal* **19**(10), 3297–3301.

Xiang S, He Y, Zhang Z, Wu H, Zhou W, Krishna R and Chen B 2012 *Nature Communications* **3**, 954.

Xiang S, Wu X, Zhang J, Zhang J, Fu R, Hu S and Zhang X Z X 2005 *Journal of the American Chemical Society* **127**(47), 16352–16353.

Yu J, Cui Y, Wu C, Yang Y, Wang Z, O'Keeffe M, Chen B and Qian G 2012 *Angewandte Chemie International Edition* **51**(42), 10542–10545.

Zeng M H, Hu S, Chen Q, Xie G, Shuai Q, Gao S L and Tang L Y 2009 *Inorganic Chemistry* **48**(15), 7070–7079.

Chapter 5

Phase Transition Sequences in Hybrid Organic-Inorganic Salts

5.1 Synopsis

The phase transition sequences of two members of the tetramethylammonium tetrachlorometallate(III) ($[NMe_4]^+[MCl_4]^-$) family of hybrid organic-inorganic salts have been determined and structurally-characterised as a function of temperature for the first time. Unusually, we observe a reduction in point-group symmetry with increasing temperature until reaching a cubic prototype phase. This prototype phase is present over a narrow (*ca.* 2 K) temperature range and is characterised by significant diffuse scattering due to hindered-rotation of the tetrahedral component ions. Two additional intermediate phases are observed for M = Fe^{3+}. First-principles calculations and the presence of short Cl...Cl contacts for M = Ga^{3+} suggest the $[GaCl_4]^-$ anion to be conformationally hindered due to stronger lone-pair-σ-hole interactions.

The additional intermediate phases allow a lower-energy pathway to the prototype phase than is possible for M = Ga^{3+}. The conformationally more flexible M = Fe^{3+} anion results in a phase exhibiting sublattice disordering with the onset of rotational disorder in the $[NMe_4]^+$ cations occurring 40 K below the corresponding onset of rotational disorder in the $[FeCl_4]^-$ sublattice. This structure is not adopted with M = Ga^{3+}, and as a result both ions become disordered simultaneously upon the transition to the cubic plastic phase.

5.2 Introduction

Alkylammonium tetrahalometallates of various *d*-block metals ($[NR_4]_n{}^+[MX_4]^{n-}$, where R = H, Me, Et, *etc.*, and X = Cl, Br) are inorganic-organic hybrid systems which, despite their apparent simplicity, display a wealth of different physical properties and rich phase diagrams containing ferromagnetic, ferroelectric, ferroelastic, and incommensurate phases within a range of relatively mild thermodynamic conditions (López-Echarri *et al.*, 1990; Ruiz-Larrea *et al.*, 2000)

The very earliest studies of these materials were primarily concerned with elucidating the geometries of tetrahedral metal clusters such as $[CuCl_4]^-$ (Morosin and Lingafelter, 1959, 1961). Following the discovery of ferroelectricity in *bis*-tetramethylammonium tetrachlorozincate(II) ($[NMe_4]_2ZnCl_4$) by Sawada *et al.* (1978), numerous experimental

and theoretical studies of the *bis*-tetramethylammonium tetrahalometallates ($[NMe_4]_2[MX_4]$) have uncovered a complex but general phase diagram for M = Zn^{2+}, Co^{2+}, Fe^{2+}, Mn^{2+}, and Cu^{2+} (Shimizu *et al.*, 1980; Styczeń *et al.*, 2008; Zubillaga *et al.*, 1988; Clay *et al.*, 1975). These systems have become archetypal models for studying disordered→incommensurate→commensurate phase sequences (López-Echarri *et al.*, 1985). As for all materials in this class, the relationships between phases are governed by the orientations of component ions reflecting subtle changes in response to both temperature and pressure (Barreda-Argüeso *et al.*, 2014).

The range of structure types can be extended even further by selective or complete substitution of R groups. For example, *bis*-propylammonium tetrachloromanganate ($[C_3H_7NH_3]_2[MnCl_4]$) has been shown to adopt a pseudo-perovskite structure more commonly found in inorganic materials (Muralt *et al.*, 1982). Recently, related hybrid organic-inorganic trihalide pseudo-perovskite materials such as methylammonium lead iodide ($MeNH_3PbI_3$), have attracted significant attention as components of high-efficiency solar cells (Lee *et al.*, 2012). Substitution of the methyl groups for ethyl groups produces a new range of materials whose structures and phase sequences have only recently been fully characterised (Wolthuis *et al.*, 1986; Mahoui *et al.*, 1996; Kandhaswamy and Srinivasan, 2002; Lutz *et al.*, 2014).

The subset of alkylammonium tetrahalometallates with R = Me, and $n = 1$, have not been subject to the same systematic phase determination as for $n = 2$. Gośniowska *et al.* (2000) report calorimetry results suggesting three first-order transitions for tetramethylammonium tetrabromoindate(III) ($[NMe_4][InBr_4]$), although structures for all three phases were elusive. Lenck *et al.* (1991) present a study of three members of tetralkylammonium tetrachlorothallates(III). They report a single phase transition as determined by solid-state NMR for the tetramethylammonium member of the series.

Tetramethylammonium tetrachloroferrate(III) ($[NMe_4][FeCl_4]$, TCF) like other compounds of alkylammonium cations, has attracted attention for the numerous phase transitions reported in the relatively narrow range of temperatures from 220 to 400 K. In comparison to the analogues reported above, TCF is notable for the large number of reported transitions.

Czapla *et al.* (1985) report successive phase transitions (upon heating) at 291, 303,

314, 322, 347, and 384 K detected by differential scanning calorimetry (DSC) measurements. Above 520 K the material decomposes. Subsequently Ruiz-Larrea *et al.* (1987) carried out adiabatic calorimetry and DSC measurements and report phase transitions (upon heating) at 236.1, 291, 307, 347, and 381 K.

Optical microscopy observations and linear birefringence measurements by Kosturek *et al.* (1999) confirmed the presence of four first-order transitions at 385, 303, 294, and 265 K on cooling. The loss of all optical anisotropy above 385 K indicated the high-temperature prototype phase cannot be tetragonal, as proposed by Ruiz-Larrea *et al.,* but cubic instead. Kosturek *et al.* and others note that transitions in this material are subject to very large thermal hystereses and the exact critical temperature of a transition is very much dependent upon the thermal history of the sample. As an illustration, in the temperature range of 303 K to 307 K TCF can exist in one of three phases depending upon the heating regime to which it has been subjected.

The only crystal structure reported so far was first described (at room temperature) by Czapla and Ruiz-Larrea to be orthorhombic, space group $Pmc2_1$ whereas Wyrzykowski *et al.* (2008) report a corrected space group $Pma2$ with $a = 14.2746(12)$, $b = 6.4431(5)$, and $c = 6.4401(5)$ Å. Czapla *et al.* also carried out measurements of dielectric constant with temperature, finding a hundred-fold increase at the $T_c = 386$ K transition (Czapla *et al.*, 1985).

Tetramethylammonium tetrachlorogallate(III) ($[NMe_4][GaCl_4]$, TCG), is a previously unreported analogue to TCF. The literature contains structural information on one other $[NMe_4][MCl_4]$ salt, tetramethylammonium tetrachlorothallate $[NMe_4][TlCl_4]$, which is reported to crystallise at room temperature in space group $Cmmm$ with $a = 9.132(4)$, $b = 8.946(4)$, and $c = 7.525(3)$ Å with both ions disordered and no carbon atoms located (Lenck *et al.*, 1991).

Here we report and analyse the sequence of phases present in TCF and TCG upon heating at temperatures from 100 K to amorphisation at *ca.* 400 K. Unusually, the symmetry of both materials decreases upon heating until the high-symmetry plastic phases present in a narrow range at high-temperature. In TCF, symmetry reduction occurs *via* a sequence of phases which show a step-wise loss of orientational correlation. TCG shows fewer intermediate steps; orientational correlation is lost entirely in one

step before the onset of full rotational disorder.

5.3 Methods

5.3.1 Crystallisation, X-ray diffraction and other measurements

Single-crystals of TCF were prepared by the addition of an aqueous solution (20 ml) of NMe_4Cl (tetramethylammonium chloride, 0.1096 g, 1 mmol) to an aqueous solution (20 ml) of $FeCl_3$ (iron chloride(III) 0.1622 g, 1 mmol). The resulting precipitate was dissolved in ethanol, slow evaporation afforded crystals suitable for X-ray diffraction. Crystals of TCG were provided courtesy of Prof. Rafael Valiente of the University of Cantabria and were grown by slow evaporation at 30°C of acidified aqueous solution (HCl 3 mol l^{-1}) containing NMe_4Cl and $GaCl_3{\cdot}6H_2O$ in a 1:1 stoichiometric ratio. The acid is added to avoid oxidation of the trivalent anions and the formation of hydroxides or other compounds. After several weeks single crystals of about 1 mm size are formed.

Single-crystal diffraction data were collected on an Agilent Supernova using a Mo $K\alpha$ microsource (λ = 0.71073 Å) equipped with an Oxford Cryosystems variable-temperature device. Data were integrated using *Crysalis PRO*, absorption corrections were carried out in *ABSPACK* (Agilent, 2014).

Variable temperature powder diffraction data were collected using a Bruker D8 ADVANCE diffractometer equipped with a Lynxeye position-sensitive detector and an Oxford Cryosystems low-temperature device. The radiation source was Ge-monochromated Cu $K\alpha1$. The temperature stability of the variable-temperature device was ±0.1 K over a temperature range of 120 to 400 K. For the 5 and 10 K steps a ramp rate of 10 K hr^{-1} was used, this was increased 360 K hr^{-1} for larger steps. The temperature was equilibrated for at least 30 minutes before collections. Unit-cell dimensions were determined by Le Bail fitting carried out in *JANA2006* (Petříček *et al.*, 2014) and fitted to a Berman thermal equation of state in *EOSFIT 7.0* to determine thermal expansivities (Berman, 1988; Angel *et al.*, 2014).

Differential scanning calorimetry (DSC) was carried out over the temperature range 100 K to 400 K at the Thermal Analysis Facility at The University of Durham.

5.3.2 Refinement and twinning

We shall refer to the different phases observed in this study by means of their Pearson symbols, in which the first two letters specify the Bravais lattice and the following figure indicates the number of atoms in the unit cell. For TCF five phases were observed, and in increasing order of temperature these are: TCF-$oP88$, TCF-$oP44$, TCF-$mP22$, TCF-$mP44$, and TCF-$cP22$. Three phases were observed for TCG: TCG-$oP88$, TCG-$mP22$, and TCG-$cP22$.

Structures were solved in *SIR92* (Altomare *et al.*, 1993) or *SUPERFLIP* (Palatinus and Chapuis, 2007), refinements were carried out against $|F|^2$ in *CRYSTALS* (Betteridge *et al.*, 2003) or *SHELXL* (Sheldrick, 2015). Rigid-body and rigid-bond restraints were applied to the $[NMe_4]^+$ cation for TCF-$mP22$, TCG-$mP22$, and TCF-$oP44$. The refinement of phases TCF-$mP22$ and TCG-$mP22$ also required the use of bond-angle and bond-distance restraints on the $[NMe_4]^+$ cation. The structures of phases TCF-$mP44$, TCF-$cP22$, and TCG-$cP22$ contain rotationally disordered $[NMe_4]^+$ cations which were modelled using the spherical-shell shape implemented in *CRYSTALS* (Schröder *et al.*, 2004). The shell model has six refinable parameters four of which, the occupancy and the coordinates of the centre of the sphere, were held fixed. The radius and isotropic displacement factor were allowed to vary.

Although most crystals of TCF suffered from twinning, a sample was eventually found which consisted of one domain in the TCF-$oP88$ and TCF-$oP44$ phases. This sample was used in the determination of phases TCF-$oP88$, TCF-$oP44$, and TCF-$mP22$. Due to degradation of the sample, a second crystal was used for the structure determination of TCF-$mP44$. For TCG, the fourfold twin law was observed at 300 K in a crystal picked from the mother liquor. This crystal was the cooled and the same fourfold rotation was confirmed to persist in TCG-$oP88$ and domains could be separated and data were integrated and refined as a single domain.

The structures of TCF-$mP22$ and TCG-$mP22$ could both be indexed using orthorhombic C-centered cells, with apparent space group $Cmmm$. Unit-cell dimensions for TCF were $a = 8.9739(19)$, $b = 9.204(2)$, and $c = 7.1747(12)$ Å; those for TCG were $a = 9.027(11)$, $b = 9.235(13)$, and $c = 7.1473(9)$ Å. Solutions of these structures yielded

Phase	Space group	T / K	a / Å	b / Å	c / Å	β / °	V / Å^3	Twin laws (scale factor)	Basis transformation
TCF-$oP88$	$Pbma$	220	13.1442(8)	13.9946(8)	6.4272(3)	90	1182.27(11)	-	-
TCF-$oP44$	$Pbm2$	295	6.4471(5)	14.2753(11)	6.4526(5)	90	593.86(8)	-	$\frac{a}{2}, b, c$
TCF-$mP22$	Pm	318	6.425(3)	7.1480(16)	6.4274(18)	91.21(3)	295.10(16)	$4_{[010]}$: 0.358(13), $2_{[100]}$: 0.155(11), $2_{[101]}$: 0.094(4)	$a, \frac{b}{2}, c$
TCF-$mP44$	$P2_1/m$	365	6.574(3)	14.156(7)	6.594(3)	93.86(4)	612.26(10)	$4_{[010]}$: 0.496(18)	$a, 2b, c$
TCF-$cP22$	$Pm\bar{3}m$	385	6.842(3)	6.842(3)	6.842(3)	90	320.32(4)	-	-
TCG-$oP88$	$Pbma$	226	12.8329(7)	14.1248(4)	6.3718(3)	90	1154.97(9)	$4_{[010]}$: $< 1\%$	-
TCG-$mP22$	Pm	300	6.4478(14)	7.1316(7)	6.4451(8)	91.399(14)	296.28(8)	$4_{[010]}$: 0.463(7)	$\frac{a}{2}, \frac{b}{2}, c$
TCG-$cP22$	$Pm\bar{3}m$	393	6.8504(4)	6.8504(4)	6.8504(4)	90	321.48(3)	-	-

Table 5.3.1: Summary of TCF and TCG phases and unit cell dimensions from single-crystal diffraction data.

Phase	T/ K	No. reflections in domain 1	No. reflections in domain 2	No. reflections overlapped
TCF-$mP22$	318	1046	899	1635
TCF-$mP44$	365	2012	1941	1907
TCG-$oP88$	226	6412	822	3370
TCG-$mP22$	300	2204	723	1656

Table 5.3.2: Indexing information for twinned phases of TCF and TCG.

highly disordered models exhibiting poor fits to the data. However, split high-angle peaks suggested that the symmetry was in fact monoclinic. Re-indexing revealed two metrically pseudo-tetragonal monoclinic domains twinned by pseudo-merohedry.

The unit-cell dimensions of TCF-$mP22$ were $a = 6.425(3)$, $b = 7.1480(16)$, and $c = 6.4274(18)$ Å, $\beta = 91.21(3)°$. A total of 3580 reflections were indexed; 1046 were assigned to domain 1 only, 899 to domain 2 with the remaining number overlapped, a total of 279 reflections were unindexed. The relationship between the orientation matrices of the two indexed domains was a rotation of 90° about the b-axis, expressed by the twin law 5.3.1.

$$\begin{pmatrix} 0 & 0 & \bar{1} \\ 0 & 1 & 0 \\ 1 & 0 & 0 \end{pmatrix} \tag{5.3.1}$$

Coset decomposition of point group $4/mmm$ with respect to point group $2/m$ gives a total of four possible domains and in addition to the fourfold rotation around the b-axis identified during indexing, two further twin laws, a twofold rotation around the a-axis and a twofold rotation about the ac face-diagonal, were applied during the refinement of TCF-$mP22$ (Flack, 1987; Schlessman and Litvin, 1995). Refined twin scale factors were 0.393(12), 0.358(13), 0.155(11), and 0.094(4). This twinning model neglects the absolute structure of the four domains, which would require the addition of a further four twin laws given by the decomposition of $4/mmm$ into m (these laws are obtained by the addition of an inversion operator to each of the four domains in the model). Attempts to include these twin laws into the model led to refinement instabilities.

Data were collected on a crystal of TCG-$mP22$ selected directly from the mother

liquor. Again two monoclinic domains could be identified, related by a 90° rotation about the b-axis, with unit-cell dimensions a = 6.4478(14), b = 7.1316(7), and c = 6.4451(8) Å, β = 91.399(14)°. Of the 4615 reflections used for indexing, 2204 were assigned to domain 1, 723 to domain 2 only, with 1656 overlapped reflections; the remaining 32 reflections could not be assigned to either domain. Refinement was carried out using a two-domain model with the fourfold rotation given above; the additional twin laws ($2_{[100]}$ and$2_{[101]}$) gave no improvement to the R-factor. The final twin scale factor was 0.463(7). The same domains were also present in TCG-oP88 obtained on cooling.

Analysis of the TCF-mP22 and TCG-mP22 phases was attempted in space groups $P2$, $P2/m$, Pm. Only the refinements in Pm gave reasonable bond lengths and acceptable R-factors. The existence of twinning *via* a fourfold rotation in the mP22 phases of TCF and TCG seems paradoxical because this operation is not part of the point group symmetry of the lower-temperature oP88 or oP44 phases. The twin law is thus not 'inherited' from the symmetry or domain structure of the orthorhombic phases, and its provenance is unclear. Details of indexing, twin laws, scale factors, and lattice transformations are given in Tables 5.3.1 and 5.3.2.

5.3.3 Computational method

Geometry optimisation calculations were carried out using the plane-wave density-functional theory computational package *CASTEP 6.11* (Clark *et al.*, 2005). The generalised gradient approximation, as expressed in the Perdew-Burke-Ernzerhof (PBE) exchange-correlation functional, was used with 'on-the-fly' pseudopotentials generated by *CASTEP* and the TS semi-empirical dispersion correction scheme (Perdew *et al.*, 1996; Tkatchenko and Scheffler, 2009). Basis set kinetic energy cut-offs and Monkhorst-Pack grid densities were chosen to converge total energy differences of $\mathrm{d}E_{tot}/\mathrm{d}E_{cut} <$ 0.001 eV atom^{-1} giving values of E_{cut} = 500 eV for both TCF and TCG and a Monkhorst-Pack grid of 3 × 3 × 4. Standard convergence criteria were applied for geometry optimisation: maximum change in total energy of 2.0 × 10^{-5} eV atom^{-1}, maximum force 0.05 eV Å^{-1}, maximum root-mean-square atomic displacement of 0.002 Å, and maximum stress of 0.1 GPa. Experimentally-derived structures provided starting

coordinates for optimisation of atomic positions and unit-cell dimensions.

5.4 Results and Analysis

5.4.1 Calorimetry and variable-temperature powder diffraction

Differential scanning calorimetry identified a total of three phase transitions in TCG and five phase transitions in TCF. Of the five TCF phases, three were structurally closely related to, but not precisely isostructural with the equivalent TCG phases (see Table 5.3.1), so the phase sequence of TCF can be considered to be analogous to TCG with two additional intermediate phases. To avoid labelling phases out of sequence or with absent members, phases are labelled using the Pearson symbol which identifies similar phases in the respective sequences. The general phase sequence found in these compounds on heating is given below; the additional intermediate phases observed in TCF are shown in square brackets.

$$o\mathit{P}88\ (\mathit{Pbma}) \rightarrow [o\mathit{P}44\ (\mathit{Pbm2})] \rightarrow m\mathit{P}22\ (\mathit{Pm}) \rightarrow [m\mathit{P}44\ (P2_1/m)] \rightarrow c\mathit{P}22\ (Pm\bar{3}m) \rightarrow \text{amorphous}$$

Differential scanning calorimetry measurements for TCG (shown in Figure 5.4.1(a)) show the presence of three first-order transitions peaking at 286.15, 391.04, and 393.58 K. Single-crystal X-ray diffraction data were collected at 180, 300, and 393 K to identify the three TCG phases.

The DSC data for TCF, shown in Figure 5.4.1(b), indicated a total of five transitions on heating a freshly prepared sample between 100 K and 400 K. This is in agreement with Kosturek *et al.* (1999) for a sample taken from room temperature into phase TCF-$oP88$ then heated. The critical temperatures for phase transitions in both materials are given in Table 5.4.1 along with literature values. The variable-temperature single-crystal diffraction data collection strategy followed the phase sequence from 220 K to 385 K on freshly prepared samples cooled from room temperature. All structures, with the exception of TCF-o$P44$, are previously unreported.

The narrow stability range of the $cP22$ phases on heating (TCG: 2.54 K; TCF: 2.00 K) in both materials results in overlapping peaks in the DSC data between the

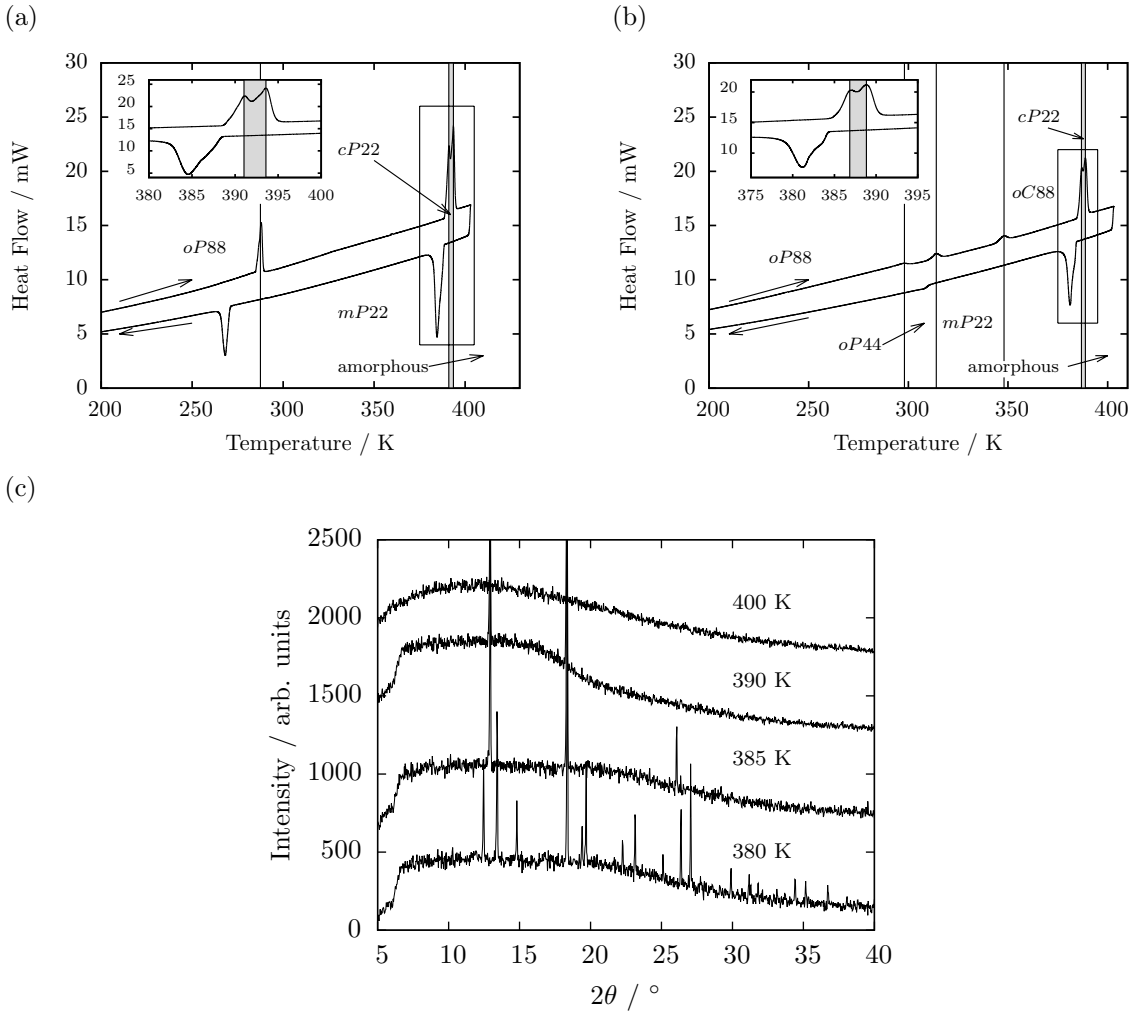

Figure 5.4.1: DSC data for (a) TCG, three phase transitions are apparent on heating at 286.15, 391.04 and 393.58 K; (b) DSC Data for a single crystal of TCF. The five phase transitions upon heating are marked with vertical lines. Insets display the two transitions in the region of the high-temperature *cP*22 phase (shaded); (c) Variable temperature X-ray powder diffraction data over the stability range of TCF-*cP*22 phase. The data at 380 K correspond to the *mP*44 monoclinic phase. By 385 K only three peaks are discernible in the diffraction pattern and can be indexed with a primitive cubic cell. At 390 K the diffraction limit has dropped significantly with just two reflections and by 400 K the sample is amorphous showing only diffuse scattering.

Transitions (TCF)	Critical temperature from DSC / K	Kosturek *et al.* (1999)	Ruiz-Larrea *et al.* (1987)
$oP88 \rightarrow oP44$	288.2	288	291
$oP44 \rightarrow mP22$	310.9	307	307
$mP22 \rightarrow mP44$	344.4	341	347
$mP44 \rightarrow cP22$	386.84	386	381
$cP22 \rightarrow$amorphous	388.84		
Transitions (TCG)	Critical temperature from DSC / K		
$oP88 \rightarrow mP22$	286.15		
$mP22 \rightarrow cP22$	391.04		
$cP22 \rightarrow$amorphous	393.58		

Table 5.4.1: Phase transitions in TCF according to literature and DSC measurements on heating.

$mP22 \rightarrow cP22$ and $cP22 \rightarrow$amorphous transitions (*cf.* Figure 5.4.1 insets).

Variable-temperature powder diffraction for TCF shows the presence of a cubic phase stable in the narrow range of 385 K to 390 K before the sample became amorphous (Figure 5.4.1(c)). Shoulders are also visible on the corresponding DSC peaks upon cooling, although they are less well defined for both materials. It is also noteworthy that there is no peak upon cooling corresponding to the $mP22 \rightarrow mP44$ transition for TCF on cooling.

5.4.2 Phase sequence and structures

Phase transitions in TCF and TCG are characterised by reorientations of the constituent $[NMe_4]^+$ and $[MCl_4]^-$ ions, and can be visualised in terms of alignment of 'chains' formed by both ions along the crystallographic axes. The highest temperature cubic phase ($cP22$) is the exception, with both ions rotationally disordered.

At temperatures below 288 K (TCF) and 286 K (TCG) both materials crystallise in the $oP88$ phase, which has space group $Pbma$ with unit-cell dimensions: (TCF at 220 K) $a = 13.1442(8)$, $b = 13.9946(8)$, and $c = 6.4272(3)$ Å, $Z = 4$. $Pbma$ is a non-standard setting of $Pbcm$, and is used here to facilitate comparisons with the other phases.

As illustrated in Figure 5.4.2, the ions in this phase are aligned along the c-axis in 'chains' of matching orientation. Successive chains along **a** and **b** contain $[MCl_4]^-$ anions oriented 'up' or 'down' along **c** as a result of the inversion symmetry. The

major structural changes between phases (excluding $cP22$) can be understood in terms rotations of $[MCl_4]^-$ anions about the **b** axis in the *ac*-plane, therefore each phase can be characterised by the orientation of $[MCl_4]^-$ anions along **b**. In TCF-$oP88$ the $[FeCl_4]^-$ anions are mutually perpendicular, with small off-sets in the *ac*-plane.

The corresponding TCG-$oP88$ structure is similar, except that the off-sets of $[GaCl_4]^-$ anions in the *ac*-plane are much larger than in TCF-$oP88$. In TCG-$oP88$, $[GaCl_4]^-$ anions are offset along **c** creating sinusoidal chains in the *a*-direction with amplitude 1.077(2) Å at 226 K, compared to 0.006(1) Å in TCF at 220 K (*c.f.* Figure 5.4.2(a) and (b)). This difference in packing allows TCG-$oP88$ to adopt a signifcantly smaller volume than TCF-$oP88$, despite the only marginally larger $[FeCl_4]^-$ ion. The tetrahedral volume of $[GaCl_4]^-$ at 226 K is 5.185(7) Å^3, the volume of $[FeCl_4]^-$ is 5.352(4) Å^3 at 220 K. Differences between $oP88$ phases are discussed further below (§5.4.4).

Upon heating through the $oP88 \rightarrow oP44$ phase transition to 295 K, TCF adopts an orthorhombic cell, space group $Pbm2$ with unit-cell dimensions $a = 6.4471(5)$, $b = 14.2753(11)$, and $c = 6.4526(5)$ Å, $Z = 2$. This structure corresponds to the corrected room-temperature structure described (in the standard $Pma2$ setting) by Wyrzykowski *et al.* (2008). The loss of *a*-glide symmetry leads to a halving of the *a*-axis relative to TCF-$oP88$: for TCF-$oP44$ $a' \approx a/2$, $b' \approx b$, $c' \approx c$, with **c** becoming a polar axis. This can be considered as a result of further alignment of the ionic chains along the *a*-axis, alternation now occurs along **b** only, as illustrated by comparison of Figure 5.4.2(a) and Figure 5.4.3. In this phase all Fe-Cl3 bonds are aligned along **c,** leading to partial eclipsing along **b** rather than alternating in the positive and negative directions (*c.f.* top-right projections in Figure 5.4.2(a) and Figure 5.4.3).

There is no direct group-subgroup relationship for phases $oP88$ and $oP44$. Despite the reduced point group symmetry, $oP44$ is not a *translationengeleiche* maximal subgroup of $oP88$ as the unit cell volume decreases through the transition (Müller, 2013). The lack of a direct group-subgroup relationship is typical for a first-order crystalline phase transition and suggests the presence of a hypothetical arisotype structure which is both a *translationengeleiche* maximal supergroup of $oP44$ and a *klassengeleiche* maximal supergroup of $oP88$. The only space group to satisfy these conditions is a hypothetical structure in $Pmam$ (in full: $P21/m\,2/a\,2/m$, non-standard $a - cb$ setting

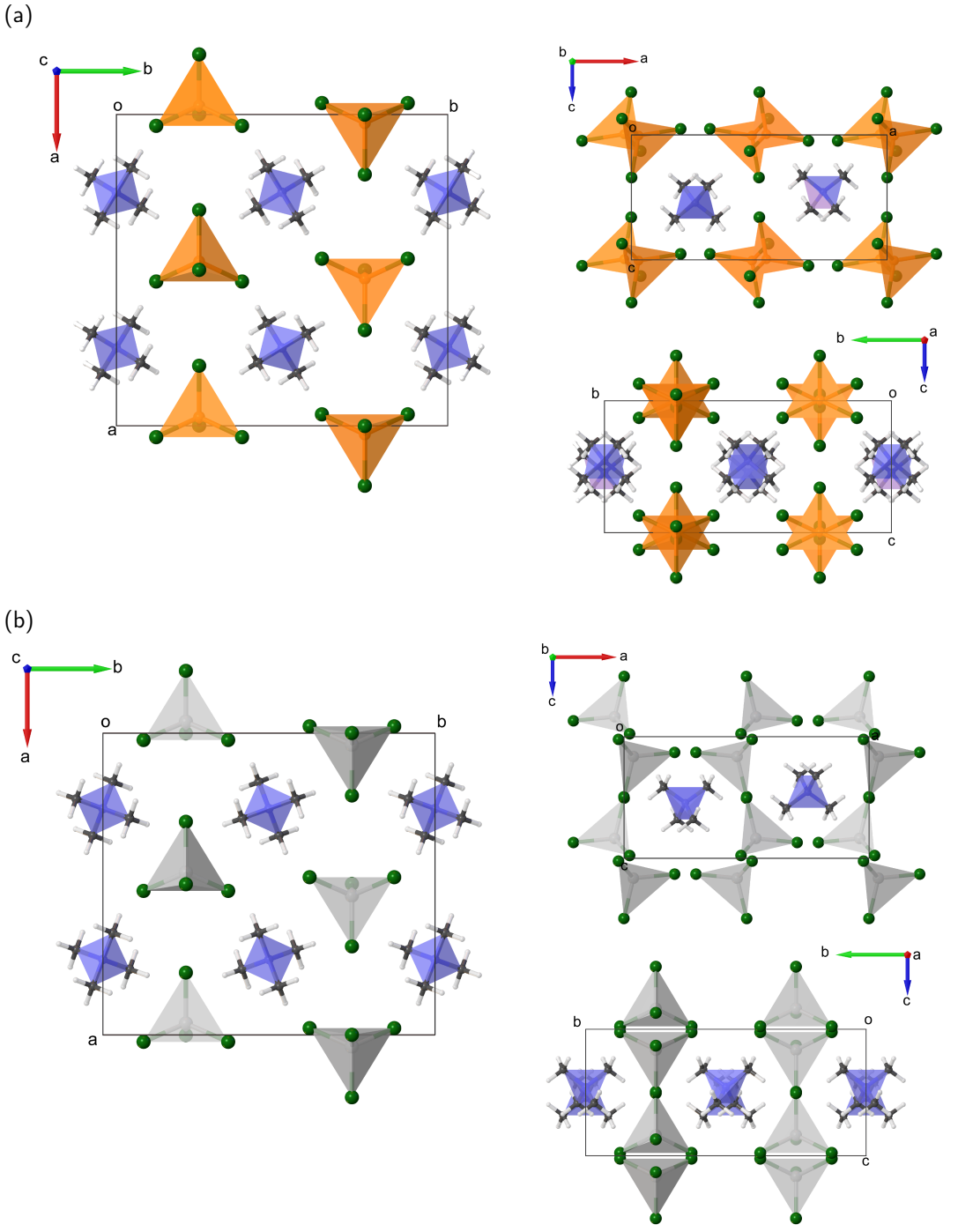

Figure 5.4.2: (a) TCF-*oP*88 illustrating the alteration of ion chain alignment in **b** and **c** directions; (b) shows the similar structure of TCG-*oP*88, highlighting the staggering of $[GaCl_4]^-$ anions in the *ac*-plane.

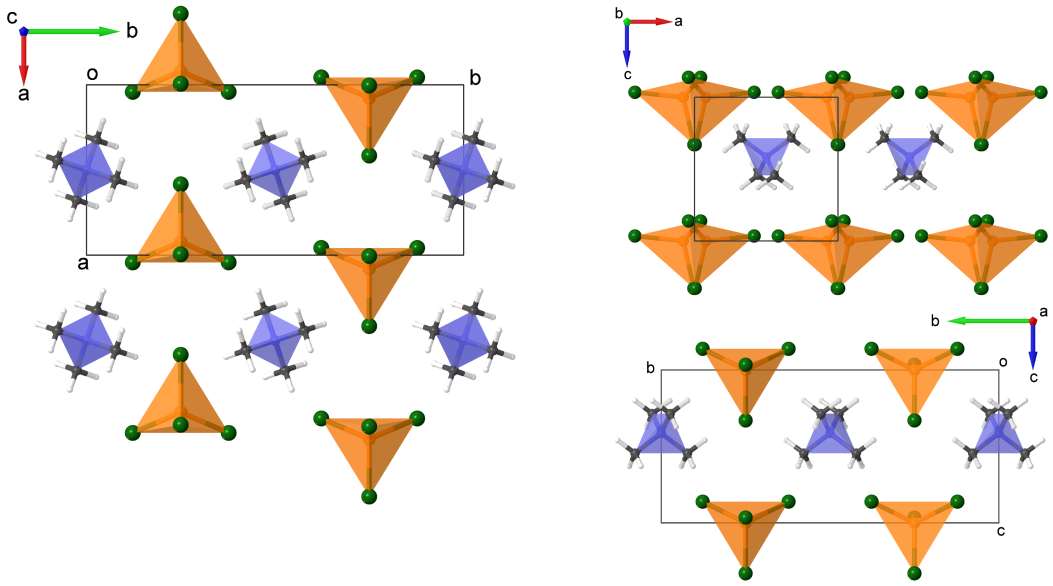

Figure 5.4.3: TCF-*oP*44 shows alteration of ion chain alignment in the *b*-direction; in the *c*-direction ions are now aligned.

of *Pmma*) with unit cell lengths (compared to *oP*88) of $a' \approx a/2$, $b' \approx b$, $c' \approx c$, formed by the overlap of inversion-related *oP*44 structures. As described in Müller (2013), this supergroup phase is *not* proposed to exist during the transition, instead phase transformation occurs *via* the nucleation and growth of the incipient phase with transformation occurring at the grain boundaries between the existing and incipient phases.

The structure of TCF-*mP*22 phase was determined at 318 K. Accompanying the transition is a marked drop in the data quality caused by twinning (see §5.3.2). The structure has a primitive monoclinic cell with unit-cell dimensions: $a = 6.425(3)$, $b = 7.1480(16)$, $c = 6.4274(18)$ Å, $\beta = 91.21(3)°$, space-group symmetry Pm, though this can be transformed to an orthorhombic C-centred setting with dimensions $a = 8.9739(19)$, $b = 9.204(2)$, and $c = 7.1747(12)$ Å. These parameters are similar to those reported for the highly disordered structure of tetramethylammonium tetrachlorothallate(III) reported by Lenck *et al.* (1991) ($a = 7.525(3)$, $b = 8.946(4)$, $c = 9.132(4)$ Å) and it seems possible that that structure too is actually monoclinic and twinned by pseudo-merohedry.

It is usually the case that symmetry increases through a sequence of phase transitions induced by heating, and it is noteworthy that the point-group symmetry decreases for

both TCF and TCG upon heating in the sequence $mmm \rightarrow [mm2] \rightarrow m$. The expected increase in symmetry is seen in the lattice translations. The phase transition from TCF-$oP44$ to TCF-$mP22$ leads to a halving of the b-axis length, so that with respect to TCF-$oP88$, in TCF-$mP22$ $a' \approx a/2$, $b' \approx b/2$, $c' \approx c$. The loss of all glide symmetry results in the full alignment of all the ionic chains along the axes as shown in Figure 5.4.4(a), as a result the $[FeCl_4]^-$ anions are fully eclipsed, resulting in the shortest Cl3...Cl3 contacts along **b** (3.544(6) Å).

A similar TCG-$mP22$ phase is observed above 286 K. As mentioned above, the two domains were related by a rotation of 90° about the b-axis with unit-cell dimensions at 300 K: $a = 6.4478(14)$, $b = 7.1316(7)$, and $c = 6.4451(8)$ Å, $\beta = 91.399(14)°$. Of the various twinning possibilities only the four-fold axis about **b** was active, this difference may be due to the quality of fit at the domain walls of each material.

Calorimetry measurements suggested TCF-$mP22$ to be stable over a 30 K range before a third transition at 344 K formed the TCF-$mP44$ phase; diffraction data on this phase were collected at 365 K. At this temperature the crystal quality had degraded still further and appeared to consist of at least four domains and smaller fragments with no significant diffracted intensity beyond 1.0 Å. A second sample crystal was selected and reflections were indexed to a primitive monoclinic cell, $a = 6.574(3)$, $b = 14.156(7)$, $c = 6.594(3)$ Å, $\beta = 93.86(4)°$ with space-group symmetry $P2_1/m$.

Numerous partially-occupied C atom sites were located about the central N atom of the $[NMe_4]^+$ cation giving an approximately spherical distribution about N. This shell of C atoms was modelled using a spherical shell equivalent to four methyl groups.

Interionic distances increase as a result of the $[NMe_4]^+$ motion and anionic rearrangement; $FeCl_4$-$FeCl_4$ distances (given by the unit-cell lengths) increase by 0.125(4) Å relative to TCF-$mP22$, and 0.149(5) and 0.139(4) Å relative to the similar TCF-$oP44$ structure. The increased symmetry of the $[NMe_4]^+$ cations results in the loss of the b-glide perpendicular to **a**.

In TCF-$mP44$, $[FeCl_4]^-$ alignment alternates along the b-axis only, ions are fully aligned along **a** and **c**. The eclipsed configuration along **b** adopted in TCF-$mP22$ is replaced by a fully staggered conformation, relieving the short, head-on Cl3...Cl3 contacts present in TCF-$mP22$, increasing from 3.544(6) Å to 3.628(11) Å (*cf.* top-right

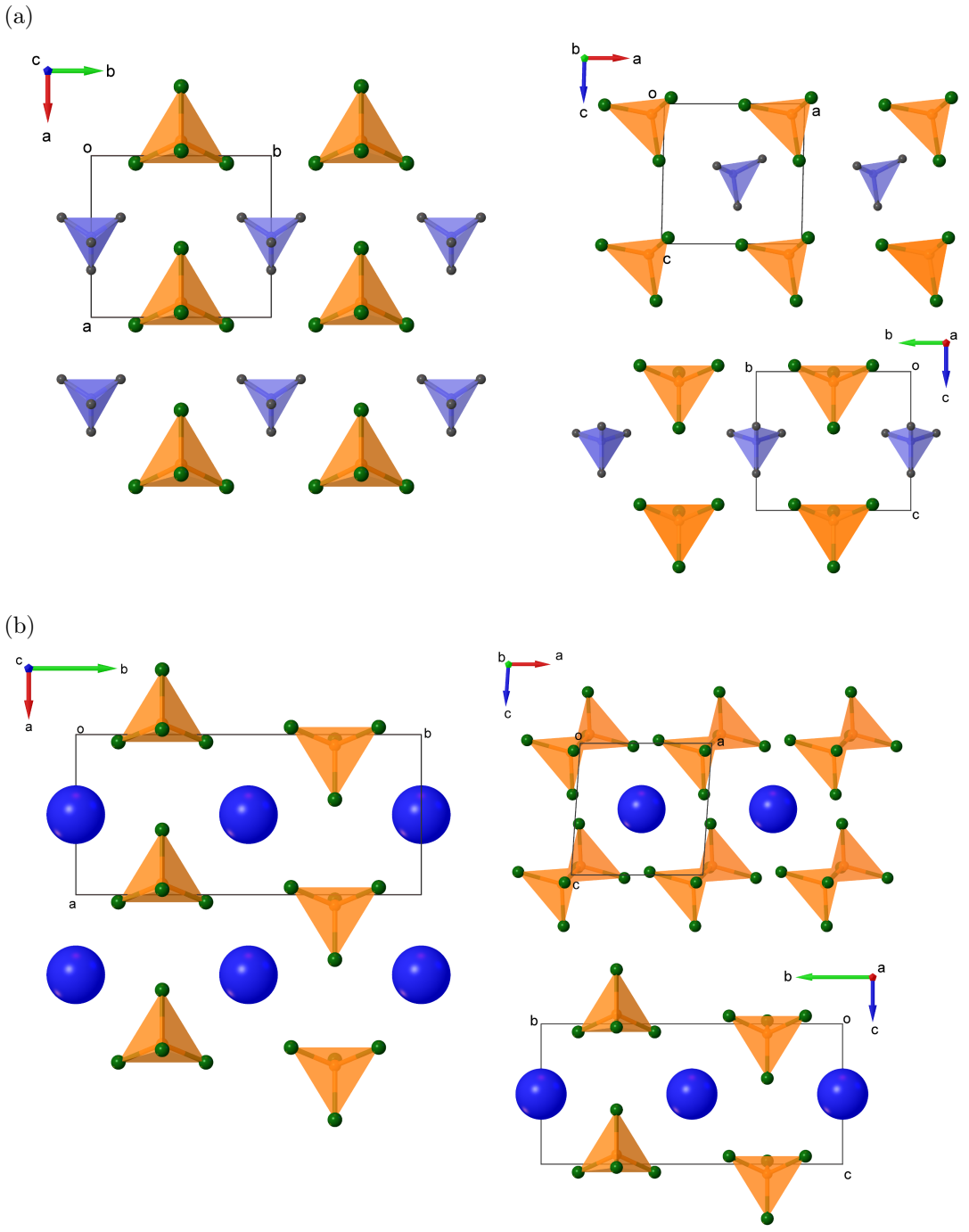

Figure 5.4.4: (a) Projections of TCF-*mP*22. All ion chains are aligned with only mirror symmetry present perpendicular to **b**; (b) TCF-*mP*44, the arrangement of $[FeCl_4]^-$ anions is similar to TCF-*oP*44, however the $[NMe_4]^+$ cations are rotationally disordered increasing the symmetry from $Pbm2$ to $P2_1/m$.

insets in Figure 5.4.4).

5.4.3 Prototype plastic phase

Heating TCF through the final phase transition to 385 K produces the expected high-symmetry prototype phase ($cP22$), indexed with a primitive cubic cell with $a = 6.8460(3)$ Å. The diffraction limit dropped to approximately 2 Åand highly structured diffuse scattering, taking the form of sheets in the {100} planes, could be observed, in addition to a diffuse inner ring as shown in Figure 5.4.5(a). These features are characteristic of a plastic (or rotor) crystalline phase. Such phases exhibit rotational disorder of the constituent ions and are often associated, in ionic materials, with sharp increases in dielectric constant such as those observed by (Czapla *et al.*, 1985; Staveley, 1962). Heating TCG through the phase transition to 393 K results in a similar significant drop in diffraction resolution to approximately 1.5 Å, also accompanied by sheets of diffuse scattering in the {100} planes. At 393 K, the TCG unit cell could be indexed to a slightly larger primitive cubic cell, $a = 6.8504(4)$ Å.

Both structures were refined in $Pm\bar{3}m$ with the tetramethylammonium cation occupying the body center, tetrachlorometallate at the origin. Both ions lie on Wyckoff positions with octahedral point symmetry $m\bar{3}m$ (O_h) which, in conjunction with the diffuse scattering, confirms rotational disorder at both sites. One chlorine atom sits on Wyckoff position $24m$ at (x, x, z) with occupancy 0.125, the remaining chlorine position is the higher symmetry $8g$ position at (x, x, x) with an occupancy of 0.125. The off-axis position of the m chlorine produces a truncated dodecahedron representing eight orientations of the $[MCl_4]^-$ anion.

For each tetrahedral anion orientation, one chlorine atom occupies the $8g$ site and the remaining three occupy the $24m$ site. The $24m$ chlorine sites create short Cl...Cl contacts of 2.52(2) Å along the cell edges. For an Fe−Cl bond length of ∼2.20 Å and a chlorine van der Waals radius of 1.74 Å, the radius of a freely-rotating $[FeCl_4]^-$ anion would be ∼3.94 Å, requiring a primitive unit cell with $a > 7.9$ Å, and a volume 1.5 times larger than the measured volume. As for the plastic crystal phase of CBr_4, (another material with molecules of T_d symmetry occupying sites with O_h symmetry) the structured nature of the $[MCl_4]^-$ reflects the hindered nature of rotation at these

sites requiring strong nearest-neighbour-correlated motion (Folmer *et al.*, 2008).

The $[NMe_4]^+$ cation was refined using a spherical special shape in *CRYSTALS*. A similar treatment was also attempted for $[MCl_4]^-$ however this gave significantly worse fitting than the discrete-disorder model. The final model is shown in Figure 5.4.5(b) along with an F_{obs} isosurface plot indicating the discrete disorder of the $[FeCl_4]^-$ anion (Figure 5.4.5(c)).

To summarise, the structures of each phase of TCF and TCG corresponding to the observed transitions from DSC measurements have been determined by single-crystal X-ray diffraction. Tables 5.5.1 and 5.5.2 summarise the crystallographic data for phases of TCF and TCG.

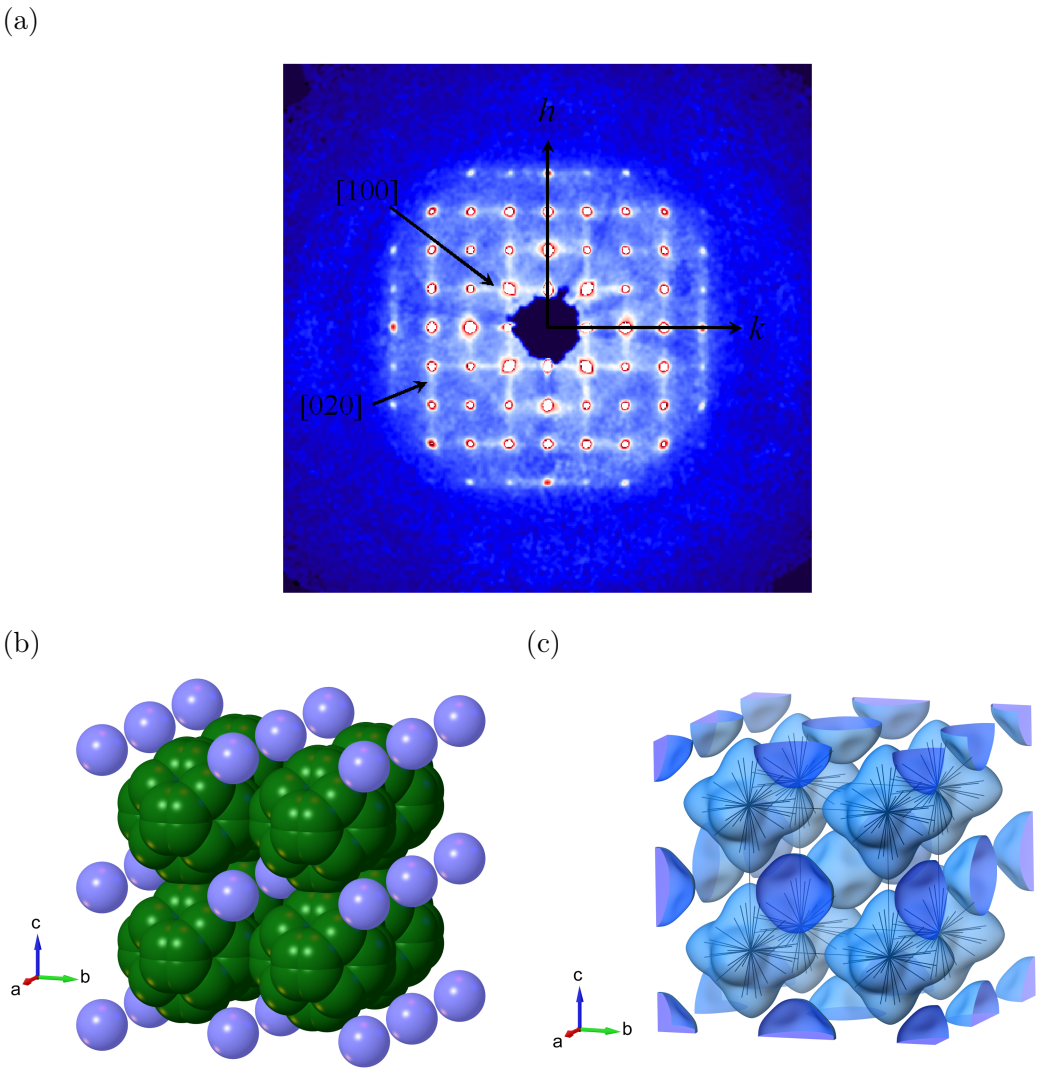

Figure 5.4.5: TCF-*cP*22 (a) A simulated procession image of the $hk0$ plane showing the sheets of diffuse scattering; (b) The spherical shape of the $[NMe_4]^+$ cation is indicative of full rotational disorder on that site. The $[FeCl_4]^-$ anion however appears more constrained occupying one of eight possible orientations. Short Cl...Cl distances are present along each axis; (c) An F_{obs} isosurface map illustrating the discrete orientations of the $[FeCl_4]^-$ anions. Isosurface level is 0.5 e Å^{-3}, plot generated using *VESTA 3* (Momma and Izumi, 2011).

5.4.4 Thermal expansion and packing in *oP*88 phases

The more efficient packing displayed by TCG-*oP*88 results in smaller unit-cell volumes than TCF-*oP*88 throughout the temperature range studied. This is despite the significantly larger bulk thermal expansivity for TCG-*oP*88 over TCF-*oP*88: $\alpha_{V,\mathrm{Ga}} = 40(3) \times 10^{-5}$ K^{-1} and $\alpha_{V,\mathrm{Fe}} = 19(2) \times 10^{-5}$ K^{-1}. The unit-cell volume difference increases to a maximum of ~ 27 Å^3 at 150 K, before decreasing to a minimum of ~ 20 Å^3 at 285 K (Figure 5.4.6(a)).

Examining axial thermal expansivities for TCF reveals the origin of the low bulk expansivitiy; the **a** and **b** axes have approximately equal but opposite axial expansivities: $\alpha_{a,\mathrm{Fe}} = -12(2) \times 10^{-5}$ K^{-1}, and $\alpha_{b,\mathrm{Fe}} = 10.4(19) \times 10^{-5}$ K^{-1}. As a result TCF-*oP*88 expands essentially uniaxially along **c** with $\alpha_{c,\mathrm{Fe}} = 21.6(16) \times 10^{-5}$ K^{-1} being approximately equal to $\alpha_{V,\mathrm{Fe}}$. Unit-cell dimensions for both *oP*88 phases are given in Figure 5.4.6(a), expansivities are given in Table 5.4.2.

The primary cause appears to be the increased displacement of $[FeCl_4]^-$ chains along **c**, in a similar fashion to the sinusoidal chains of TCG-*oP*88. From 120 K to 260 K $[FeCl_4]^-$ ions displace up to 0.1179(5) Å along **c** and as a result of inversion symmetry this displacement is replicated in the opposite direction. The effect is similar to a 'wine-rack' in the *ac* plane, the two unique next-nearest neighbour interionic distances correspond to the diagonals of the 'wine-rack', the longest diagonal increases by 0.283(1) Å and the shortest decreases by −0.048(1) Å. Although the analogy is not exact, there are no rigid 'struts' linking $[FeCl_4]^-$, the geometric behaviour can be visualised in a similar manner (Figure 5.4.6(b)).

	TCF-*oP*88	TCG-*oP*88
α_V / $\times 10^{-5}$ K^{-1}	19(2)	40(3)
α_a / $\times 10^{-5}$ K^{-1}	−12(2)	0.9(2)
α_b / $\times 10^{-5}$ K^{-1}	10.4(19)	11.2(8)
α_c / $\times 10^{-5}$ K^{-1}	21.6(16)	20.8(20)

Table 5.4.2: Bulk and axial thermal expansivities for *oP*88 phases of TCF and TCG.

In addition to the presence of sinusoidal displacements in the *ac* plane, the structure of TCG-*oP*88 also shows significantly shorter Cl…Cl short contact distances as a result of the more covalent-type bonding present in the $[GaCl_4]^-$ anion. This effect is most noticeable in the Cl…Cl contacts along the **a** and **b** axes, which are shorter in TCG-*oP*88 by −0.358(3) Å and −0.119(2) Å, respectively. These short-contacts are clearly visible in the fingerprint plots of $[MCl_4]^-$ anions shown in (Figure 5.4.6(c)). The shortest Cl…Cl contacts occur along the **b** direction and in TCF the Fe−Cl…Cl angle is 116.99(4)° whereas in TCG this value is 142.59(8)°. This difference leads to the pronounced staggering of ions in the *ac*-plane observed for TCG; this difference is

exaggerated further in the optimised structures of TCG-*oP*88 and TCF-*oP*88 where Fe−Cl...Cl is 114.79° and Ga−Cl...Cl 144.10°.

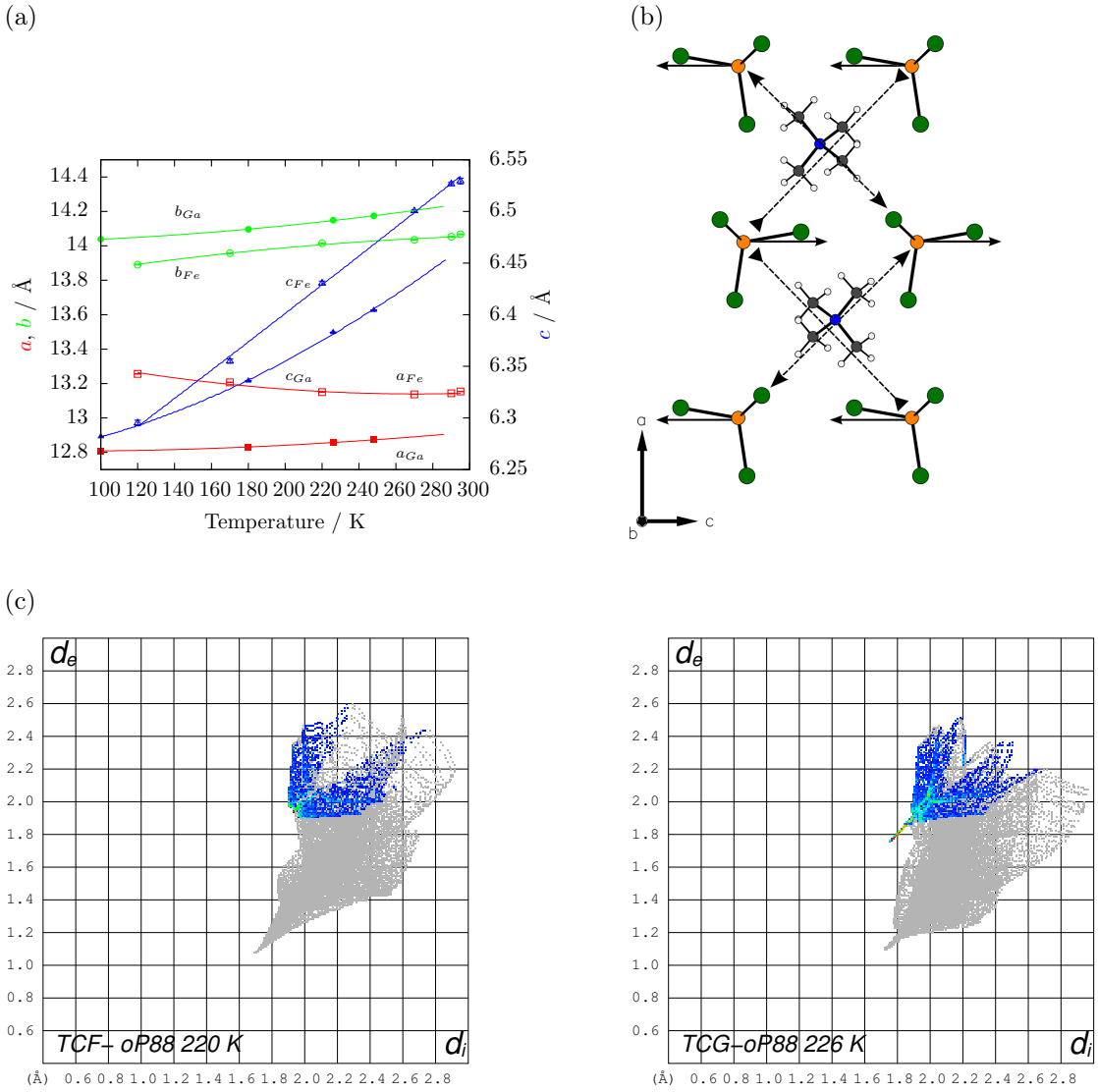

Figure 5.4.6: (a) Changes in unit cell dimensions for *oP*88 phases of TCF and TCG. Berman thermal equation of state values are given by solid lines; (b) Origin of negative thermal expansivity along **a**. Displacements of $[FeCl_4]^-$ ions along **c** has the effect of reducing diagonal distances across the 'wine-rack' arrangement in the ac-plane. Consequentially, aligned ionic chains along **c** can approach closer, reducing **a** with increasing temperature; (c) Fingerprint plots for (left) $[FeCl_4]^-$ at 220 K and (right) $[GaCl_4]^-$ at 226 K. Only Cl...Cl close contacts are highlighted. The sharp 'point' at low d for TCG shows the prevalence of short Cl...Cl contacts in the structure.

5.4.5 Anomalous volume reduction

Examination of the volume per formula unit (V/Z) values gives an indication of the packing efficiencies of the various phases. Data for TCF and TCG derived from variable-

temperature X-ray powder diffraction are shown in Figure 5.4.7(a). The coexistence of TCF-$oP88$ and TCF-$oP44$ in the powder form at 295 K allowed the direct comparisons of V/Z and the transition from $oP88 \rightarrow oP44$ results in a significant reduction in V/Z of $-4.1(4)$ Å^3 (-1.3 %), an example of a discontinuous contraction through a phase transition. Similar data for TCG shows no such reduction in V/Z, with only a minor increase of $+2.0(5)$ Å^3 ($+0.7$ %) and no significant discontinuous changes in unit cell dimensions (Figure 5.4.7(a) and (b)).

Comparison of the unit cell dimensions (with $a' = a/2$ and $b' = b/2$ for $oP88$, $b' = b/2$ for $oP44$) show the decrease to be due to contractions in the a'- and c-axes of $-0.126(2)$ Å (-1.9 %) and $-0.068(3)$ Å (-1.0 %) respectively, counter-acted by an increase along b' of 0.115(4) Å (1.6 %) as shown in Figure 5.4.7(b).

The discontinuous changes in unit cell lengths can be rationalised by examining the packing of $[FeCl_4]^-$ anions. In both phases $[FeCl_4]^-$ are arranged to create buckled layers of Cl atoms in the bc-plane composed of three of the four Cl atoms of each anion. The remaining fourth Cl atom is projected above or below these planes along **a** (Figure 5.4.7(c)). The degree of buckling within these layers determines how efficiently the planes can stack and consequentially determines the magnitude of **a**. On transition from $oP88$ to $oP44$, the buckling in these layers decreases from an amplitude of 0.457 Å to 0.279 Å, in effect the layers are 'flattened' allowing more efficient packing and accounting for the discontinuous reduction in a'.

The smaller reduction in c is due to both ions shifting from positions displaced above and below the c-glide in $oP88$ to lying directly within the glide plane in $oP44$. At 220 K the displacements in $[NMe_4]^+$ position are $\pm 0.278(3)$ Å and remain unchanged up to at least 260 K ($\pm 0.287(5)$ Å). Similar, smaller displacements occur in $[FeCl_4]^-$ position, at 200 K anionic displacements are $\pm 0.0740(3)$ Å increasing to $\pm 0.1960(6)$ Å at 260 K, in TCF-$oP44$ these offsets are absent and ions lie in the directly in their respective planes.

While both TCF-$oP88$ and TCF-$oP44$ phases were present at the 295 K collection, for the other transitions there were no simultaneous mixed phase measurements so a direct comparison of V/Z values is not possible. However, the values at 305 K ($oP88$, 298.7(1) Å^3) and 310 K ($mP22$, 298.7(4) Å^3) are indistinguishable, which combined

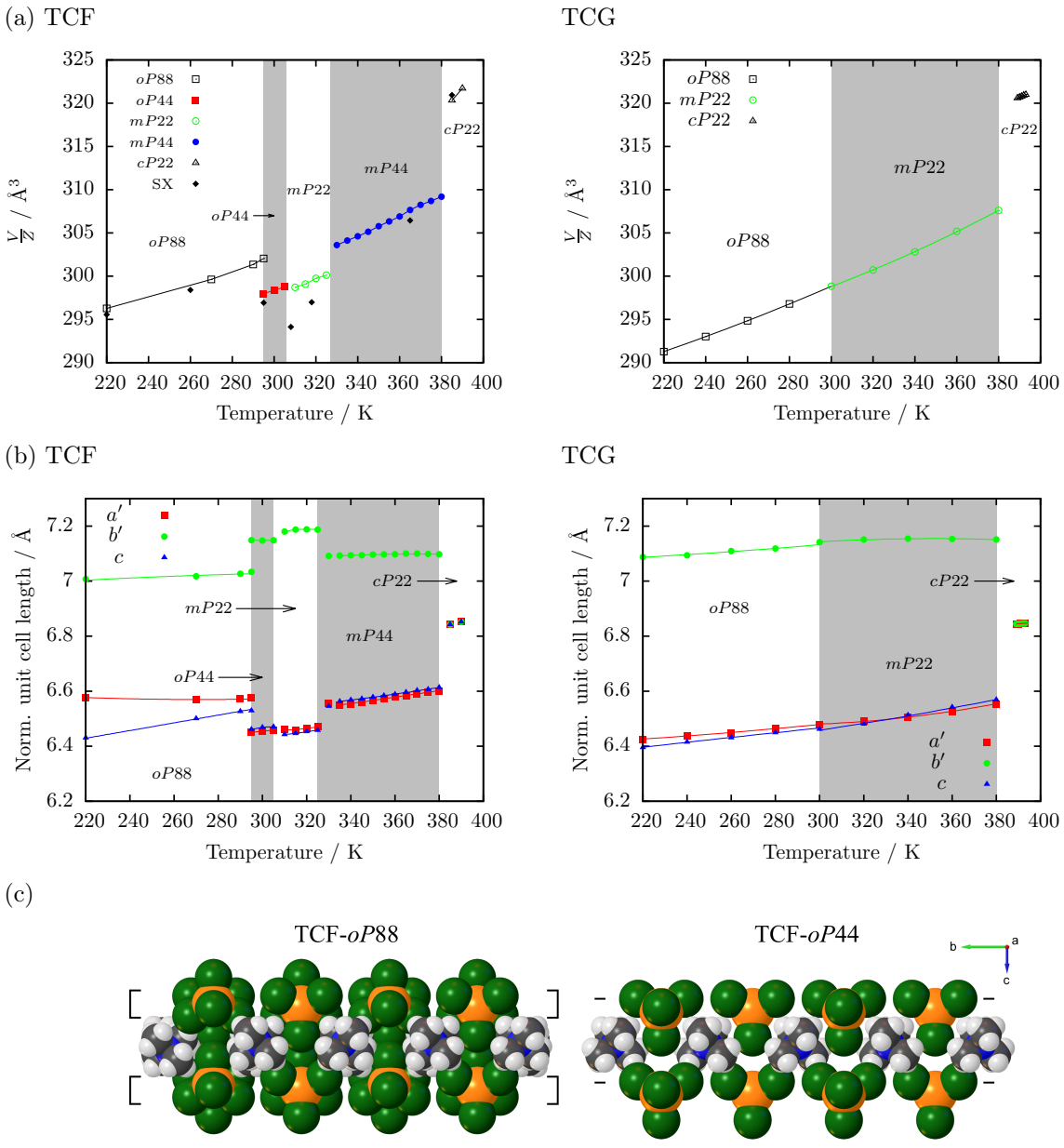

Figure 5.4.7: (a) Changes in volume per formula unit (V/Z) with temperature for (left) TCF and (right) TCG as determined by variable temperature X-ray powder diffraction and single-crystal data, labelled 'SX'; (b) Corresponding changes in normalised unit cell dimensions with temperature. Lines correspond to thermal equation of state values. Errors are smaller than symbols; (c) Space-filling plots of TCF-*oP*88 and TCF-*oP*44, the layers of Cl atoms, indicated with braces, pack more closely along **c** as a result of anionic reorientation.

with the much higher bulk thermal expansivity of phase $oP44$ ($52(5) \times 10^{-5}$ K^{-1}) as compared to phase $mP22$ ($28(7) \times 10^{-5}$ K^{-1}) suggests that $mP22$ offers a lower V/Z around this temperature range.

The $mP22 \rightarrow mP44$ transition is marked by a sharp volume increase of 6.6(1) Å^3 accompanying the onset of rotational disorder in $[NMe_4]^+$ cations. A similar increase of 7.4(1) Å^3 occurs on the final transition to phase $cP22$ where the $[FeCl^4]^-$ anions become rotationally disordered. This sequence is in marked contrast to TCG where during the $mP22 \rightarrow cP22$ transition there is an increase of 13.0(1) Å^3, clearly due to the simultaneous onset of rotation in both ions.

5.4.6 Analysis of phase sequence

Phase sequences for both TCF and TCG are similar with the exception of two additional intermediate phases: TCF-$oP44$ and TCF-$mP44$. Enthalpy changes derived from DSC data (Table 5.4.3) show that the transitions to intermediate phases in TCF require significantly less energy than transitions in TCG. As a result, the total enthalpy changes for transition sequences $Pbma \rightarrow [Pbm2] \rightarrow Pm$ and $Pm \rightarrow [P2_1/m] \rightarrow Pm\bar{3}m$ are significantly lower for TCF. The DSC peaks corresponding to the transitions into and out of the $cP22$ phases ($mP22$ or $mP44 \rightarrow cP22$) overlap; as a result the enthalpy changes recorded by DSC are the sum for the two transitions. The 0.31 kJ mol^{-1} difference between the TCG and TCF sequence reflects the fact that the $[NMe_4]^+$ cations are already rotationally disordered in TCF-$mP44$ before the onset of the $cP22$ phase.

Mulliken population analysis (Mulliken, 1955) of $[GaCl_4]^-$ and $[FeCl_4]^-$ anions in optimised $oP88$ structures shows a significant charge disparity of 0.22 e between $[GaCl_4]^-$ ($-0.56\,e$) and $[FeCl_4]^-$ ($-0.78\,e$) which suggests increased covalency in the $[GaCl_4]^-$ anion. This difference allows for the close approach of Cl atoms observed in the structure of TCG-$oP88$ but which are absent in TCF-$oP88$, and is consistent with the more linear M-Cl$\ldots$Cl contacts in TCG compared to TCF (142.59(8)° *versus* 116.99(4)°) which is suggestive of a more prominent Cl-based σ-hole in TCG.

This model is supported by geometry optimisations of $oP88$ phases, both in the experimentally-determined geometries and with Fe substituted for Ga and *vice versa*. Allowing atomic positions and unit-cell dimensions to optimise results in structures in

which the initial anionic arrangements are essentially preserved, and the resulting total energy differences reflect the stable arrangements observed experimentally.

When Fe is substituted for Ga in the structure of TCG-$oP88$, the final configuration results in short Cl...Cl distances of 3.5176 Å along **b**, significantly shorter than in the arrangement in TCF-$oP88$: 3.8845 Å (−0.3669 Å, −9.45 %) and as a result the total energy of this conformation is 9.12 kJ mol^{-1} higher in energy. Similarly for TCG, the optimised experimental configuration is significantly lower in energy than the Ga-substituted TCF-$oP88$ structure, the total energy difference between the two optimised geometries is 6.73 kJ mol^{-1}.

TCF transitions	Critical temperature DSC / K	ΔH from DSC / kJ mol^{-1}
$oP88 \rightarrow oP44$	288.2	0.4089
$oP44 \rightarrow mP22$	310.9	0.6016
$mP22 \rightarrow mP44$	344.4	0.6183
$mP44 \rightarrow cP22$	386.84	6.0791
$cP22 \rightarrow$amorphous	388.84	
TCG transitions	Critical temperature DSC / K	ΔH from DSC / kJ mol^{-1}
$oP88 \rightarrow mP22$	286.15	2.3455
$mP22 \rightarrow cP22$	391.04	6.3893
$cP22 \rightarrow$amorphous	393.58	

Table 5.4.3: Phase transition enthalpy changes and temperatures for TCF and TCG.

Due to the mismatch in cation-anion sizes all phases of both TCG and TCF can be considered as interpenetrating primitive cubic lattices in the CsCl-type, where each ion has eight neighbours. The T_d point symmetry of each ion results in distortions of the sublattices and offsets with respect to one another, which are resolved only when the effective ionic point symmetry is O_h as in the $cP22$ phases.

At the lowest temperature, the $oP88$ phases show staggering in both cation and anion sublattices. During each phase transition upon heating, translational symmetry is increased by the full occupation of just one orientation of the staggered sublattice. This is illustrated in Figure 5.4.8 for $oP88 \rightarrow oP44$ *via* the hypothetical supergroup $Pmam$, the $[NMe_4]^+$ sublattice is shown in blue, the $[FeCl_4]^-$ sublattice in orange. In $oP88$ the positions of $[NMe_4]^+$ cations are staggered in the ac plane leading to two positions marked 'a' and 'b', in the hypothetical $Pmam$ structure these positions are

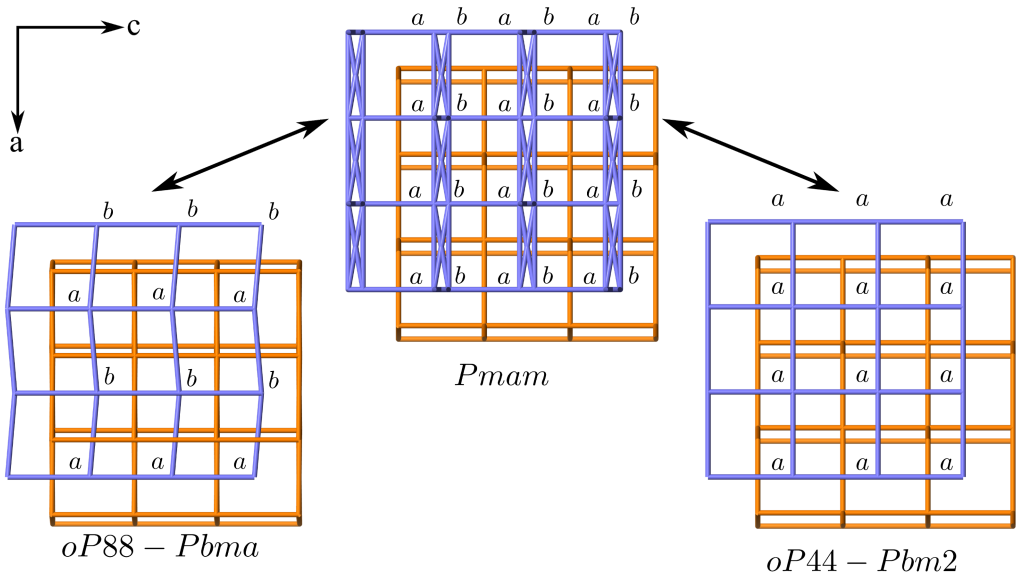

Figure 5.4.8: Phase transition *oP*88→ *oP*44 results in the selection of one $[NMe_4]^+$ ionic orientation which can be visualised by the shared maximal supergroup $Pmam$.

superimposed. Transition to $oP44$ leads to only the 'a' (or the inverse structure 'b') orientations being observed (Figure 5.4.8). Notice that the staggering of $[FeCl_4]^-$ anions in the ab plane is preserved through this transition, this staggering is resolved in the subsequent $oP44 \rightarrow mP22$ transition. The halving of certain unit-cell lengths through the sequence $oP88 \rightarrow oP44 \rightarrow mP22$ implies these transitions are driven by modes occurring away from the gamma point, and will therefore not be IR or Raman active.

5.5 Conclusions

Through a combination of single-crystal and powder X-ray diffraction studies and differential scanning calorimetry, four novel phases of tetramethylammonium tetrachloroferrate (TCF) between 120 and 385 K, and three phases of tetramethylammonium tetrachlorogallate (TCG) between 100 K and 393 K, have been identified. All three phases of TCG display an analogue in the phase sequence of TCF. Unusually, the point group symmetry of both TCG and TCF decreases upon heating until the high-temperature cubic plastic phase, which is stable over a temperature range of just *ca.* 2 K.

The presence of additional intermediate phases suggests greater conformational flexibility of the $[FeCl_4]^-$ anion. The subtle, but energetically significant, structural dif-

ferences in the low temperature $oP88$ phases results in the presence of shorter and more linear M-Cl...Cl contacts in TCG which are absent in TCF. Such close contacts are consistent with the presence of a prominent lone-pair-σ-hole interaction in TCG. Calculations show a distinct covalent character to the $[GaCl_4]^-$ anion, in agreement with this observation. Such interactions are highly directional and may act to reduce the conformational flexibility of $[GaCl_4]^-$, explaining the absence of the intermediate phases.

These additional intermediate phases in TCF appear to allow a lower-energy pathway between phases than is possible in TCG. The structure of TCF-$mP44$ shows the onset of rotational disorder of the constituent ions can occur at separate temperatures, in this case separated by 40 K. This structure is not adopted by TCG, and as a result both ions become disordered simultaneously upon the TCG-$mP22$ $\rightarrow$ TCG-$cP22$ transition at 393 K.

	$oP88$	$mP22$	$cP22$
Crystal data			
Formula		$C_4H_{12}N$, $GaCl_4$	
Formula weight		285.68	
Crystal system	Orthorhombic	Monoclinic	Cubic
Space group	$Pbcm$ (bca)	Pm	$Pm\bar{3}m$
a,b,c / $Å$	12.8329(7), 14.1248(4), 6.3718(3)	6.425(3), 7.1480(16), 6.4274(18)	6.8470(5), 6.8470(5), 6.8470(5)
β / °	90	91.21(3)	90
Volume / Å^3	1182.27(11)	295.12(17)	321.00(7)
Z	4	1	1
F_{000}	568	125	202
Crystal size / mm	0.10 x 0.12 x 0.20	0.10 x 0.12 x 0.20	0.05 x 0.10 x 0.12
Data collection			
Temperature / K	226	300	393
Radiation / Å		Mo$K\alpha$ (0.71073)	
θ_{min}, θ_{max} / °	3.2, 24.8	5.4, 26.3	3.0, 15.6
$h_{min} : h_{max}$;	0:14;	−7:8;	0:3;
$k_{min} : k_{max}$;	0:16;	0:8;	0:3;
$l_{min} : l_{max}$	0:7	−8:8	1:5
Total and unique data,	14843, 1032,	1254, 1254,	1506, 30,
R_{int}	0.044	0.033	0.069
Observed data ($I > 2\sigma(I)$)	994	1231	29
Refinement			
N_{ref}, N_{par}	1028, 51	1254, 56	29, 14
R, $wR2$,	0.0464, 0.0941,	0.0425, 0.0995,	0.0951, 0.1549,
S	1.00	0.98	0.99
$\Delta\rho_{min}$, $\Delta\rho_{max}$ / e Å^{-3}	−0.46, 1.13	−0.44, 0.77	−0.36, 0.48

Table 5.5.2: Crystallographic information for TCG phase sequence.

	$oP88$	$oP44$	$mP22$	$mP44$	$cP22$
Crystal data					
Formula			$C_4H_{12}N$, $FeCl_4$		
Formula weight			271.80		
Crystal system	Orthorhombic	Orthorhombic	Monoclinic	Monoclinic	Cubic
Space group	$Pbcm$ (bca)	$Pma2$ ($ba-c$)	Pm	$P2_1/m$	$Pm\bar{3}m$
a,b,c / $Å$	13.1442(8),	6.4471(5),	6.425(3),	6.574(3),	6.8470(5),
	13.9946(8),	14.2753(11),	7.1480(16),	14.156(7),	6.8470(5),
	6.4272(3)	6.4526(5)	6.4274(18)	6.595(3)	6.8470(5)
β / °	90	90	91.21(3)	93.87(4)	90
Volume / Å^3	1182.27(11)	593.86(8)	295.12(17)	612.3(5)	321.00(7)
Z	4	2	1	2	1
F_{000}	548	274	125	202	202
Crystal size / mm	0.05 x 0.08	0.05 x 0.08	0.05 x 0.08	0.05 x 0.05	0.05 x 0.05
	x 0.10	x 0.10	x 0.10	x 0.10	x 0.10
			Data collection		
Temperature / K	220	295	318	365	385
Radiation / Å			Mo$K\alpha$ (0.71073)		
θ_{min}, θ_{max} / °	3.1, 25.7	3.2, 26.4	3.2, 25.5	3.1, 20.9	3.0, 13.4
$h_{min}:h_{max}$;	0:16;	0:8;	−7:7;	−6:6;	0:2;
$k_{min}:k_{max}$;	0:16;	0:17;	0:8;	0:14;	0:3;
$l_{min}:l_{max}$	0:7	−8:8	−7:7	0:6	1:4
Total and unique data,	17459, 1169,	1248, 1248,	1184, 1184,	5173, 675,	1895, 21,
R_{int}	0.043	0.042	0.133	0.065	0.059
Observed data ($I > 2\sigma(I)$)	1007	1160	1040	576	18
			Refinement		
N_{ref}, N_{par}	1162, 51	1243, 52	1182, 58	665, 32	18, 14
R, $wR2$,	0.0391, 0.0740,	0.0581, 0.1301,	0.0711, 0.1864,	0.1190, 0.2057,	0.0981, 0.1380,
S	1.00	0.96	0.94	1.04	0.99
$\Delta\rho_{min}$, $\Delta\rho_{max}$ / e Å^{-3}	−0.50, 0.41	−0.78, 1.14	−0.68, 0.82	−0.62, 0.59	−0.25, 0.18

Table 5.5.1: Crystallographic information for TCF phase sequence.

5.6 References

Agilent 2014 '*ABSPACK*; *CrysAlis* PRO; *SCALE*'.

Altomare A, Cascarano G, Giacovazzo C and Guagliardi A 1993 *Journal of Applied Crystallography* **26**(3), 343–350.

Angel R J, Alvaro M and Gonzalez-Platas J 2014 *Zeitschrift für Kristallographie-Crystalline Materials* **229**(5), 405–419.

Barreda-Argüeso J A, Nataf L, Rodríguez-Lazcano Y, Aguado F, González J, Valiente R, Rodríguez F, Wilhelm H and Jephcoat A P 2014 *Inorganic Chemistry* **53**(19), 10708–10715.

Berman R 1988 *Journal of Petrology* **29**(2), 445–522.

Betteridge P W, Carruthers J R, Cooper R I, Prout K and Watkin D J 2003 *Journal of Applied Crystallography* **36**(6), 1487.

Clark S J, Segall M D, Pickard C J, Hasnip P J, Probert M I, Refson K and Payne M C 2005 *Zeitschrift für Kristallographie* **220**(5/6/2005), 567–570.

Clay R, Murray-Rust J and Murray-Rust P 1975 *Acta Crystallographica Section B* **31**(1), 289–290.

Czapla Z, Czupiński O, Galewski Z, Sobczyk L and Waśkowska A 1985 *Solid State Communications* **56**(8), 741 – 742.

Flack H D 1987 *Acta Crystallographica Section A* **43**(4), 564–568.

Folmer J C W, Withers R L, Welberry T R and Martin J D 2008 *Phys. Rev. B* **77**, 144205.

Gośniowska M, Ciunik Z, Bator G, Jakubas R and Baran J 2000 *Journal of Molecular Structure* **555**(1), 243–255.

Kandhaswamy M and Srinivasan V 2002 *Bulletin of Materials Science* **25**(1), 41–45.

Kosturek B, Podsiadla D and Czapla Z 1999 *Ferroelectrics* **223**(1-4), 57–61.

Lee M M, Teuscher J, Miyasaka T, Murakami T N and Snaith H J 2012 *Science* **338**(6107), 643–647.

Lenck M, Dou S Q and Weiss A 1991 *Zeitschrift für Naturforschung Section A - a Journal of Physical Sciences* **46**(9), 777–784.

López-Echarri A, Ruiz-Larrea I and Tello M 1990 *Journal of Physics: Condensed Matter*

2(3), 513.

López-Echarri A, Tello M, Socias C and Herreros J 1985 *Journal of Physics C: Solid State Physics* **18**(13), 2631.

Lutz M, Huang Y, Moret M E and Klein Gebbink R J M 2014 *Acta Crystallographica Section C* **70**(5), 470–476.

Mahoui A, Lapasset J, Moret J and Saint Grégoire P 1996 *Acta Crystallographica Section C* **52**(11), 2671–2674.

Momma K and Izumi F 2011 *Journal of Applied Crystallography* **44**(6), 1272–1276.

Morosin B and Lingafelter E C 1959 *Acta Crystallographica* **12**(8), 611–612.

Morosin B and Lingafelter E C 1961 *The Journal of Physical Chemistry* **65**(1), 50–51.

Müller U 2013 *Symmetry relationships between crystal structures: applications of crystallographic group theory in crystal chemistry* Oxford University Press.

Mulliken R S 1955 *The Journal of Chemical Physics* **23**(10), 1833–1840.

Muralt P, Kind R, Blinc R and Zeks B 1982 *Phys. Rev. Lett.* **49**, 1019–1022.

Palatinus L and Chapuis G 2007 *Journal of Applied Crystallography* **40**(4), 786–790.

Perdew J P, Burke K and Ernzerhof M 1996 *Phys. Rev. Lett.* **77**, 3865–3868.

Petříček V, Dušek M and Palatinus L 2014 *Zeitschrift für Kristallographie-Crystalline Materials* **229**(5), 345–352.

Ruiz-Larrea I, Fraile-Rodríguez A, Arnáiz A and López-Echarri A 2000 *Journal of Thermal Analysis and Calorimetry* **61**(2), 503–512.

Ruiz-Larrea I, López-Echarri A and Tello M J 1987 *Solid State Communications* **64**(8), 1099–1101.

Sawada S, Shiroishi Y, Yamamoto A, Takashige M and Matsuo M 1978 *Journal of the Physical Society of Japan* **44**(2), 687–688.

Schlessman J and Litvin D B 1995 *Acta Crystallographica Section A* **51**(6), 947–949.

Schröder L, Watkin D J, Cousson A, Cooper R I and Paulus W 2004 *Journal of Applied Crystallography* **37**(4), 545–550.

Sheldrick G M 2015 *Acta Crystallographica Section C* **71**(1), 3–8.

Shimizu H, Kokubo N, Yasuda N and Fujimoto S 1980 *Journal of the Physical Society of Japan* **49**(1), 223–229.

Staveley L A K 1962 *Annual Review of Physical Chemistry* **13**(1), 351–368.

Styczeń E, Pattek-Janczyk A, Gazda M, Jóźwiak W K, Wyrzykowski D and Warnke Z 2008 *Thermochimica Acta* **480**(1), 30–34.

Tkatchenko A and Scheffler M 2009 *Phys. Rev. Lett.* **102**, 073005.

Wolthuis A, Huiskamp W, de Jongh L and Carlin R 1986 *Physica B+C* **142**(3), 301 – 319.

Wyrzykowski D, Kruszyński R, Kłak J, Mroziński J and Warnke Z 2008 *Inorganica Chimica Acta* **361**(1), 262–268.

Zubillaga J, López-Echarri A and Tello M 1988 *Journal of Physics C: Solid State Physics* **21**(24), 4417.

Chapter 6

Concluding remarks

6.1 Summary

The main aim of this work has been to develop the capacity for high-pressure single-crystal neutron diffraction experiments on the KOALA diffractometer, and the successful initial experiments with hexamine and arginine dihydrate demonstrate that this technique is viable and ready to be applied to problems of scientific interest. In addition to development work on KOALA, a number of crystallographic studies utilising high-pressure and variable-temperature X-ray diffraction have been carried out on a wide range of materials as discussed in subsequent chapters.

In Chapter 2, the first high-pressure neutron diffraction study in a miniature diamond-anvil cell of a single crystal of size typical for X-ray diffraction were reported. Unexpectedly reflections whose diffracted beams pass through the cell body are reliably observed, and can be used for structure refinement after correcting for attenuation. There is no angular limit imposed by the cell and the crystallographic completeness for a sample in the cell is essentially the same as a data collection without the cell. Initial experiments with hexamine showed that sample size and temperature are the most important factors influencing data quality. Despite the small crystal size and correction for attenuation, the data collected allow a full anisotropic refinement of hexamine with bond lengths and angles that agree with literature data within experimental error. Further experiments with arginine dihydrate showed the suitability of this technique for low-symmetry crystals, and in these cases the transmission of diffracted beams through the cell body results in much higher completeness values than are possible with X-rays.

In the following chapter a combination of high-pressure X-ray diffraction and neutron Laue diffraction were used to investigate the pressure- and temperature-dependent phase transitions in the ferroelectric rubidium hydrogen sulfate. Neutron diffraction above and below the ferroelectric transition agreed with spectroscopic data in the literature, confirming the mechanism giving rise to the spontaneous polarisation in the ferroelectric phase is due to the ordering of hydrogensulfate anions. Under applied pressure $RbHSO_4$ undergoes a ferroelectric transition before a transition to a third high-pressure phase described in the literature as another non-centrosymmetric structure, our data show this structure is in fact centrosymmetric and is isostructural to an ambient pressure phase

of $CsHSO_4$. This chapter also described the difficulties encountered attempting high-pressure (and high-temperature) neutron diffraction data on KOALA and subsequent developments, including testing of gasket materials and the collection of orientation matrices prior to the experiment using X-ray diffraction.

Chapter 4 investigated the mechanical behaviour of the cobalt citrate metal-organic framework UTSA-16. Three contrasting hydrostatic media were used and the mechanical response was found to be highly dependent upon the medium. Structural analysis showed the array of behaviours to originate in coordination changes at the flexible cobalt tetrahedra. Under pure hydrostatic compression, these tetrahedra flex inducing a negative linear compressibility effect. In methanol, the filling of the pores and ordering potassium cations suppresses this motion resulting in positive axial compressibilities. In isopropyl alcohol a pressure-driven transition increases cobalt coordination numbers replacing cobalt tetrahedra with rigid octahedral units. The resulting reduced compressibility shows that these secondary-building units play a critical role in determining the mechanical strength of this framework material in both penetrating and non-penetrating hydrostatic media.

In the final chapter the phase transition sequences of two members of the alkylammonium tetrachlorometallate family of hybrid organic-inorganic salts were determined for the first time. Unusually, point-group symmetry reduces with increasing temperature until reaching a cubic prototype phase. This prototype phase is present over a narrow temperature range is characterised by significant diffuse scattering due to hindered rotation of the component ions. The presence of additional intermediate phases with Fe^{3+} was rationalised on the basis of density-functional theory calculations.

6.2 Conclusions and future development

The principal aim of this work has been to develop high-pressure techniques for the KOALA diffractometer, and the results presented here illustrate the potential utility of the technique for a range of problems in contemporary science and will allow for further experiments to probe the pressure and sample size limits. The success of the Laue technique in this regard is based on two factors: firstly the transmission of diffracted

beams through the small cell body effectively removes restrictions on completeness familiar to high-pressure X-ray diffraction. This makes the technique ideally suited to the study of low-symmetry crystals. Secondly, the combination of a stable, finely collimated incident beam and image-plate detectors with a very wide dynamic range results in diffraction patterns from which weak sample scattering can be extracted despite the presence of very strong scattering from the anvils. As a result, the size of the sample can be significantly reduced to volumes approaching those encountered for high-pressure X-ray diffraction. This has the benefit of significantly widening the range of materials for which sufficiently sized single crystals can be synthesised.

There are a number of technical improvements that can be envisaged for future experiments; the use of smaller cells, such as the turnbuckle cell designed for high-pressure magnetization measurements (Giriat *et al.*, 2010), could reduce attenuation of the transmitted beams by reducing the total mass of the cell body. The attenuation correction scheme presented in Chapter 2 can be simply modified for any cell with radial symmetry and an updated version has been developed for use with the turnbuckle cell.

Prior experiments with the moissanite-anvil cell (MAC) from the Geophysical Lab (Xu *et al.*, 2002) on VIVALDI have shown these much larger cells can be fitted and used on Laue instruments. Although it appears diffracted intensity cannot pass through the cell body of this cell (McIntyre *et al.*, 2005), the large angular access and ability to reach far higher pressures (*ca.* 50 GPa) could see its widespread use for pressures above 5 GPa, the current estimated pressure limit for the miniature DAC.

Modifications to the collimation on KOALA could also be explored. Currently the finest degree of collimation available is a 1 mm diameter 'snout' placed downstream of the main aperture. Using current cells, this results in the incident beam illuminating portions of the gasket regardless of the centering. As shown in Chapter 3, minimising the degree of scattering from the gasket will not only improve peak-to-background ratios but would also mitigate against incorrect centering based on structured scattering. Finer collimation could result in significantly reduced background levels, although of course this should be weighed against the reduction in flux to the sample. KOALA is already well-equipped to test fine collimation thanks to the highly precise stage motors already in place.

To date, pressure measurement by ruby fluorescence is only possible offline. This poses a problem for variable-temperature high-pressure experiments where thermal expansion or contraction of the cell can lead to significant changes in pressure applied to the sample, this issue is exacerbated by the inability to determine unit-cell dimensions absolutely by the Laue method. Online pressure measurement would allow this issue to be bypassed if the necessary thermal equation of state data is available for the sample. One final, technically challenging, improvement to the instrument would be to evacuate the detector drum once closed, thus removing scattering from air between the end of the 'snout' on the drum surface and the sample.

Improvements are not limited solely to the collection of data, the unique nature of the high-pressure data sets requires several 'work-arounds' for handling masking and attenuation correction in the current iteration of processing software *LaueG*. The introduction of a set of pattern-specific masks which are able to be updated and displayed on-the-fly would greatly speed up the indexing and integration process. The current attenuation correction is a standalone python script and could be easily integrated into a future *LaueG* build.

Improving facilities for high-pressure experiments at any neutron source includes the provision of ancillary facilities for sample loading (including gases), ruby fluorescence and other spectroscopic measurements, and single-crystal X-ray diffraction for sample orientation. As of January 2016 a ruby fluorescence spectrometer is operational for offline pressure measurement at ANSTO. Further expansion of the on-site supporting facilities will significantly improve the ability to successfully carry out these technically challenging neutron diffraction experiments.

As shown in Chapter 2, sample sizes on the order of 0.01 mm^3 probably represent the lower bound of feasibility on reactor sources such as OPAL, certainly at room temperature. The improved fluxes anticipated for the new generation of spallation sources such as the European Spallation Source could further reduce sample sizes, and consequentially increase pressure limits for miniature 'transmitting' pressure cells such as the mini-DAC.

6.3 References

Giriat G, Wang W, Attfield J P, Huxley A D and Kamenev K V 2010 *Review of Scientific Instruments* **81**(7).

McIntyre G, Mélési L, Guthrie M, Tulk C, Xu J and Parise J 2005 *Journal of Physics: Condensed Matter* **17**(40), S3017.

Xu J, Mao H K, Hemley R J and Hines E 2002 *Journal of Physics: Condensed Matter* **14**(44), 11543.